ISTANBUL TECHNICAL UNIVERSITY ★ GRADUATE SCHOOL OF SCIENCE ENGINEERING AND TECHNOLOGY

EXPERIMENTAL AND NUMERICAL INVESTIGATION OF MOMENTUM AND HEAT TRANSFER IN OPEN-CELL METAL FOAM SUBJECTED TO OSCILLATING FLOW

Ph.D. THESIS

Özer BAĞCI

Department of Mechanical Engineering

Mechanical Engineering Programme

JUNE 2015

ISTANBUL TECHNICAL UNIVERSITY ★ GRADUATE SCHOOL OF SCIENCE ENGINEERING AND TECHNOLOGY

EXPERIMENTAL AND NUMERICAL INVESTIGATION OF MOMENTUM AND HEAT TRANSFER IN OPEN-CELL METAL FOAM SUBJECTED TO OSCILLATING FLOW

Ph.D. THESIS

Özer BAĞCI
(503092034)

Department of Mechanical Engineering

Mechanical Engineering Programme

Thesis Advisor: Asst. Prof. Levent Ali KAVURMACIOĞLU

Thesis Co-Advisor: Prof. Nihad DUKHAN

JUNE 2015

İSTANBUL TEKNİK ÜNİVERSİTESİ ★ FEN BİLİMLERİ ENSTİTÜSÜ

SALINIMLI AKIŞ KOŞULLARINDA AÇIK HÜCRELİ METAL KÖPÜKTE AKIŞ VE ISI GEÇİŞİNİN DENEYSEL VE SAYISAL OLARAK İNCELENMESİ

DOKTORA TEZİ

Özer BAĞCI
(503092034)

Makina Mühendisliği Anabilim Dalı

Makina Mühendisliği Doktora Programı

Tez Danışmanı: Yrd. Doç. Dr. Levent Ali KAVURMACIOĞLU

Tez Eş Danışmanı: Prof. Dr. Nihad DUKHAN

HAZİRAN 2015

Özer Bağcı, a **Ph.D**. student of ITU **Graduate School of Science, Engineering and Technology**, student ID **503092034**, successfully defended the **dissertation** entitled "EXPERIMENTAL AND NUMERICAL INVESTIGATION OF MOMENTUM AND HEAT TRANSFER IN OPEN-CELL METAL FOAM SUBJECTED TO OSCILLATING FLOW", which he prepared after fulfilling the requirements specified in the associated legislations, before the jury whose signatures are below.

Advisor: **Asst. Prof. Levent Ali KAVURMACIOĞLU** ....
Istanbul Technical University

Co-advisor: **Prof. Nihad DUKHAN** ....
University of Detroit Mercy

Jury Members: **Prof. Mustafa ÖZDEMİR** ....
Istanbul Technical University

Assoc. Prof. Oğuz UZOL ....
Middle East Technical University

Prof. Hasan GÜNEŞ ....
Istanbul Technical University

Assoc. Prof. Zehra YUMURTACI ....
Yıldız Technical University

Assoc. Prof. Emre ALPMAN ....
Marmara University

Date of Submission : 11 May 2015
Date of Defense : 04 June 2015

FOREWORD

Heat transfer in metal foam is a research topic with an increasing trend as it is one of the porous media used for many relevant engineering applications. The prime aspects augmenting its popularity are its tortuous inner structure, high thermal conductivity and extremely high surface area.

This study focuses on heat transfer characteristics of isotropic metal foam subjected to steady and oscillating water flow. However, the flow experiments themselves have an important part due to the extraction of main flow parameters.

I present my gratitude to Prof. Nihad Dukhan, Asst. Prof. Levent Ali Kavurmacıoğlu and Prof. Mustafa Özdemir. They are not only my professors, but also role models for an academic life I will always pursue.

May 2015 Özer BAĞCI

(Research assistant)

TABLE OF CONTENTS

Page

ABBREVIATIONS

ANSI : American National Standards Institute
CFD : Computational fluid dynamics
CPU : Central processing unit
DC : Direct current
FFT : Fast Fourier transform
SLE : Special limit of error

LIST OF SYMBOLS

a	Constant, Equation (3.6)
b	Constant, Equation (3.6)
A	Constant, Ergun equation
A_0	Non-dimensional displacement
A_p	Piston area (m^2)
B	Constant, Ergun equation
$\tilde{a}$	Correlation coefficient, Equation (3.21)
$\tilde{b}$	Correlation coefficient, Equation (3.21)
d	Sphere diameter (mm)
D	Inner diameter of the test section (m)
d_p	Particle diameter, Ergun equation (mm)
f	Permeability-based friction factor = $\frac{(\Delta p/L)\sqrt{K}}{\rho u^2}$
f_D	Diameter-based friction factor = $\frac{2(\Delta p/L)D}{\rho u^2}$
f_{max}	Oscillating flow friction factor= $\frac{2(\Delta p_{max}/L)D}{\rho u_{max}^2}$
F	Forchheimer coefficient (dimensionless)
g	Acceleration due to gravity (m/s^2)
I	Uniformity
k	Thermal conductivity (W/mK)
K	Permeability (m^2)
L	Length of porous medium (m)
Nu	Nusselt number
Nu_L	Length- and Cycle-averaged Nusset number
Nu_z	Local cycle-averaged Nusselt number
p	Static pressure (kPa)
ppi	Pores per inch
Pé	Péclet number
Pr	Prandtl number
q''	Heat flux (W/m^2)
Re	Reynolds number based on permeability = $\frac{\rho u\sqrt{K}}{\mu}$
Re_d	Reynolds number based on particle diameter = $\frac{\rho ud}{\mu}$
Re_D	Reynolds number based on the diameter of the test section = $\frac{\rho uD}{\mu}$
Re_{max}	Reynolds number for oscillating flow = $\frac{\rho\omega D x_{max}}{2\mu}$
Re_ω	Kinetic Reynolds number = $\frac{\rho\omega D^2}{\mu}$
t	time (s)
T	Temperature (°C)
u	Average velocity (m/s)
u_{max}	Maximum flow velocity for oscillating flow (m/s)

$\tilde{\bar{U}}$	Time-averaged maximum velocity (m/s)
x_{max}	Maximum flow displacement (mm)

Greek

Δ	Change
ε	Porosity
κ	Kozeny–Carman constant
μ	Viscosity (Pa·s)
ρ	Density (kg/m^3)
ω	Frequency

Subscripts

f	Fluid
e	Effective
i	Inlet
LTE	Local thermal equilibrium
LTNE	Local thermal non-equilibrium
min	Minimum
max	Maximum
s	Solid
w	Wall
z	Flow direction, local

LIST OF TABLES

LIST OF FIGURES

EXPERIMENTAL AND NUMERICAL INVESTIGATION OF MOMENTUM AND HEAT TRANSFER IN OPEN-CELL METAL FOAM SUBJECTED TO OSCILLATING FLOW

SUMMARY

Oscillating flow and heat transfer in porous media is encountered in many engineered systems such as heat pipes, regenerators, Stirling engines, cooling units of nuclear power plants and reciprocating internal combustion engines. Due to substantial heat removal rates, there has been interest in using oscillatory flow in porous media for cooling high-power-density high-speed electronic components, as well.

Heat transfer due to oscillating flow in traditional porous media (e.g. packed spheres) has been studied before. Metal (aluminum, copper, etc.) foams are relatively new class of porous materials. They have extremely large surface area density, up to 10000 m^2/m^3, and very high porosity, around 90%. The shape of cells of metal foams can be regarded as tetrakaidecahedra. Oscillating flow and heat transfer of air in metal foam has also been studied. However, heat transfer due to oscillating flow of water in metal foam has never been studied. In terms of flow and heat transfer in porous media, air and water, as working fluids, are very different: in water, an added momentum and heat transport mechanism called dispersion is important, while it is negligible for air flow. There is also a big difference in the effective thermal conductivity when the porous medium is saturated with air compared to water. This is in addition to the difference in Prandtl number and other thermophysical properties for the two fluids. There is a difference in compressibility between the two fluids and an expected splashing for the case of oscillating water flow. These differences are expected to produce vastly different flow field and temperature distribution in metal foam.

In the current study, a 20-ppi (pores per inch) cylinder-shaped aluminum metal foam core with a porosity of 87% was tested under the conditions of steady and oscillating water flow. The core was made of 6101-T6-aluminum alloy and it was brazed into an aluminum tube with the designation code of 6061-T6. The test section was deliberately brazed in order to avoid high thermal contact resistance.

Before installing the foam as a test section, the test setup was tested hydrodynamically as a qualification study. The porous media used for this step were packed beds of 1- and 3-mm steel spheres with a cylindrical bulk volume similar to that of the metal foam. All of the porous-media flow regimes reported in literature were found. Therefore the system was proven to reveal not only turbulent flow regime in porous media, but also regimes observed at flow conditions even with the slightest fluid motion, namely pre-Darcy and Darcy regimes.

The packed bed was replaced by the metal foam and care was taken so as to prevent any leakage. For steady-state flow experiments, water inlet from an elevated tank and directly from the network were used as constant pressure sources for low and high flow rates, respectively. The system was set to be open rather than a closed loop. For

measuring pressure loss, differential pressure sensors with changeable ranges were used. For the flow rate measurements, mass scales with different ranges and accuracies along with a stopwatch were used. A quadratic relation between pressure loss and velocity was observed as expected. The pressure gradients were modified obtain linear curves with slopes varying from zone to zone. These zones with different slopes denoted different regimes. Four different regimes, namely pre-Darcy, Darcy, Forchheimer and turbulent regimes, were identified along with the transitions among them. Two important foam parameters, permeability and form drag coefficient were calculated, and proven to have different values, for each regime. Finally, the already-reduced pressure gradient-velocity couples were modified with the purpose of displaying the relationship between non-dimensional quantities, which were the friction factor and Reynolds number. This step ensured that the square root of the permeability calculated in the Darcy regime was a viable characteristic length for Reynolds number. This idea had been originated from the fact that the flow crept encapsulating the ligaments of the foam and was related well to internal morphology of the foam.

The oscillating flow experiments involved the use of a reciprocating mechanism, which also resulted in a closed system. Because the flow was transient in nature, the revolutions of the oscillation-generating mechanism were recorded with respect to time for velocity calculations. Besides, rather than a differential pressure sensor, two pressure transmitters located at both ends of the foam were used to avoid inertia-induced errors. The runs were completed with combinations multiple frequencies and flow displacements. The data was acquired using a data logger. Two frequency zones were identified. In the low frequency zone, the pressures had counteracting behaviors, whereas in the high frequency zone, those values were in parallel, still with a certain pressure difference. In both of the zones, the friction factors were higher than those of the steady-state flows, and lower than those found previously oscillating water flow experiments in packed beds of spheres.

For the steady-state heat transfer experiments, holes were drilled along the wall of the foam to measure wall temperatures. Constant heat flux was introduced through the wall. In addition, inlet and outlet water temperatures were measured. The bulk temperatures were calculated using averaged temperatures from these two ends and the wall temperature distribution. The velocities were in Darcy, Forchheimer and transition regimes. Nusselt number for each velocity case was calculated using the corresponding wall and bulk temperatures. In addition to thermal entry lengths, exit lengths were also found. The thermal entry lengths were contrasted to their counterparts in literature as well as the Nusselt numbers. The Nusselt numbers in the fully developed region for Darcy flow matched the analytical solutions extremely well for the thermal non-equilibrium approach.

The steady-state heat transfer mechanism was turned into a closed system using the same oscillation generator for the oscillating heat transfer test. The cycle-averaged wall temperature distribution was observed to be symmetric under oscillation. Therefore, only one half of the axial domain was studied. The cycle-averaged Nusselt number and temperature distribution were obtained. It was observed that the temperatures were lower for higher displacements and frequencies. The distribution was also more uniform. Nusselt number was correlated with respect to the kinetic Reynolds number.

The steady-state flow and heat transfer were modeled in three dimensions and simulated using ANSYS finite volume tools. The flow results were in good agreement with their experimental counterparts. Therefore numerical approximations were made for hydrodynamic entry length since this value is extremely hard to determine experimentally. The heat transfer results on the other hand exhibited divergence from experimental findings at high velocities. This result was attributed to the fact that the current built-in model was originally for traditional porous media, not high-porosity foam.

The oscillating flow and heat transfer were modeled in two dimensions because the propagation of the temperature required an extensive CPU time. The flow results matched the experimental values well. However, there was a significant mismatch of heat transfer results, exceeding the experimental uncertainty. This was a result of the same problem reported above and inadequate mixing due to the current turbulence model in the numerical tools.

SALINIMLI AKIŞ KOŞULLARINDA AÇIK HÜCRELİ METAL KÖPÜKTE AKIŞ VE ISI GEÇİŞİNİN DENEYSEL VE SAYISAL OLARAK İNCELENMESİ

ÖZET

Gözenekli ortamda salınımlı akış ve ısı geçişine nükleer santrallerin soğutma üniteleri, pistonlu içten yanmalı motorlar, ısı boruları, rejeneratörler, Stirling motorları gibi birçok mühendislik uygulamasında rastlanmaktadır. Yüksek ısı kayıp oranları sebebiyle, yüksek güç yoğunluklu, yüksek hızlı elektronik bileşenleri soğutmak için gözenekli ortamda salınımlı akışın kullanılmasına ilgi artmıştır.

Gözenekli ortamda salınımlı akışla ısı geçişi konusu, örneğin bilyalı yataklarla, daha önce çalışılmıştır. Metal (Alüminyum, bakır, nikel vb.) köpükler nispeten yeni nesil gözenekli ortamlardır. 10000 m^2/m^3'lere ulaşan, oldukça yüksek yüzey alan yoğunluklarına ve %90 mertebelerinde yüksek gözenekliliklere sahiptirler. Metal köpüklerin içyapılarını oluşturan, kirişlerle çevrili hücrelerin şekilleri tetradekahedrona benzetilebilir. Metal köpüklerde havanın salınımlı akışı da akademik çalışmalara daha önce konu olmuştur. Fakat suyun bu tür çalışmalarda kullanıldığı görülmemiştir.

Gözenekli ortamlarda akış ve ısı geçişi bakımından, hava ve su birbirinden oldukça farklıdır: Momentum ve enerji mekanizmalarında kaynak terimi olarak bulunan dispersiyon su için önemli, hava için ise ihmal edilebilirdir. Doymuş gözenekli ortamlarda hava ve su için etkin ısı geçiş katsayıları birbirilerinden yine oldukça farklıdır. Bunların yanı sıra, Prandtl sayıları ve diğer termofiziksel özellikleri farklılık göstermektedir. Suyun sıkıştırılabilirliği ve titreşimli akıştaki rastgele davranışı farklı incelenebilir. Bu gibi ayrılıkların akış alanı ve sıcaklık dağılımlarında da kendilerini belli etmesi beklenmektedir.

Bu çalışmada, 20 ppi (inç başına gözenek) gözenek yoğunluğuna ve %87 gözenekliliğe sahip, silindirik şekilli ticari bir alüminyum köpük, suyun düz ve salınımlı akış durumlarında incelenmiştir. Silindirin malzemesi 6101-T6 kodlu alüminyum alaşımıdır ve 6061-T6 kodlu yine bir alüminyum alaşımından üretilmiş bir borunun içine sert lehimle kaynatılmıştır. Bu birleştirme yönteminin seçilmesindeki amaç ısıl temas direncinin minimum değerde tutulması gerekliliği idi.

Metal köpüğü bir test bölmesi olarak, daha önceki çalışmalarda kullanılmış, var olan düzeneğe yerleştirmeden önce düzenek hidrodinamik olarak denendi. Bu aşama için kullanılan gözenekli ortamlar 1 ve 3 mm çapındaki çelik kürelerin oluşturduğu, boyut olarak da metal köpüğün brüt hacmiyle benzeşen bilyalı yataklardı. Literatürde rastlanan tüm gözenekli ortam rejimleri bu denemede bulundu. Ayrıca daha önceki bilyalı yataklarda elde edilen sonuçlar tekrarlanabildi. Böylece düzeneğin sürünen akıştan türbülanslı akışa uzanan geniş bir yelpazedeki kullanılabilirliği gösterilmiş oldu.

Bilyalı yataklar denemeden sonra metal köpük ile değiştirildi, fiber contalar ve teflon bantlar ile sızdırmazlık sağlandı. Sabit hızlı, tek yönlü akış deneyleri için 3.5 m yüksekliğinde bir kule yapıldı ve üzerine 50 litrelik bir su tankı yerleştirildi. Tankın üst noktasına yakın, aynı seviyede 4 noktaya 1.9 cm çapında delik delindi. Bu deliklerden su çıkışı sağlanarak sabit su yüksekliği ve dolayısıyla düşük debiler için 0.38 bar değerinde sabit bir basınç kaynağı elde edildi. Yüksek debiler için musluktan gelen su doğrudan kullanıldı. Test düzeneği açık sistem olduğu için metal köpüğü terk eden su çevreye bırakıldı. Basınç kaybı ölçümü için değiştirilen basınç aralıklarına sahip fark basınç ölçüm cihazları kullanıldı. Debi için ise fakl kapasite ve hassasiyetlerde teraziler ve bir kronometre kullanıldı. Yaklaşık 100 lineer basınç gradyeni-hız çifti ölçüldü, tabloya işlendi ve grafikte gösterildi. Gözenekli ortamların bir karakteristiği olan kuadratik eğrinin oluştuğu gözlemlendi. Basınç gradyeni hız ile bölünerek hızın yine yatay eksende olduğu grafikte gösterildi ve farklı bölgelerde farklı eğimlere sahip olduğu görüldü. Bu bölümlerin her birinin ayrı akış bölgelerinin temsil ettiği kabul edildi. Aralardaki geçiş bölgelerinin yanı sıra 4 akış rejimi tespit edildi: Darcy öncesi, Darcy, Forchheimer ve türbülanslı bölgeler. *Geçirgenlik* ve *şekil direnç katsayısı* isimli iki önemli gözenekli ortam parametresi Forchheimer denklemi vasıtasıyla her rejim için ayrı ayrı hesaplandı ve bulunan değerlerin birbirinden farklı olduğu gözlemlendi. Hıza bölerek indirgenmiş basınç gradyenleri ve Forchheimer denklemindeki diğer terimler tekrar değiştirilerek boyutsuz hale getirildi ve sürtünme katsayısı Reynolds sayısı cinsinden bir fonksiyon olarak gösterildi. Bu aşamada Reynolds sayısı ve sürtünme katsayısı için geçerli ve doğru olan karakterisik uzunluğun Darcy rejiminde bulunan geçirgenliğin karekökü olduğu gösterildi. Bu fikrin çıkış noktası, Darcy rejiminde akışkanın sürünen akış halinde ilerlemesi ve metal köpüğün iç yapısına dair bilginin ancak bu akış tarafından gösterilebileceğinin düşünülmesidir.

Salınımlı akış deneylerinde ileri ve geri periyodik hareket yapan pistonlu bir mekanizma kullanıldı. Çift yönlü çalışan piston ile sistem kapalı hale geldi. Akış, doğası gereği zamana bağlı olduğu için hız ölçümleri zamana bağlı olarak kaydedildi. Atalet etkilerine bağlı olarak ölçüm cihazı ve system arasındaki mesafeden kaynaklanabilecek hataları yok edebilmek için fark basınçölçerler kullanılmadı. Bunun yerine statik basıncı yerinde ölçebilecek basınç transmiterleri kullanıldı. Deneyler 0.116 Hz ve 0.696 Hz arasında eşit aralıklı olarak değişen frekanslar ve üç farklı akış yer değiştirme mesafesinin kombinasyonları ile tamamlandı. Basınç değerleri dijital multimetre ile zamana bağlı olarak kaydedildi, tabloya işlenip grafiklerde gösterildi. İki farklı frekans bölgesi ortaya çıkarıldı. Düşük frekans bölgesinde köpüğün iki ucundaki basınç değerleri birbirilerine zıt olarak değişti. Faka yüksek basınç bölgesinde davranışları paraleldi fakat yine de her durumda harekete sebep olacak bir basınç gradyeni mevcuttu. Salınımlı akışta elde edilen sürtünme faktörleri düz akışa kıyasla daha yüksek bulundu fakat bilyalı yataklara göre daha düşüktü.

Düz akışta ısı geçişi deneyleri için köpük duvarı üzerine eksen boyunca 33 adet 4 mm derinliğinde 1 mm çapında delikler delindi. Bu deliklere ısıl yapıştırıcılar ile sabitlenen termoeleman telleri ile duvar sıcaklığı ölçüldü. Debi için ise 20 l/d ölçüm kapasiteli manyetik debimetre kullanıldı. Duvarda sabit ısı akısı sağlamak amacıyla tüm boru yüzeyini kaplayacak bir kelepçe ısıtıcı ve birbirilerine seri bağlanmış iki adet doğru akım üreteci kullanıldı. Köpük giriş ve çıkışında suyun sıcaklığını ölçmek için iki sıcaklık probu üretildi. Bu problar sayesinde akışa dik eksende eşit aralıklı beş noktada sıcaklık ölçümü yapıldı. Suyun yığın sıcaklık dağılımı bu iki probdan alınan ortalama sıcaklıklar ve duvar sıcaklığı dağılımı yardımıyla ölçüldü. Ölçüm yapılan akış hızları Darcy, Forchheimer ve geçiş bölgelerinden seçildi. Her hız için Nusselt sayısı dağılımı duvar sıcaklıkları ve ilgili noktalardaki yığın sıcaklıkları sayesinde bulundu. Sıcaklık ve Nusselt sayısı dağılımları duvar boyunca tabloya işlendi ve grafikte gösterildi. Isıl giriş bölgelerinin yanısıra çıkış bölgeleri de tespit edildi. Isıl giriş uzunlukları ve Nusselt sayıları literatürdeki değerlerle karşılaştırıldı. Darcy rejimindeki ısı geçişlerinde tam gelişmiş bölgedeki Nusselt sayısının, ısıl dengesizlik kabulü altında, literatürdeki değerlere yakın olduğu bulundu.

Düz ve kararlı akışta ısı geçişi için hazırlanmış açık düzenek aynı salınım üretecinin bağlanması ile yine kapalı hale getirildi. Benzer frekans ve yer değiştirme değerleri kullanıldı. Çevrim ortalaması alınmış duvar sıcaklığı değerlerinin eksen boyunca simetrik dağılıma sahip olduğu ortaya çıkarıldı. Böylece metal köpük duvarının yalnızca bir yarısının incelenmesinin yeterli olduğuna karar verildi. Nusselt sayısının hesabında, literatürde de karşılaşıldığı gibi giriş sıcaklıkları ve duvar sıcaklıkları kullanıldı. Çevrim ortalaması alınmış duvar sıcaklığı ve Nusselt sayısı dağılımı tablolara işlendi ve grafiklerde gösterildi. Her frekans-yer değiştirme çifti için azami sıcaklık tespit edildi ve yüksek frekans ve değiştirme değerlerinde bu değerin daha düşük olduğu tespit edildi. Ayrıca bu yüksek değerlerde sıcaklıkların duvar boyunca daha düzgün dağılımlı olduğu görüldü. Nusselt sayılarının her konfigürasyon için duvar boyunca da ortalamaları alınarak kinetik Reynolds sayısı cinsinden, yine literatürde olduğu gibi üstel fonksiyon olarak ifade edilebildiği gösterildi.

Metal köpük içinde suyun düz akışı ve ısı geçişi, gerçek hacmin dörtte birinin 3 boyutlu olarak modellendi ve ANSYS Fluent isimli ticari akış analizi koduyla çözümlendi. Hidrodinamik analiz sonuçları deney sonuçları ile uyuşuyordu. Bu sebeple, deneysel olarak bulunması oldukça güç olan hidrodinamik giriş uzunluğunun kestirimi yapıldı. Diğer taraftan ısı geçişi sonuçları düşük hızlarda deneysel sonuçlarla benzeşirken yüksek hızlarda deneysel sonuçlardan ıraksamaya başladı. Bu sonucun sebebi Fluent içindeki gözenekli ortam modelinin geleneksel gözenekli ortamlar düşünülerek hazırlanmış olması olarak kabul edilebilir.

Salınımlı akış ve ısı geçişi 2 boyutlu olarak modellendi. Bunun sebebi, zamana bağlılık sebebiyle akış alanı hesabı yakınsasa bile sıcaklığın yayılması ve sanki-dengeli hale gelmesi için yüksek işlemci zamanlarının gerekmesiydi. Hidrodinamik sonuçlar deneyle yine benzerlik gösterse de ısı geçişi sonuçlarında deneydeki belirsizlik değerlerini de aşan belirgin farklar vardı. Bu sonuç yukarıdaki sebeple birlikte, salınımdan ötürü oluşması gereken karışmanın mevcut türbülans modelinin yetersizliği sebebiyle bulunamamasına bağlandı.

1. INTRODUCTION

1.1 Flow in Metal Foam

Man-made porous media, e.g., packed spheres and metal, graphite, ceramic and polymeric foams are highly exploited in many engineering applications. Open-cell metal foam can be manufactured from several metals and alloys, e.g., aluminum, copper, steel and nickel [1]. These highly-permeable foams have relatively high thermal conductivity and contain high surface area per unit volume; their internal structure (web-like) grants forceful mixing of through fluid flow. For liquid flow in metal foam, dispersion – an added mechanism of transport – is considerable. All these attributes make metal foams attractive for heat transfer enhancement, e.g., in electronics cooling [2], and in gas–liquid and liquid–liquid compact heat exchangers [3]. Boomsma et al. [4] have experimentally proven that, at the same pumping power, certain compressed aluminum foam heat exchangers generated thermal resistances that were two to three times lower than commercially available heat exchangers. Mahjoob and Vafai [5] published a synthesis of fluid and thermal transport models for metal-foam heat exchangers, and introduced a performance factor for assessing the enhanced heat transfer and pressure drop penalty simultaneously, which showed superior performance of such heat exchangers.

In applications requiring flow of liquid or gas in metal foam, e.g., heat exchangers and filters, Understanding various flow regimes in metal foam, and the associated pressure drop, are critical. For example, flow details directly influence convection heat transfer, chemical reaction rates and filtration effectiveness, as well as the required pumping power.

The internal structure of metal foam drastically influences the flow field by destroying boundary layers and compelling the fluid to travel through winding tortuous paths. In order to understand the pressure drop penalty, one must first understand the characteristics of flow regimes in metal foam and the processes of energy dissipation in each regime, as well as the transition from one regime to another.

Fluid flow in (traditional) porous media has been the subject of numerous studies, e.g., [6-12]; and has been covered in several books, e.g., [13]. Open-cell metal foam is different from traditional porous media in two regards: (1) it has a very high porosity (often greater than 90%), and (2) it has a web-like internal structure with the solid ligaments being relatively thin compared to cell size. These two attributes endows the foam with high permeability—in the order of 10^{-8} m^2 compared to 10^{-10} m^2 for packed spheres. Hence, one must be careful not to simply expect well-accepted empirical results for flow in traditional porous media to be valid for flow in metal foam. For example, values of Reynolds number corresponding to transition among flow regimes in traditional porous media may or may not be easily extrapolated to metal foam.

Compared to traditional porous media, the literature on fluid flow in metal foam is significantly less sizable [14]. The study of Beavers and Sparrow [15] is one of the earliest, if not the earliest, dedicated in part to investigating pressure drop of water in three nickel foams. No mention of the porosity or pore density (number of pores per inch) was provided. Beavers and Sparrow [15] employed Reynolds number and friction factors based on permeability to plot their data, and identified a departure from Darcy regime at Reynolds number of order unity. Montillet et al. [16] used permeametry to determine the specific surface area and tortuosity of three nickel foams having 45, 60 and 100 pores per inch (ppi). There was a noticeable change in flow regimes at Reynolds number, based on an equivalent pore diameter, between 5 and 10. Edouard et al. [17] reviewed the literature on pressure drop in metal foam. They reported severe divergence of available correlations in terms of predicting pressure drop, permeability and form/inertia coefficient.

Mancin et al. [18] investigated air pressure drop in six samples of aluminum foam for the purpose of obtaining a widely-applicable correlation. From inspection of their pressure drop data, it is apparent that all the data lied in post-Darcy regime, and did not exhibit transition. Naturally, the issue of flow regimes and transition was not addressed by Mancin et al. [18].

Much of the previously published data on flow in metal foam, e.g., [2,19-23], contain significant disagreements on the values of the two pressure drop parameters, i.e., the permeability and the form drag coefficient, for foams with similar porosities and internal structures. These discrepancies are attributed to three possible causes: (1) foam sample size in flow direction used by various researchers [24], (2) foam sample size perpendicular to flow direction, [25,26], and (3) overlooking flow regimes encountered in a given experimental data set, along with the fact that the same foam exhibited different values of permeability and form drag coefficient in different flow regimes, as was shown by Boomsma and Poulikakos [22]using water flow and by Dukhan and Minjeur [27] using air flow in aluminum foam.

The literature containing flow regime changes in metal foam is limited. It also seems that flow-regime transitions were encountered happenstance. A transition from Darcy to Forchheimer regime was identified by Boomsma and Poulikakos [22] at an average water velocity around 0.10, 0.11 and 0.07 m/s (Reynolds number based on Darcy-regime permeability, Re 14.2, 22.3 and 26.5) for 10-, 20- and 40-ppi aluminum foam, respectively. In an experimental study targeting compressibility and inertia effects, Zhong et al. [25] reported departure from Darcy regime at Re of about 0.1 for air flow in sintered steel foam. For various metal foams, Bonnet et al. [28] and Liu et al. [29] identified a transition from Darcy to Forchheimer regime.

Dedicated studies purposely geared toward establishing various flow regimes in metal foam, and transition among them, are almost non-existent. Dukhan and Ali [30] presented results of an experimental study of flow through aluminum foam samples. A distinction was made between transition from Darcy to Forchheimer regimes and from laminar to turbulent flow regimes. The data in [31] was not extensive and the working fluid was air.

The current work presents new set of experimental data for water flow in metal foam to establish various flow regimes, and to assess the behavior of pressure drop in each regime. Such information has not been available in the literature, to the best knowledge of the authors. Understanding flow regimes and their boundaries can directly aid in modeling –numerical and analytical – of flow in metal foam; and it can assist in interpreting and cognizing heat and mass transport in such media.

1.2 Heat Transfer in Metal Foam

Open-cell metal foams are excellent heat exchange cores [4]. They have high conductivities and very large surface area density. The internal structure of the foam causes vigorous mixing and dispersion, which augment convection.

Solutions and simulations, e.g., [32-34], of heat transfer inside metal foam, along with various assumptions, require experimental validation. Experimental data also has intrinsic value and can provide empirical correlations for practical design. In 2012 a review by Zhao [35] indicated that there has been a lack of reliable experimental heat transfer data for open-cell metal foam in general. In 2006, no experimental data was available for metal-foam-filled pipes, Lu et al. [34].

Boomsma et al. [4] have shown that compressed open-cell aluminum foam heat exchangers generated thermal resistances that were two to three times lower than the best commercially available heat exchanger, at the same pumping power.

Due to the complexity of heat transfer phenomenon inside metal foam, researchers have solved simplified forms of the governing equations, and relied on numerical simulations. Calmidi and Mahajan [32] numerically studied forced convection of air flow in aluminum foam. Hwang et al. [23] indicated that the local Nusselt number for air flow in metal foam increased with increasing Reynolds number. Angirasa [33] numerically studied convection heat transfer due to water flow in metal foam heat dissipaters. He invoked local thermal equilibrium. The validity of the local thermal equilibrium assumption is questionable due to the difference in the thermal conductivities of the solid and fluid phases.

Lu et al. [34] analyzed forced convection in a tube filled with metal foam subjected to constant wall heat flux. The two-equation model, which relaxes the thermal equilibrium assumption, was solved. They employed the Brinkman-extended Darcy momentum model. A closed-form solution for the solid and the fluid temperatures was presented. They exploited the solution for investigating the effect of various foam parameters in practical heat-exchange designs. Analytical solutions in porous media continue to be sought [36-38] due to their utility, identifying trends of critical variables, parametric studies and for validating numerical models.

Some recent experimental studies were geared toward practical applications, e.g., testing metal-foam designs for cooling future generation fuel cells. Odabaee et al. [39] experimentally showed that air-cooled fuel-cell systems employing metal foam required half the pumping power of current water-cooled systems, while removing the same amount of heat at identical operating conditions. In a related study Fiedler et al. [40] experimentally established the relationship between the thermal and electrical contact resistances and the compressive stress applied between metal foam and graphite plates. This study was a step toward reducing cost for future generation air-cooled fuel cells [41].

Metal foam has also been used to extend external surfaces in order to enhance heat transfer from such surfaces. Recently, Khashehchi et al. [42] investigated the wake region behind a foam-covered cylinder subjected to cross air flow. Chumpia and Hooman [43] evaluated the performance of single tubular aluminum-foam heat exchangers in which foam layers were attached to the outer surface of tubes subjected to cross flow of air. The foam-covered tubes performed substantially better than finned tubes under the same test conditions. A summary of some experimental studies for heat transfer in metal foam due to strictly internal flow of air and water is given in Table 1.1. It should be noted that the last number is the length of the foam test sample in flow direction for each study.

From Table 1.1, three facts emerge: (a) experimental studies concerning heat transfer in metal foam in general employed small foam sample sizes (or at least small dimension in one direction) or a short length in the flow direction relative to flow area hydraulic diameter, which makes their results specific to the samples tested, as the data may contain unassessed size and/or entry and exit effects (b) studies with water as the cooling fluid are few indeed; water flow provides much higher heat transfer rates due to its higher thermal conductivity (compared to air) and also due to dispersion which is negligible for air flow in metal foam, and (c) only one experimental study involved the cylindrical geometry, such geometry is most suited for many practical heat exchange designs and reactors.

While literature on porous media flow and heat transfer is abundant, the issue of thermal development in porous media is addressed, or displayed, in only several articles [44-59]. These articles employed various geometries, boundary conditions and simplifying assumptions. Haji-Sheikh et al. [54] investigated the thermal entrance length for flow through rectangular porous passages with different aspect ratios, and subjected to constant wall temperature and constant wall heat flux. Hydrodynamic development was ignored and local thermal equilibrium was imposed on their analysis. For narrow passages with constant wall heat flux, they indicated that thermal fully developed conditions may not be attainable in practical applications. Hooman et al. [55] analytically investigated thermal development in the same geometry but subjected to isothermal walls and including viscous dissipation. Similar to [54], hydrodynamic development was ignored and local thermal equilibrium was imposed.

Table 1.1 : Experimental Studies on Heat Transfer in Metal Foam from the Literature.

Working Fluid	Study	Geometry	Dimensions (mm)
Air	Calmidi and Mahajan [32]	Block	45 × 63 × 196
	Hwang et al. [23]	Block	60 × 25.4 × 60
	Bhattacharya et al. [20]	Block	43.75 × 62.5 × 192.5
	Bhattacharya and Mahajan [60]	Block (fin)	3.12 × 56.25 × 62.50 6.25 × 56.25 × 62.50
	Zhao et al. [61]	Block	12 × 127 × 127
	Kurtbas and Celik [62]	Block	8 × 52 × 62 13 × 52 × 62
	Mancin et al. [63,64]	Block	100 × 20 × 100
	Dukhan et al. [65]	Cylinder	255.6 × 152.4
Water	Boomsma et al. [4]	Block	40 × 40 × 2
	Hetsroni et al. [66]	Block	2 × 10 × 54
	Kim et al. [19]	Block (fin)	9 × 90 × 30

Hooman and Ejlali [56] and Hooman and Haji-Sheikh [57] investigated thermal development and entropy generation due to forced convection in a porous tube with uniform wall temperature and a rectangular porous duct with isoflux walls, respectively. In both cases, the effect of viscous dissipation was included, while the assumption of local thermal equilibrium and hydrodynamically fully-developed flow were imposed. Nusselt number depended on Darcy-Brinkman number and clearly showed thermal development behavior. In the latter study, it was observed that viscous dissipation reduced Nusselt number in both thermally developing and fully-developed regions.

Hooman and Gurgenci [58] investigated the effect of viscous dissipation on forced convection in parallel-plate channel filled with a porous medium. The plates were subjected to constant temperature and constant wall heat flux- one boundary condition at a time. The local thermal equilibrium model was solved numerically. Nusselt number behavior showed dependence on Brinkman number in the thermally-developing region for isothermal walls and isoflux walls cases. Hydrodynamic development was presented in terms of velocity profiles.

In a different study [59] Hooman and Gurgenci numerically studied the effect of temperature-dependent viscosity on forced convection due to liquid flow through a porous medium sandwiched between two isoflux parallel plates. Here too the assumption of local thermal equilibrium was imposed. Velocity and temperature profile shapes as well as hydrodynamic and thermal development was seen to be affected by changes in viscosity.

Noh et al. [44] experimentally investigated flow and thermal aspects for water transport through an annulus filled with aluminum foam and heated externally with a constant heat flux. The wall temperature and the local Nusselt number were given as functions of axial location, at only four axial locations. Thermal development was obvious, but concrete conclusions were difficult to ascertain due to the limited number of data points.

Nield et al. [46] analytically investigated thermal entry length for the case of a circular-tube porous media subjected to constant heat flux assuming local thermal equilibrium between the solid and fluid phases in the porous medium. They ignored hydrodynamic development in the analysis. Nonetheless, this is the closest case to the problem investigated in the current paper. A comparison of the results of the current study to those presented in [46] will be given below.

The thermal entry length, as well as the effect of thermal development, is often ignored in metal foam heat transfer studies. In the current study, direct measurements of wall, inlet and outlet temperatures for water flow inside heated, commercial open-cell aluminum foam are presented. The foam cylinder tested is sufficiently long to ensure that the complete thermal development phenomenon is clearly captured. Flow velocities covers Darcy and non-Darcy flow regimes. The thermal entry length is obtained and contrasted to the most relevant theoretical predictions. The experimentally obtained data have intrinsic value, and to the knowledge of the authors, the data set is novel. The information gained is critical for validation of analytical and numerical models of heat transfer in metal foam, as well as for heat-exchange engineering designs employing metal foam.

Direct comparisons to experimental values of key variables is lacking in many analytical porous media studies concerning heat transfer [36-38], and seem to be non-existent in the literature concerning heat transfer in metal foam. Experimental verifications, when possible, add confidence to analytical solution and validate numerical modeling and simulations. Experimental data also has intrinsic value and they can provide correlations for practical engineering design. In 2006, Lu et al. [34]

stated that no experimental data was available for metal-foam-filled pipes. The circular geometry is preferred in many heat exchange applications. In a 2012 comprehensive review, Zhao [35] indicated that there has been a lack of reliable experimental heat transfer data for open-cell metal foam in general. A summary of available experimental data for heat transfer in metal foam will be summarized next.

1.2.1 Studies with air

Calmidi and Mahajan [32], measured the wall temperature of aluminum foam sample bounded by substrates. For comparing to their numerical results, they used the measured wall temperature to obtain the average surface heat transfer coefficient. Hwang et al. [23] obtained wall and exit temperature measurements for air flow through metal foam having dimensions $60 \times 25.4 \times 60$ mm^3. The data was used to investigate heat transfer in terms of Nusselt number. Bhattacharya et al. [60] used the same kind of temperature measurements to obtain the effective conductivity of metal foam, while Bhattacharya and Mahajan [60] used similar techniques to assess the thermal performance of a finned-metal-foam heat sink. Zhao et al. [61] tested convection due to air flow in several foam samples $127 \times 127 \times 12$ mm^3 each. Kurtbaş and Çelik [62] published the results of an experimental study of forced and mixed convection heat transfer in a foam-filled rectangular channel for air as the working fluid. Similar measurements were conducted. Mancin et al. [67] presented experimental data for forced convection due to airflow in several samples of aluminum and copper foam. Overall and interstitial heat transfer coefficients were obtained; foam finned surface efficiency was investigated. Each foam sample was 100 mm long and had a cross section of 20 mm × 20 mm. Dukhan et al. [65] measured actual air temperature inside a cylinder of metal foam heated with constant heat flux and cooled by air. The tube had a length of 152.4 mm in the flow direction and an inside diameter of 255.6 mm. Wall temperature measurements were limited, and the Nusselt number was not discussed.

1.2.2 Studies with water

Experimental studies concerning heat transfer in heated metal foam with water as the cooling fluid are few indeed. Water flow provide much higher heat transfer rates due to its higher thermal conductivity (relative to that of air) and also due to dispersion which is negligible for air flow in porous media.

Boomsma et al. [4] experimentally investigated compressed aluminum foam performance as a compact heat exchanger using water as a coolant. The foam size was 40 mm × 40 mm × 2 mm. Hetsroni et al. [66] investigated the cooling of 40-ppi metal-foam heat sink for transmission window. The foam dimensions were 10 mm × 45 mm × 2 mm. Kim et al. [19] studies convection in a sample of metal foam 9 × 90 × 30 mm^3. One common fact about these studies is that they employed small foam sample sizes (small length at least in one direction), which makes the results specific to the samples tested.

In the current study, direct measurements of wall and inlet and outlet temperatures for water flow inside heated commercial aluminum foam are presented. The length of the foam cylinder tested is long to ensure full thermal development and minimize size effects. Flow velocities encountered Darcy and non-Darcy regimes. Such measurements have an intrinsic value. To the knowledge of the present authors, the experimental data are novel, and can be used for validation of analytical and numerical models of heat transfer in metal foam and for assessing the performance of heat-exchange engineering designs based on such media.

1.3 Oscillating Flow in Metal Foam

Time-dependent periodic flows include oscillating (or reciprocating) and unidirectional pulsating flow. It is well established that heat transfer can be enhanced by employing time-dependent flows compared to heat transfer due steady-state flow. Lambert et al. [68] proposed oscillating flow for enhancing heat-transfer performance of solar devices. For oscillating flow, the effective thermal diffusivity was several orders of magnitudes higher than the fluid molecular diffusivity [69].

Oscillating flow adds another layer of complexity to the already complex problems of flow and heat transfer in porous media. For interpreting and understanding of heat transfer driven by oscillating flow, one must first understand the characteristics of oscillating flow, in terms of increased pressure drop (or pumping power), effect of frequency, effect of stroke length, flow regimes, scales and pertinent non-dimensional numbers, etc.

Oscillating and pulsating fluid flow and heat transfer in traditional porous media (spherical particles, granular beds and mesh screens) have received considerable attention. Kim et al. [70] and Guo et al. [71] conducted numerical analysis for pulsating flow and heat transfer in porous media. Both studies were for a porosity of 60%, and a Prandtl number equal to 0.7, which correspond to air. Khodadadi [72] provided an analytical solution for oscillatory flow through a porous channel bounded by two solid walls for two limiting cases: highly inertial and highly viscous flow. For the first case, the velocity and pressure gradient had a phase shift of 90° and there was a channeling effect: the velocity profiles exhibited maxima next to the solid wall. Zhao and Cheng [73] experimentally investigated pressure drops due to oscillatory air flow through a woven-screen packed column. The data were correlated using the friction factor based on maximum flow velocity and the kinetic Reynolds number. The average pressure drop for the oscillatory flow was several times higher than that for steady flow. Hsu et al. [74] experimentally investigated oscillating flow through packed wire screens.

Cha et al. [75] investigated oscillating flow of helium through typical porous fillers for pulse-tube and Stirling-cycle cryocooler regenerators (e.g. mesh screens, foam metal, stacked micro-porous nickel disks), both experimentally and using CFD. They reported a phase shift between the inlet and outlet pressures of the porous media that increased with increasing frequency.

Pamuk and Özdemir [76] experimentally investigated oscillating water flow in two sets of mono-sized packed steel balls. The porosity of the first set was 36.9%, while it was 39.1% for the other. It was shown that the permeability and inertial coefficient for oscillating flow were greater than their steady-state counterparts. The friction factor was correlated with the Reynolds number. Pamuk and Özdemir [77] presented experimental heat transfer results using the same porous media subjected to oscillating flow of water.

For oscillating flow in metal foam, there are only few published studies. Leong and Jin [78] experimentally investigated oscillating air flow through a channel filled with open-cell metal foam. They showed that the oscillating flow characteristics in the foam were governed by the hydraulic-ligament-diameter-based kinetic Reynolds number and the dimensionless flow displacement amplitude. The effect of the kinetic Reynolds number on the pressure drop and flow velocity was more significant. There was a small phase difference between the velocity and the pressure drop. The maximum friction factor increased with decreasing displacement amplitude. A correlation for the maximum friction factor was presented. As compared to oscillating flow in wire screens, the maxi-mum friction factor was generally lower for the case of metal foam.

In a different study, Leong and Jin [79] studied heat transfer due to oscillating air flow through a channel filled with 40 pore-per-inch aluminum foam experimentally. The velocity and pressure drop were also measured. The pressure drop and flow velocity increased with increasing oscillating frequency and varied almost sinusoidally.

As indicated by Pamuk and Özdemir [76] and by the review given above, all experimental studies in the literature concerning oscillating flow and heat transfer in porous media (including metal foam) used gas, mostly air, as the working fluid. Oscillating flow of a liquid, e.g., water, in metal foam has not been presented.

The purpose of the current experimental study is to map out the characteristics of oscillating water flow in open-cell metal foam using pertinent parameters affecting this phenomenon. The results of the current study will be contrasted to those in previous studies employing air flow in similar metal foam; and also to the results obtained for different porous media (packed beds of spheres and screens). The ultimate purpose is to enhance fundamental understanding of oscillating flow phenomenon in metal foam as prerequisite for understanding other related phenomena, e.g., heat transfer.

1.4 Oscillating Heat Transfer in Metal Foam

Open-cell metal foams have high thermal conductivity and surface area density besides high porosity and permeability. The web-like internal structure of metal foams promotes heat transfer through mixing of flowing fluids. As such, metal foams are attractive for heat transfer enhancement systems.

It is well-established that heat transfer can be enhanced substantially by employing time-dependent flow as compared to heat transfer due steady-state flow. Oscillating (or reciprocating) flow is time-dependent periodic flow. Lambert et al. [68] proposed enhancing heat-transfer performance of solar devices by employing oscillating flow. He showed that for oscillating flow, the effective thermal diffusivity was several orders of magnitudes higher than the fluid molecular diffusivity. Pamuk and Özdemir [77] indicated that heat transfer due to oscillating flow is comparable to that of heat pipes.

Oscillating flow and heat transfer in porous media occur in many applications, e.g., heat pipes, regenerators (e.g. in Stirling engines and cryocoolers), cooling designs of nuclear power plants and reciprocating internal combustion engines. Oscillating heat transfer in porous media can produce two advantageous effects: 1) a high heat transfer rate and 2) a more uniform temperature distribution on a (hot) substrate surface due to the presence of two thermal entry regions. As such, the heat-transfer design can be used to cool modern high-speed devices (e.g., microprocessors and transistors), the reliability and operation speed of which depend on not only their average temperature, but also on temperature uniformity.

Transport phenomena due to oscillating flow are naturally complex; and they are not very well understood [80]. Heat transfer due to oscillating flow in traditional porous media (packed spheres, granular beds and mesh screens) have received considerable attention. Sozen and Vafai [81] investigated forced convection due to oscillating compressible ideal gas (Refrigerant-12m) flow in a packed bed numerically. The porosity of the bed was 39%. Byun et al. [82] analyzed heat transfer due to oscillating flow through infinitely large porous slab using the two-equation model (thermal non-equilibrium). Habibi et al. [83] solved the heat transfer equations for a two-dimensional channel partially filled with a porous medium subjected to reciprocating air flow. The channel was discretely heated on one side to simulate compact circuit boards.

Pamuk and Özdemir [77] presented experimental heat transfer results for oscillating water flow in two sets of mono-sized packed steel balls (1 and 3 mm). The porosity of the first set was 36.9%, while it was 39.1% for the other. The effect of various parameters on heat transfer were studied, e.g., frequency, flow displacement and heat input. Results were presented in terms of cycle-averaged local Nusselt number and space-cycle-averaged Nusselt number; the latter correlated well with the kinetic Reynolds number and non-dimensional flow displacement.

Recently, Dai and Yang [84] numerically studied oscillating gas flow and heat transfer in regenerative cryocoolers using the Lattice Boltzmann Method. They noted that the velocity and temperature profiles were mainly influenced by the Womersley number. Little vortices were observed near the surface of the solid phase.

Pathak et al. [80] numerically studied oscillating flow and heat transfer in a 75%-porous medium composed of square cylinders. The working fluid was helium. The Nusselt number strongly depended on flow oscillation frequency and amplitude. Significant phase lag occurred among velocity, pressure, temperature and heat transfer processes.

For heat transfer due to oscillating flow in metal foam, there are only few published studies. Leong and Jin [79] experimentally studied heat transfer due to oscillating air flow through a channel filled with aluminum foam and subjected to constant wall heat flux. The 90%-porous foam was produced by sintering and had 40 pore-per-inch (ppi). The cycle-averaged Nusselt number increased with both the kinetic Reynolds number and dimensionless amplitude of flow displacement. A correlation for the length-averaged Nusselt number as a function of these two non-dimensional parameters were provided.

In a different investigation, Leong and Jin [85] conducted experiments to study the effect of frequency on heat transfer performance of metal foam heat sinks subjected to oscillating flow of air. The aluminum foam used in the heat sinks had 10, 20 and 40 ppi. The cycle-averaged temperature decreased with increasing kinetic Reynolds number while the Nusselt number exhibited the opposite trend. Better heat transfer was noted for foam with low pore density.

In a third experiment, Leong and Jin [86] studied heat transfer of oscillating air flow in two porous channels having commercial aluminum (20 ppi) and copper (60 ppi) foams with porosities around 90%. The oscillating flow amplitude was larger than the length of the test section, in order to ensure proper cooling. The local wall temperature was maximum at the center of the test section, and the cycle-averaged wall temperature decreased with increasing Reynolds number. The cycle-averaged Nusselt number had a concave shape with a minimum at the center of the channel. Heat transfer was higher for the case of copper foam due to its higher conductivity, as expected.

Fu et al. [87] carried out experiments on heat transfer of oscillating air flow in channels filled with commercial aluminum (40 ppi) and carbon (45 ppi) foams- each having a porosity around 90%. The uniformity of the surface temperature in oscillating heat transfer was displayed.

As indicated by Pamuk and Özdemir [76] and by the literature review given above, all experimental studies in the literature concerning oscillating flow and heat transfer in porous media (including metal foam) used gas, mostly air, as the working fluid. Oscillating flow of liquid, e.g., water, in metal foam has only been presented recently [88]; no heat transfer findings were given. One main difference between gas and liquid flows in porous media is that dispersion is significant in the latter, while so weak that it has been ignored in the former [32]. Another difference is the length of the entrance region, which depends strongly on the Prandtl number of the working fluid. Both of these matters affect oscillating heat transfer significantly.

The purpose of the current experimental study is to map out the heat transfer characteristics due to oscillating water flow in open-cell metal foam in terms of pertinent parameters. The results of the oscillatory heat transfer study will be compared to other studies with air as the working fluid in similar metal foam; and also to the results corresponding to those for some different classes of porous media (e.g., packed beds of spheres and screens). A comparison of oscillating water flow heat transfer and steady state heat transfer in the same metal foam of the current study will also be provided. The purpose is to enhance fundamental understanding of heat transfer in oscillating liquid flow in metal foam in order to guide engineering design tools (analytical and numerical) for potential applications, e.g., cooling systems for high-power devices and regenerators based on metal foam.

1.5 Computational Study on Transport in Metal Foam

Insight about flow inside metal foam is vital for many engineering applications, regardless of the type of the fluid. However, there are still aspects of fluid flow in metal foam which needs to be studied such as entrance and exit lengths of water flow in metal foam.

Those phenomena were studied experimentally by Dybbs and Edwards for water in Plexiglas bundles [7]. They observed visually that the entry length was approximately 3 unit cells. To the knowledge of the authors, further studies on entry length were merely on air through porous media or even disregarded due to negligible value [89].

Vafai and Tien proposed the hydrodynamic length to be equal to Ku/ν [51], whereas it was stated to be K/ε in [48], where ε is the porosity.

A part of the study was dedicated to computation of the hydrodynamic entry length of water flow through a 325-mm-long 20-ppi metal foam with a diameter of 50.8 mm employing a macro-scale model.

2. PROBLEM FORMULATION AND NUMERICAL MODELS

2.1 Continuity and Momentum Equations

Because there is only one phase involved in transport in metal foam, the continuity equation can be written as

$$\varepsilon \frac{\partial \rho}{\partial t} + \nabla\left(\rho \vec{v}\right) = 0 \qquad \textbf{(2.1)}$$

where ε is the porosity, ρ is the density of water which was always around 997.88 kg/m^3, depending on the operating temperature, and v was the volume-averaged velocity vector, since a solid part was also included in a representative volume of the foam.

The governing momentum equation for porous media has two source terms for pressure loss in addition to those in resemblance with the terms of momentum equation for flow in a homogeneous medium.

$$\rho\left[\frac{1}{\varepsilon}\frac{\partial \vec{v}}{\partial t} + \frac{1}{\varepsilon^2}\left(\vec{v}\nabla\vec{v}\right)\right] = -\nabla p + \mu_e \nabla^2 \vec{v} - \frac{\mu}{K}\vec{v} - \frac{\rho F}{\sqrt{K}}\left|\vec{v}\right|\vec{v} \qquad \textbf{(2.2)}$$

In Equation (2.2), p is the static pressure, μ_e is the effective viscosity, which is actually influenced by the fluid and solid part of the medium, K is the permeability and F is the form drag coefficient. The source terms mentioned above are inherent due to the influence of the solid part on the flow. The third term on the right hand side corresponds to the pressure loss due to viscosity while the fourth term represents inertial-drag-related loss.

The commercial software ANSYS Fluent has a built-in porous media model and it solves the equation of motion with the source terms,

$$S_i = -\left(\sum_{j=1}^{3} D_{ij} \mu v_j + \sum_{j=1}^{3} C_{ij} \frac{1}{2} \rho |\vec{v}| v_j \right) \tag{2.3}$$

where the minus sign signifies pressure loss, D_{ij} and C_{ij} are the coefficients equal to $1/K$ and $2F/\sqrt{K}$, respectively. Those two coefficients depend on the current regime, as will be discussed later.

2.2 Steady Flow Model and Approximation of the Hydrodynamic Entry Length

The axial length of the entire computational domain was chosen as a part of the of test setup explained in detail in [90]. Water entered a 110-cm-long stainless steel pipe 32 mm in diameter followed by a divergence to 50.8 mm and a polyethylene tube with this diameter. The metal foam was located next, before another polyethylene tube attached to another stainless steel pipe with the same dimensions as the preceding counterparts, only positioned symmetrically with respect to the test section. The computational domain, however, did not contain the steel pipes completely because the flow was observed to be already developed before the diameter change from 32 mm to 50.8 mm.

Both the geometry and the mesh were generated using ICEM CFD. Only one quarter of the cylindrical domain was modeled to avoid excessive computational time. Therefore symmetry boundary condition was attributed to the orthogonal surfaces of the domain.

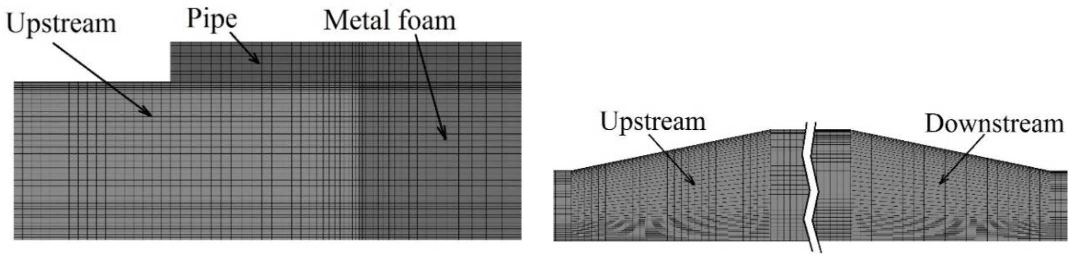

(a) (b)

Figure 2.1 : The zones of the computational domain: (a) Inlet of the test section, (b) Converging and diverging parts of the flow domain.

The computational mesh was constructed by block-structuring the geometry. A high-quality mesh was obtained and cells close to the wall boundaries were made fine in order to capture accuracy of flow variables in the boundary layer. The computational domain consisted of 4 zones as seen in Figure 2.1. The upstream and downstream zones next to the porous zone, in the middle, were assigned to be fluid zones only. The cylindrical shell encapsulating the foam was the only solid zone.

For all of the steady-state runs, flow in the porous zone was considered laminar because every velocity was in either Darcy or Forchheimer regime. However for cases with higher velocities, because of the narrow ends of the computational domain, the flow could not be considered laminar anymore. ANSYS Fluent was used to do the computational flow analysis. SIMPLE was chosen as the pressure-velocity coupling method. The absolute convergence criterion was chosen as 10^{-6} for all of the dependent values for flow equations. The flow model in the foam was chosen to be laminar for all the cases. This model changed from laminar to turbulent only for the upstream and downstream zones, and k-ε turbulence model was switched on therein. In addition, enhanced wall treatment was enabled to obtain accurate results in near-wall regions.

Velocity inlet boundary condition was attributed to the domain inlet. For the laminar cases, parabolic velocity distribution, corresponding to the required flow rate, was introduced. The inlet velocities were uniform for the turbulent cases. The pressure outlet was identified by entering zero as the gauge pressure.

The porous media model of Fluent involves the solution of momentum transport equation with source terms. Those source terms are responsible for added loss of pressure due to viscous and inertial drag in the porous medium, as it is the case also for the Forchheimer equation.

The foam parameters required for were determined experimentally and found to be different for each flow regime [90]. The form drag coefficient of flow in Darcy regime is zero because the inertial effects are negligible. The source term coefficients for viscous and inertial resistances were determined using the permeability and the drag coefficient pertaining to the corresponding regime. Same coefficients were entered for all three orthogonal principal axes on account of the fact that the porous medium was isotropic [91].

In order to see whether the CFD results were independent from the mesh resolution, three computational grids with different cell numbers were prepared. The three-dimensional laminar model explained above was run using the three meshes for the highest superficial velocity in Darcy region, which was 0.0067 m/s. The criterion for comparison of the results was the skin friction coefficient (C_f) found by averaging on the part of the pipe in contact with the foam. The differences between the results for the three meshes were in the tolerance range. Therefore the model was accepted to be mesh independent. The cell numbers of the meshes and the skin friction coefficients can be found in Table 2.1.

Table 2.1 : Number of cells and averaged skin friction coefficient for each mesh.

	Number of cells	C_f
Fine	1528080	907.6
Medium	537264	905.2
Coarse	332442	902.1

All of the cases including flow rates in Darcy and Non-Darcy (Transition and Forchheimer) are tabulated in Table 2.2.

Table 2.2 : Velocity- and regime-related details.

Regime in the foam	Superficial Velocity (m/s)	Flow regime in the pipe
Darcy (Creeping, laminar flow)	0.0049 0.0058 0.0067	Laminar
Transition from Darcy to Forchheimer	0.0072 0.0074 0.0099 0.0196	Laminar
Forchheimer (Weakly inertial, laminar flow)	0.0251 0.0307 0.0411 0.0596	Turbulent

The computations were completed employing 32 processors for each case. Each run took around 1 hour.

In Darcy and Forchheimer regimes, the static pressure difference between the upstream and downstream sides of the foam showed a good agreement with those found experimentally [90] as seen in Figure 2.2 (a) and (c). However, because the permeability and the drag coefficient were only listed for those two regimes, two separate cases for each velocity in the transitional regime were computed. The source term coefficients involved foam parameters (permeability and form drag coefficient) either from Darcy regime or Forchheimer regime. As seen in Figure 2.2 (b), the experimental points are close to the CFD results with Darcy coefficients only at low velocities. Then it exhibits a converging behavior towards the Forchheimer results.

The hydrodynamic entrance length was decided to be the point where the flow variables became constant along the foam axis. This criterion was applied by, firstly extracting data along the axis of the foam and calculating the percentage error with respect to the developed centerline velocity. When this error became lower than 0.01%, the flow was assumed to be fully developed. However, as can be seen in Figure 2.3, at the end of a velocity change along the foam axis, there is also a slight increase of velocity, downstream, after the fully developed region. This distance, at the end of the foam, can be named as the exit length since exit effects have taken place.

Both entry and exit lengths were found utilizing the 0.01% limit for all of the cases listed in Table 2.2. In Figure 2.4 (a) and (b), the plots of dimensionless entry and exit lengths versus the superficial velocities can be observed, respectively. The dimensionless lengths were found by dividing the dimensional values by the diameter of pipe. For each velocity in transition region, both results of the runs configured with Darcy and Forchheimer coefficients have been included. For both types of coefficients, lower velocities in this region exhibit proximity to Darcy region. However, as the velocity increases, only the solution with the Forchheimer coefficients shows a trend similar to that of the Forchheimer region. This fact is observable for both entry and exit lengths and the discrepancy is a result of the absence of a validated approach for transition in porous media.

The previous approaches by other researchers showed differences in the entry lengths. This can be attributed to the difference in the internal morphologies of the porous media [90]. For example, the function proposed by Vafai and Tien [51] returned a non-dimensional value of 0.01 at 0.0596 m/s, whereas it was found as 0.619 via simulation.

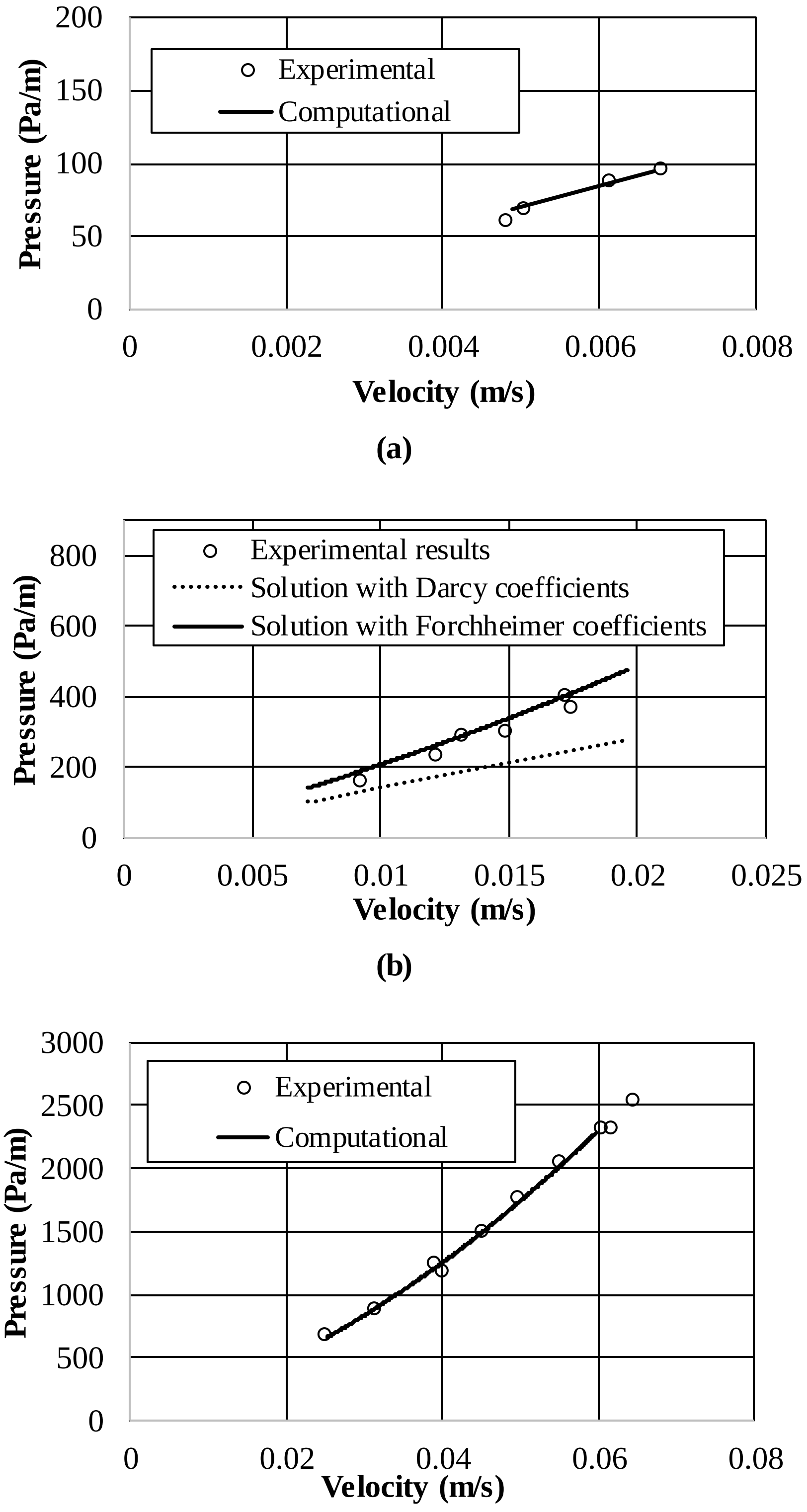

(a)

(b)

(c)

Figure 2.2 : Comparison of experimental and computational pressure drop-velocity couples: (a) Darcy region, (b) Transition region and (c) Forchheimer region.

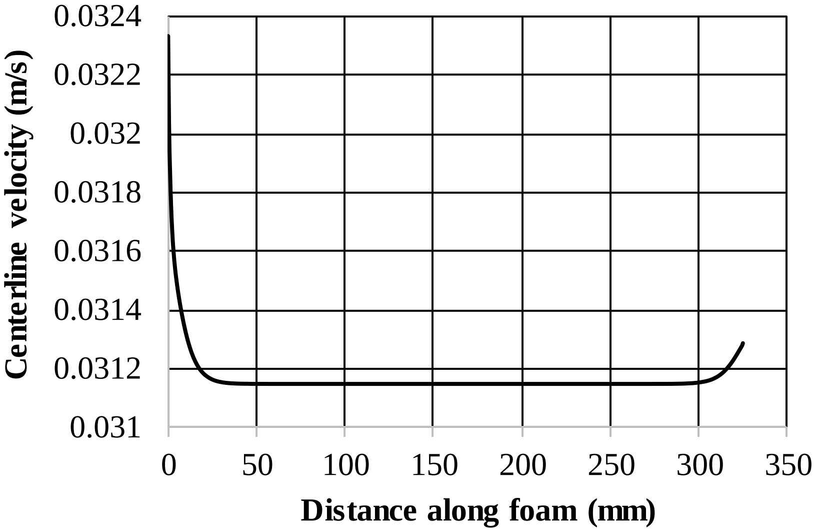

Figure 2.3 : Centerline velocity change for a case in the Forchheimer regime.

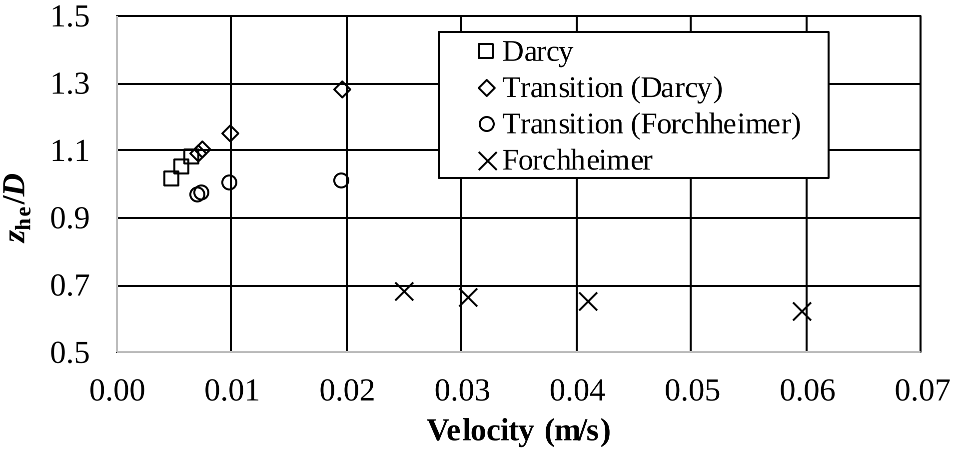

(a)

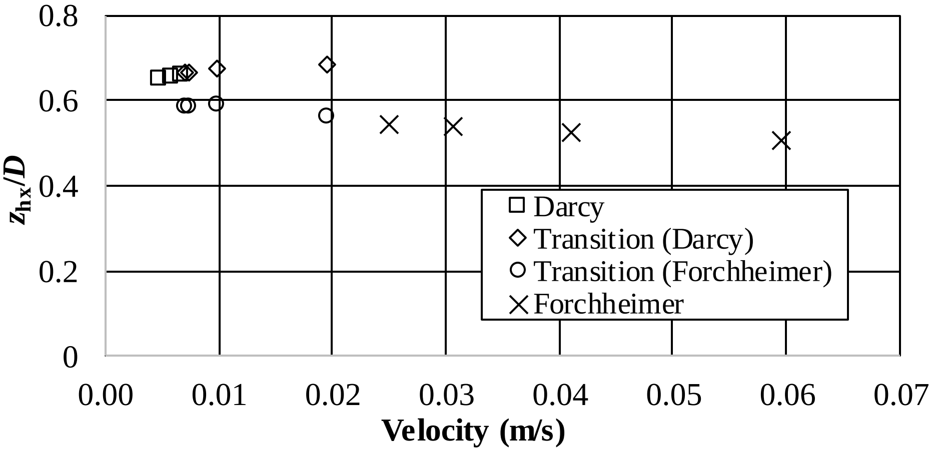

(b)

Figure 2.4 : (a) Hydrodynamic entry length, (b) Hydrodynamic exit length.

2.3 Heat Transfer Models

The two-energy-equation model has been chosen for running the cases computationally. This choice was made because the tube wall was exposed to a constant heat flux rather than kept at a constant temperature. The two equation model suggests that in the same elementary volume, the temperature of the solid matrix is different than the fluid temperature. Those two equations can be written as

$$\varepsilon \rho_{\mathrm{f}} c_{\mathrm{p_f}} \left[\frac{\partial T^{\mathrm{f}}}{\partial t} + \vec{v} \cdot \nabla T^{\mathrm{f}} \right] = \nabla k_{\mathrm{eff}}^{\mathrm{f}} \cdot \nabla T^{\mathrm{f}} + h_{\mathrm{sf}} \sigma_{\mathrm{sf}} \left(T^{\mathrm{s}} - T^{\mathrm{f}} \right) \tag{2.4}$$

$$\left(1-\varepsilon\right) \rho_{\mathrm{s}} c_{\mathrm{s}} \frac{\partial T^{\mathrm{s}}}{\partial t} = \nabla k_{\mathrm{eff}}^{\mathrm{s}} \cdot \nabla T^{\mathrm{s}} - h_{\mathrm{sf}} \sigma_{\mathrm{sf}} \left(T^{\mathrm{s}} - T^{\mathrm{f}} \right) \tag{2.5}$$

where superscripts f and s denote fluid and solid, h_{sf} is the heat transfer coefficient between solid and fluid and σ_{sf} is the surface area density.

2.3.1 Steady-state heat transfer model

For all of the steady-state runs, the flow in the porous zone was considered laminar because the velocities in Darcy and Forchheimer regimes were chosen. The flow structure in the remaining zones of the computational domain was as listed in Table 2.2. ANSYS Fluent was again used to run flow and heat analysis. SIMPLE was chosen as the pressure-velocity coupling method. The absolute convergence criterion was 10^{-6} for all of the dependent values for flow equations. In order to save time, the flow runs was allowed to converge, then only the energy model was switched on and the model was run until the convergence reached 10^{-12}. The same mesh explained in Section 2.2 was used.

Non-thermal equilibrium model explained above was employed in order to achieve more accurate results. This model required a surface area density (σ: m^2/m^3) for the porous zone and heat transfer coefficient from solid to liquid (h_{sf}).

The surface area density was calculated using the correlation found by Dukhan and Patel [92] for 20-ppi metal foams,

$$\sigma = 442.20 \ln(1-\varepsilon) + 2378.62 \tag{2.6}$$

where ε is the porosity. σ was found to be 1476.43435 m^2/m^3.

The heat transfer coefficient for the non-thermal equilibrium model, h_{sf} can be estimated employing the method proposed by Kuwahara et al. [93],

$$\frac{h_{sf} d_{ch}}{k_f} = \left(1 + \frac{4(1-\varepsilon)}{\varepsilon}\right) + \frac{1}{2}(1-\varepsilon)^{1/2} \mathrm{Re}_{\mathrm{d_{ch}}}^{0.6} \mathrm{Pr}^{1/3} \tag{2.7}$$

Where d_{ch} is the microscopic characteristic length. In this case, it was chosen as the square root of the Darcy permeability.

Boundary conditions for each computational run were selected such that they would match their experimental counterparts. The inlet conditions corresponding to each case listed in Table 2.2 and the heat transfer coefficient for each case can be found in Table 2.3.

Table 2.3 : Boundary conditions and the heat transfer coefficient.

Regime	Inlet Velocity (m/s)	Heat Flux (W/m^2)	h_{sf} (W/m^2K)
Darcy	0.0123	12000.37	4196.85
	0.0147	12032.61	4293.71
	0.0168	12032.61	4372.93
Transition	0.0181	11841.35	4416.98
	0.0188	11841.35	4444.45
	0.0250	21077.62	4647.77
	0.0494	21077.62	5303.30
Forchheimer	0.0633	21077.62	5616.99
	0.0774	21077.62	5907.34
	0.1036	21077.62	6395.26
	0.1502	21077.62	7157.52

2.3.2 Oscillating heat transfer model

Because the model for the oscillatory flow and heat transfer had to be time-dependent, the simulation required a substantial CPU time. Therefore, instead of a 3D geometry, 2D and axisymmetric model was prepared. However this model also included the annular jackets for the cooling water from the thermostats. The oscillation velocities crossed the borders of demarcation between laminar and turbulent regimes, as will be discussed in the results section of the experimental study of oscillating flow. Therefore, a turbulence model had to be employed and only one oscillatory flow configuration was studied because of the fidelity issues of the model to be stated later.

3. FLOW EXPERIMENTS AND RESULTS

3.1 Qualification of the Test Set-up Using Packed Beds of Mono-Sized Spheres

Figure 3.1 is a generic experiment schematic for one-dimensional steady flow through packed spheres of 1- and 3-mm diameters and 20-ppi metal foam. The test setup can be divided into three main sections; first part where the inlet pressure is introduced, second part including test section where pressure difference is measured, and a third part where water is collected. All the components listed in the caption of Figure 3.1 were used for both packed beds of 1- and 3-mm spheres. In addition, for metal foam experiments, a two-stage pump and a larger collecting tank was used to observe high velocities.

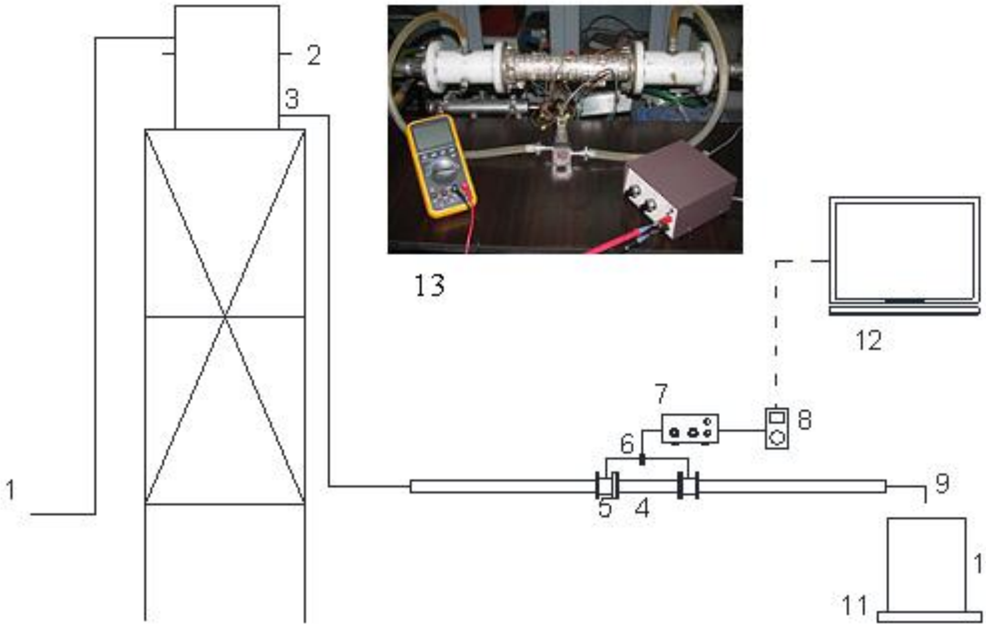

Figure 3.1 : Schematic of experimental setup: 1. Water network, 2. Discharges for constant water level supply tank, 3. 50-liter elevated tank, 4. Test section (Packed bed),5. Polyethylene tube, 6. Differential pressure sensor, 7. Carrier demodulator, 8. Multimeter, 9. Outlet, 10. 50-liter collecting tank, 11. Mass scale, 12. PC, 13. Photograph of the test section.

Because the main objectives of this study are mainly focused on metal foam, before starting the metal foam experiments, the functionality of the experiment setup had to be tested, and the results compared to those by [76]. The test was conducted using packed beds of 1- and 3-mm spheres. In addition, as will be mentioned in the following section, the pressure-velocity relation of at least one of the packed beds was required for experimenting on the metal foam at very low flow rates.

The test section, as shown with number 4 on Figure 3.1, comprised a 325-mm-long stainless steel tube with an inner diameter of 51.4 mm and with flange connections, stainless steel spheres with diameters of 1 or 3 millimeters (actual diameters were 1.14 mm and 3.03 mm) and two wire mesh screens with 0.6-mm openings, one of which was welded on one end. Before installing the test section, the mono-sized spheres were poured into the tube and shaken to avoid excessive voids as seen in Figure 3.2 (a) and (b). The open end of the tube was then closed manually with the other screen. Then, for positioning between polyethylene tubes with the same inner diameters as shown in Figure 3.1, nuts and bolts were used. In addition, fiber gaskets were used at the interfaces between components against leakage.

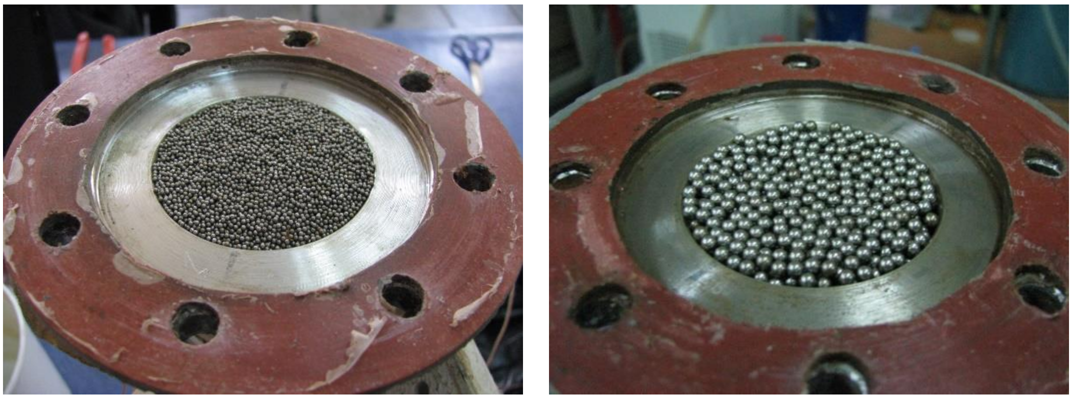

(a) **(b)**

Figure 3.2 : Packed beds of (a) 1-mm steel spheres, (b) 3-mm steel spheres.

The porosity of each medium was found by weighing the spheres inside the test section and using the volume of the porous region. The porosities of the 1-mm and 3-mm spheres were 35.01% and 36.59%, respectively:

$$\varepsilon = \frac{\forall_{\text{void}}}{\forall_{\text{total}}} = 1 - \frac{\forall_{\text{spheres}}}{\forall_{\text{total}}} = 1 - \frac{m_{\text{spheres}} / \rho_{\text{spheres}}}{\forall_{\text{total}}} \qquad \textbf{(3.1)}$$

The flow rate provided by the elevated tank which is explained in detail in the following section was practically constant (less than 4% variation). This setup could produce and hold very low water speeds (starting at 3.6×10^{-5} and 2.9×10^{-5} m/s for the 1- and 3-mm spheres, respectively). For high flow rates, water was supplied to the porous medium directly from a water tap using switching valves and 10-inches-high water filters with different pore sizes connected in series (Figure 3.3).

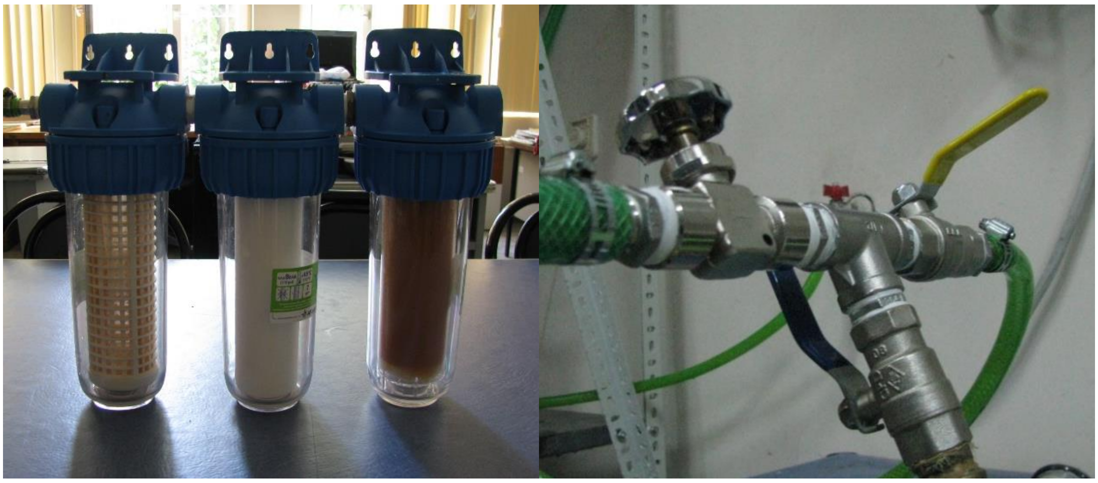

(a) **(b)**

Figure 3.3 : (a) Sediment filters connected in tandem, (b) Plumbing before the test section.

During the steady flow of water through the porous medium, pressure drop occurred due to viscous and inertial losses. The pressure loss was measured using Validyne differential pressure sensors, model DP15 and DP45. The choice of the sensors was based on the range of equipment. Model DP15 was mostly used at higher levels of difference whereas DP45 was used for much lower values. The sensor was powered by a Validyne CD15 carrier demodulator which generated an analog signal output between 0 and 10 V. This output was measured using a voltmeter.

For calculating the flow rate and velocity, the collected water was weighed and monitored during each experimental run. For measuring the mass of the collected water, three different mass scales were used as seen in Figure 3.4. The ranges of mass were 200 kg, 10.2 kg, 1.02 kg, and the precisions were 0.01%, 0.02%, 0.008% for the mass scales BASTER EKB 200, Precisa XT10200D, Precisa XT1020M, respectively. In addition, a stopwatch was used to measure the time during each steady-state run. For high flow rates, water was collected for about 4 minutes. The longest time for very low flow rates was 30 minutes. At each consecutive step with equal intervals of mass as observed on the digital screen of the scale, voltage reading from the voltmeter was recorded so as to average the voltage values and convert them into pressure depending on the range of the replaceable metal diaphragms placed in the pressure sensors.

(a) (b) (c)

Figure 3.4 : Mass Scales: (a) BASTER EKB 200 (Range: 200 kg, accuracy: 20 g), (b) Precisa XT10200D (Range: 10.2 kg, accuracy: 0.1 g), (c) Precisa XT1020M (Range: 1.02 kg, accuracy: 0.001 g).

The uncertainties in length of the porous region, diameter of steel balls and in diameter of the stainless steel tube were 0.18%, 1.0% and 0.04%, respectively.

The differential pressure sensor model DP15 had an accuracy of ±0.25% of full scale. Sensor DP45 had an accuracy of ±0.5% of full scale. The following average estimates were obtained: for the pre-Darcy region, the uncertainty in the pressure drop had a minimum of 0.49% and a maximum of 1.56%. For all other flow regimes the uncertainty in the measured pressure drop had a minimum of 0.13% and a maximum of 1.01%. The uncertainty of velocity, which was a quantity derived using mass scales, stopwatch, a thermometer for the current temperature and a caliber could be calculated by employing the method by [94].

3.1.1 Results of the qualification experiments

In total, 274 pressure drop-velocity pairs were obtained - 55 for the 1-mm 219 for the 3-mm spheres [95]. Figure 3.1 (a) and (b) are plots of the pressure drop over length vs. average velocity for 1- and 3-mm packed spheres. The pressure drop for the 1-mm spheres is higher than that for the 3-mm spheres. For example, at about a velocity of 0.05m/s, the pressure drop for the 1-mm spheres is about five times higher compared to that for the 3-mm spheres. This is expected, since the packing is denser in the case of the 1-mm sphere resulting in smaller flow passages, even though the porosities are practically the same for the two porous media. In addition, the winding of flow passages is considerable greater in the case of the 1-mm spheres, which is likely to increase resistance to flow.

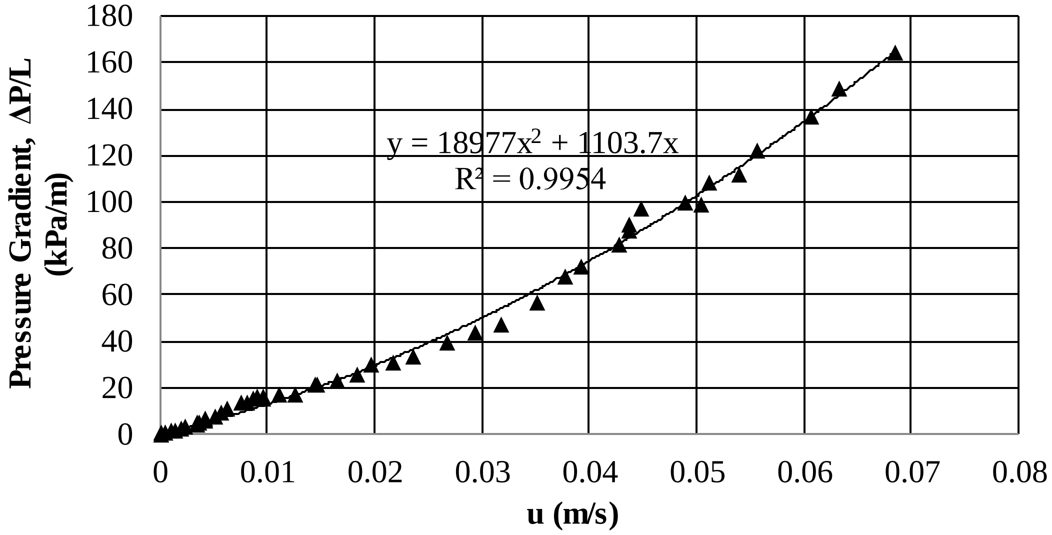

(a)

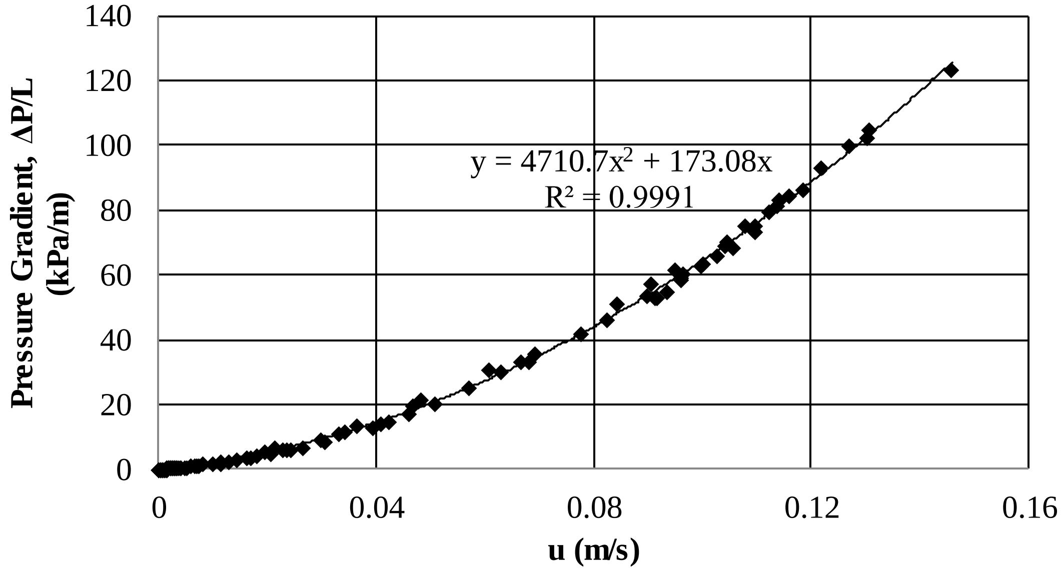

(b)

Figure 3.5 : Linear pressure gradient plots for (a) 1-mm (b) 3-mm packed spheres.

The wall region also has an effect. [11] indicated that the porosity of their packed bed of spheres was close to 1 and decreased to 0.36 inside the bed, and that the porosity got stabilized at a distance of about 3.5 particle diameters from the wall. This means that for the wall region with a porosity of about 1 extended 3.5 and 10.5 mm for the 1- and 3-mm spheres. Since both kinds of spheres occupied the same steel tube, it can be inferred that the wall region for the 3-mm spheres was three times larger allowing less pressure drop.

The behavior in these plots is characteristic for pressure drop in porous media: the pressure drop increases in quadratic fashion with velocity. Quadratic curve fits of the data are shown with very good correlation factors, R^2. By comparing the curve-fit equations to the Forchheimer equation (Equation (3.2)), values of the permeability and Forchheimer coefficient are obtained. These values are listed in Table1and will be discussed later.

$$\frac{\Delta p}{L} = \frac{\mu}{K} u + \frac{\rho F}{\sqrt{K}} u^2 \qquad \textbf{(3.2)}$$

Where Δp is the static pressure drop, L is the length of the porous medium in the flow direction, μ is the fluid viscosity, and the superficial velocity u is calculated by dividing the mass flow rate through the porous medium by the cross-sectional flow area and the density of the fluid ρ.

The format of Figure 3.5 does not display various flow regimes and transition among them. The format of Figure 3.6 (a) and (b), and Figure 3.7 (a) and (b) are more suitable for such purpose. In these figures the reduced pressure drop $\Delta p/Lu$ versus velocity is plotted - Figure 3.6 (a) and (b) for 1-mm case, while Figure 3.7 (a) and (b) are for the 3-mm case. Various flow regimes are discernable by ascertaining the values of velocity at which there are clear changes in the slope of the reduced pressure-drop data. In essence, similar treatment was performed by [8]. There are other preferences as to how the flow regimes should be identified. For example, [12] used the pore Reynolds number (based on the capillary model) for marking transition from laminar to turbulent regimes.

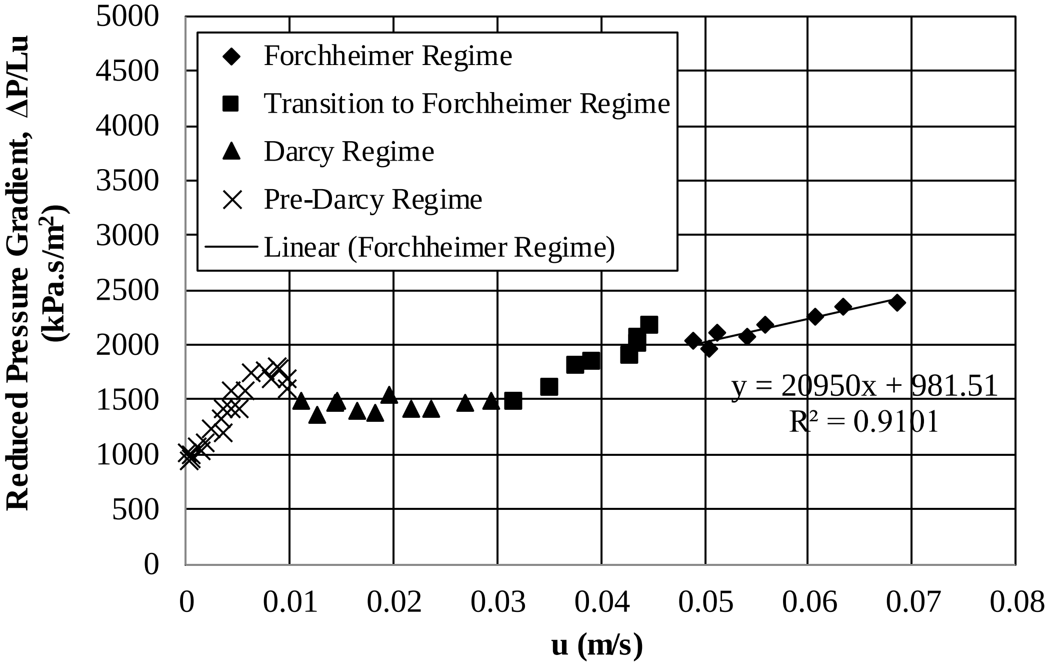

(a)

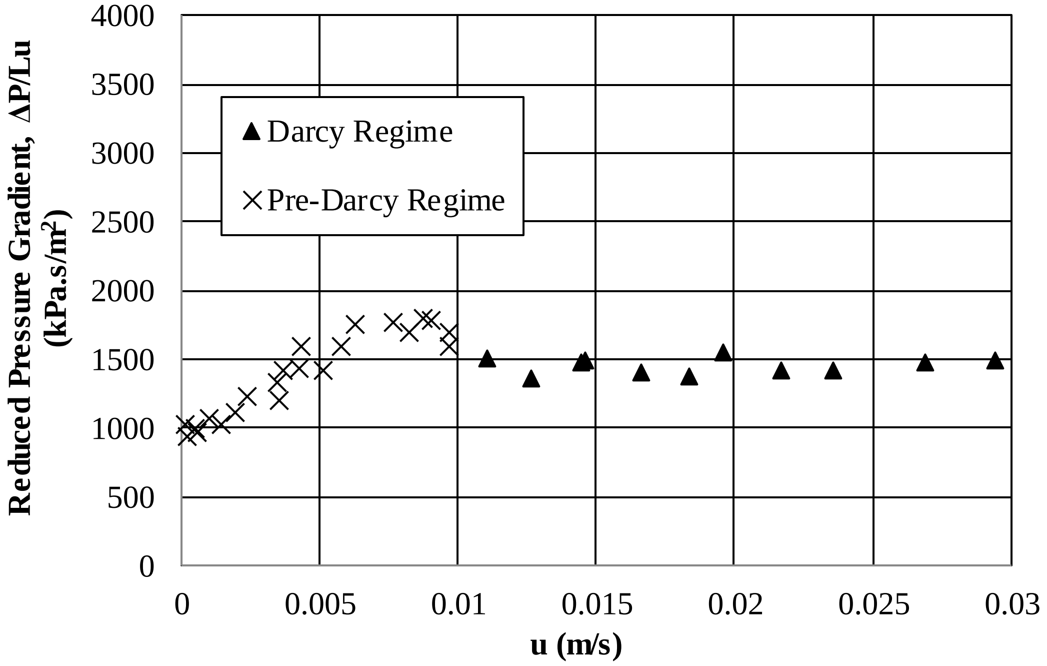

(b)

Figure 3.6 : Reduced pressure gradients versus average velocity for 1-mm spheres. Uncertainty in reduced pressure drop is 1.11% in the pre-Darcy regime and 0.70% in all other regimes: (a) Complete velocity range (b) Darcy and pre-Darcy regimes only.

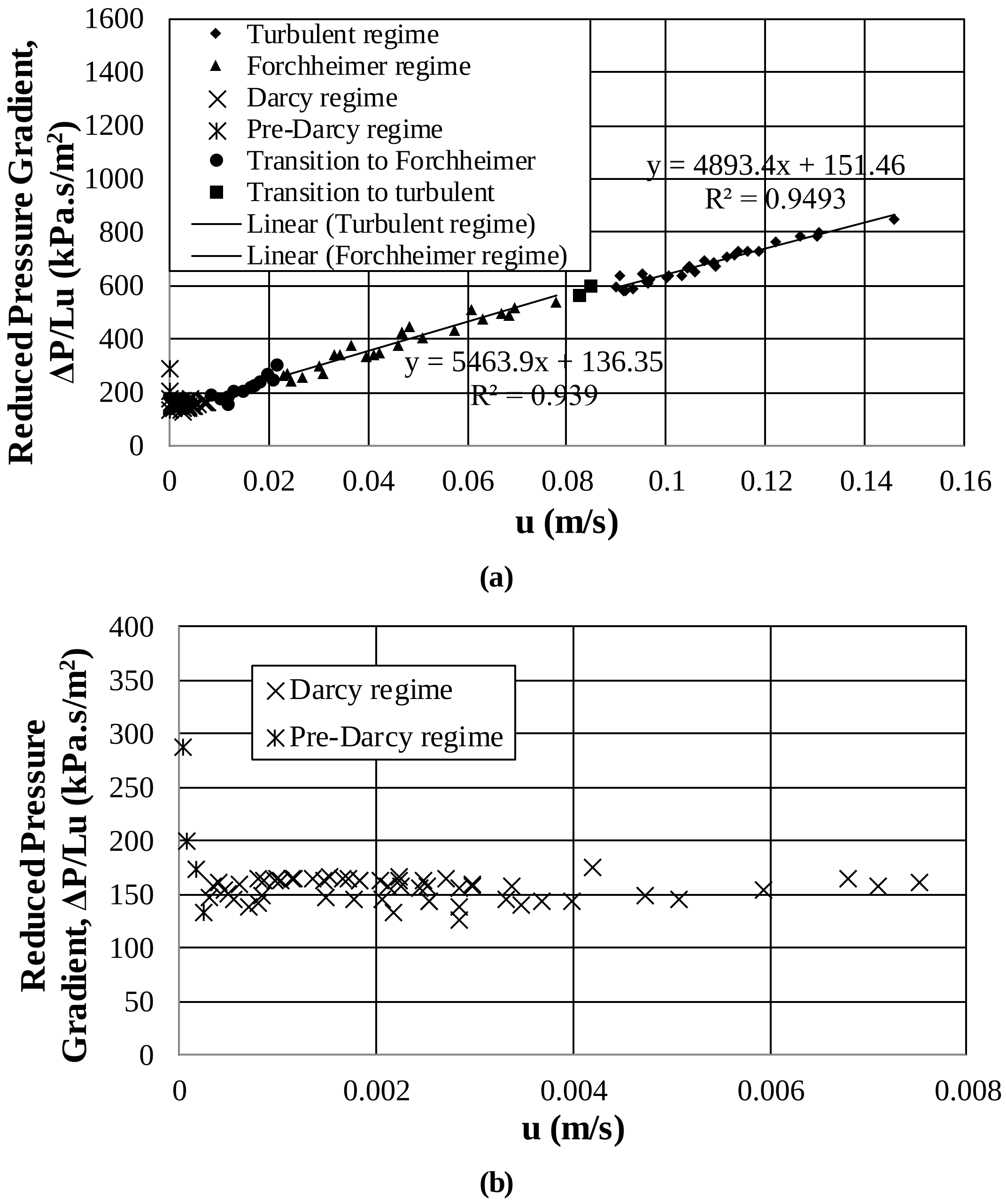

Figure 3.7 : Reduced pressure gradients versus average velocity for 3-mm spheres. Uncertainty in reduced pressure drop is 1.11% in the pre-Darcy regime and 0.70% in all other regimes: (a) Complete velocity range (b) Darcy and pre-Darcy regimes only.

For the 1-mm spheres and for very low velocity, a pre-Darcy regime is identified in Figure 3.6 (a) and expanded in (b). Measurements in this flow regime were possible because of the relatively high pressure drop for these small spheres offering a lot of resistance to flow. The pre-Darcy regime is not clearly understood and, to the knowledge of the authors, has rarely been presented in the literature. The study [9] included this regime and stated that the pre-Darcy regime prevailed over a relatively wide range of Reynolds number compared to the Darcy regime. While the behavior of the reduced pressure drop as a function of velocity seems to be unusual in this regime, it will be shown later that choosing an alternative way of displaying and interpreting pressure-drop data actually brings to light a clearly identified behavior in this regime.

The pre-Darcy regime ends at about 0.01m/s, and the Darcy regime begins, Figure 3.6 (b). The purely viscous Darcy regime is identified by a constant value of the reduced pressure drop. There is then a transitional regime shown by the red-square data points, which leads to the Forchheimer regime shown by the blue-diamond data points starting at about 0.05m/s. [11] indicated that any flow transition in porous media is expected to be gradual. No turbulent flow regime is encountered for the 1-mm set of data.

Figure 3.7, parts (a) and (b) are for the 3-mm spheres. For this case, only few points are seen to lie in the pre-Darcy regime, as more clearly visible in part (b). Extensive measurements in this flow regime were impossible because of the relatively low pressure drop for these relatively large spheres offering less resistance to flow as compared to the 1-mm spheres. The lower bound of the Darcy regime is at about a velocity of 2×10^{-4} m/s, while the upper bound is at about 7×10^{-3} m/s. There is then a transitional regime shown by the solid-circle data points, which leads to the Forchheimer regime shown by the triangle-shaped data points starting at about 0.02 m/s. For this porous medium, a regime beyond the Forchheimer regime was obtained, which is likely a turbulent flow regime. In this regime, and similar to the Forchheimer regime, the reduced pressure drop is seen to be a quadratic function of the velocity. [8] showed that turbulent flow was described by the Forchheimer equation but with different coefficients (permeability and Forchheimer coefficient). It has also been theoretically shown that the velocity dependence of the pressure drop in porous media subjected to turbulent flow is second order [31].

From Figure 3.6 and Figure 3.7, it is possible to calculate values of the permeability (K) and the Forchheimer coefficient (F) in each of the regimes beyond the Darcy regime, for the two porous media. The obtained values are shown in Table 3.1. The Forchheimer coefficient obtained for the 1-mm spheres is 0.54, which is very close to the 0.55—the value obtained by [96], and is well accepted in the porous-media literature. It is clear that the same porous medium exhibits different permeabilities and Forchheimer coefficients in different flow regimes. It is also clear that when using the whole dataset to calculate the permeability and the Forchheimer coefficient, significantly different values for these properties are obtained. Similar observations were made by [27] for fibrous highly porous media.

The experimental pressure-drop data were compared to the Ergun relation, Equation (3.3), and the coefficients A and B were obtained in the various flow regimes for the two porous media, as listed in Table 3.2. In the Darcy regime, A had the values of 147.2 and 152.1 for the 1- and the 3-mm spheres, respectively. These two values are very close to the one reported by Ergun, i.e., 150, and significantly different from 180 recommended by [97]. Divergent values are obtained in the other flow regimes. In [8], who tested spheres of various diameters, A exhibited some variations with diameter and changed for the turbulent flow; more specifically, A was higher for turbulent flow, which is confirmed by the current study for the 3-mm spheres.

$$\frac{\Delta p}{L} = A\frac{(1-\varepsilon)^2 \mu}{\varepsilon^3 d_{par}^2} u + B\frac{(1-\varepsilon)\rho}{\varepsilon^3 d_{par}} u^2 \qquad \textbf{(3.3)}$$

When compared to values obtained by other researchers for similar porous media (Table 3.2), the current study provides different values for A. The values presented by [8], for example, are considerably higher, while the value of A presented by [98] is close to what was obtained by the current study in the Darcy regime only. [98], who tested 1.12- and 4.99-mm glass spheres, showed that A remained practically constant for both cases, which is not the case for the current results.

As for the coefficient B of Ergun equation, differences were also observed. This coefficient ranged from 1.00 to 1.25 depending on the flow regime (excluding Darcy). This range is lower than the 1.8–4 range recommended by [97]. The values of B for the current data (for steel balls) are also lower than those reported by [8] and [98] for glass beads. In [8], who tested spheres of various diameters, B exhibited some variations with diameter and decreased for turbulent flow. The data of the current study seem to confirm this finding.

For porous media composed of spherical particles, the hydraulic radius theory of Kozeny-Carman provides the following relation for the permeability as a function of the structural parameters of the porous medium composed of spheres:

$$K = \frac{d^2\varepsilon^3}{36\kappa(1-\varepsilon)^2} \tag{3.4}$$

where d is the particle diameter (the sphere diameter), ε is the porosity of the porous medium and κ is the Carman–Kozeny constant. It is believed that κ is universal. For spherical particles κ is identically 5, [52]. Equation (3.4) itself is satisfactory but not general, [99], [52]. Table 3.2 shows the calculated values of κ for the two porous media of the current study as well as those for similar porous media from the literature. In general, the current data predicts lower values for this constant. Particularly, it is lower than 5.28 reported by [8], and lower than 5, the commonly accepted value for porous media composed of spherical particles, [52].

A non-dimensional form of the Forchheimer Equation may shed more light on the behavior of pressure drop, further confirm flow regime boundaries and consolidate pressure-drop data. In particular, it can be manipulated to yield

$$f = \frac{1}{\mathrm{Re}} + F \tag{3.5}$$

Where $f = (\Delta p / L)\sqrt{K} / \rho u^2$, and $\mathrm{Re} = \rho u \sqrt{K} / \mu$, both based on permeability. [96] also used the square root of the permeability as a length scale. Similar treatment was performed by [100]. Since the same porous medium exhibits different permeabilities in various flow regimes, as was shown above, one then must be careful as to which permeability should be used in the non-dimensional numbers of Equation (3.5). [7] stated that in the purely viscous Darcy regime, the exact nature of the flow field was determined by local internal geometry of the porous medium. As such, the permeability obtained in the Darcy regime represents the actual internal structure of the porous medium most accurately, and it is the one that must be used in the friction factor and the Reynolds number, as was done by [9]. In non-Darcy regimes, the actual internal structure of the porous medium is masked by effects such as boundary layers on solid surfaces, inertial cores, and wake formations.

Table 3.1 : Permeabilities and Forchheimer coefficients in different flow regimes

Regime	Darcy		Forchheimer		Turbulent		All Regimes	
d_{par} (mm)	1	3	1	3	1	3	1	3
$K \times 10^{10}$ (m^2)	6.90	64.23	10.00	73.48	NA	66.15	9.07	57.89
F	NA	NA	0.54	0.43	NA	0.39	0.57	0.37

Table 3.2 : Correlation coefficients

	Fand et al. (1987)		Comiti and Renaud (1989)	Current qualification study with the packed beds of spheres							
Regime	Forchheimer	Turbulent	Forchheimer	Darcy		Forchheimer		Turbulent		All regimes	
d_{par} (mm)	3	3	1.12	1	3	1	3	1	3	1	3
Kozeny-Carman	5.28	NA	3.89	4.09	4.22	2.82	3.69	NA	4.10	3.11	4.68
Ergun A	177.8	218.3	140	147.2	152.1	101.6	132.9	NA	147.7	112.0	168.7
Ergun B	1.90	1.63	1.68	NA	NA	1.12	1.05	NA	1.00	1.25	1.02

Based on experimental data and insights into the flow inside the pores, [7] calculated the friction factor and confirmed that it should behave according to

$$f = \frac{a}{\mathrm{Re}} + b \qquad \textbf{(3.6)}$$

where a and b are constants that depended on a characteristic length. The friction factor in Equation (3.6) has the same functional relationship to Reynolds number as it does in Equation (3.5). By comparing the two equations, the constants a and b assume the values 1 and around 0.55 (as will be shown later).

The experimental data of the investigation 1- and 3-mm packed spheres are plotted in the format of Equation (3.5) in Figure 3.8 (a) and (b), respectively. The classical behavior, [13,52,99], of the friction factor as a function of Reynolds number is displayed: the friction factor is generally inversely proportional to the Reynolds number. It is rather encouraging to see that the two datasets for the two porous media lie on the same curve, especially for Re_K greater than 0.1.

Flow regimes are identified again by comparing the experimental data to $1/\mathrm{Re}_K$ and to the constant 0.55. For the Darcy regime, the data must follow the curve $1/\mathrm{Re}_K$; departure from this function signifies the end of the Darcy regime. For the 1-mm spheres, Darcy regime extends from about Re_K of 0.29 to 0.77; as for the 3-mm spheres the bounds are approximately 0.02 and 0.6. For 1-mm spheres, the Forchheimer regime starts at about Re_K equal to 1.28, while it starts at about Re_K equal to 1.8 for the 3-mm spheres.

In the format of Figure 3.8, departure from the Forchheimer regime, and likely transition to turbulence, can be identified by the intersection of the experimental friction factor with the horizontal line f_K =0.50. This occurs at about Re_K =6 to 7. It should be noted that flow regime demarcation obtained using the friction factor was contrasted with those obtained using the reduced pressure drop of Figure 3.6, part (a) and (b), and was found to be consistent. The treatment of the pressure-drop data in the format of Figure 3.8, strongly suggests that, excluding the pre-Darcy regime, using the square root of the permeability (measured in the Darcy regime) as a length scale in the friction factor and the Reynolds number seems to consolidate the two data sets of 1- and 3-mm spheres.

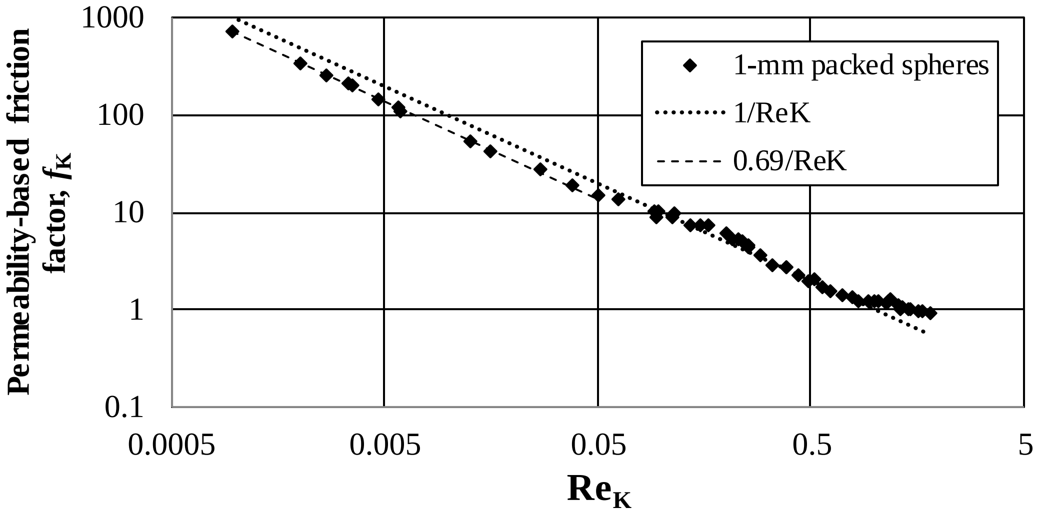

(a)

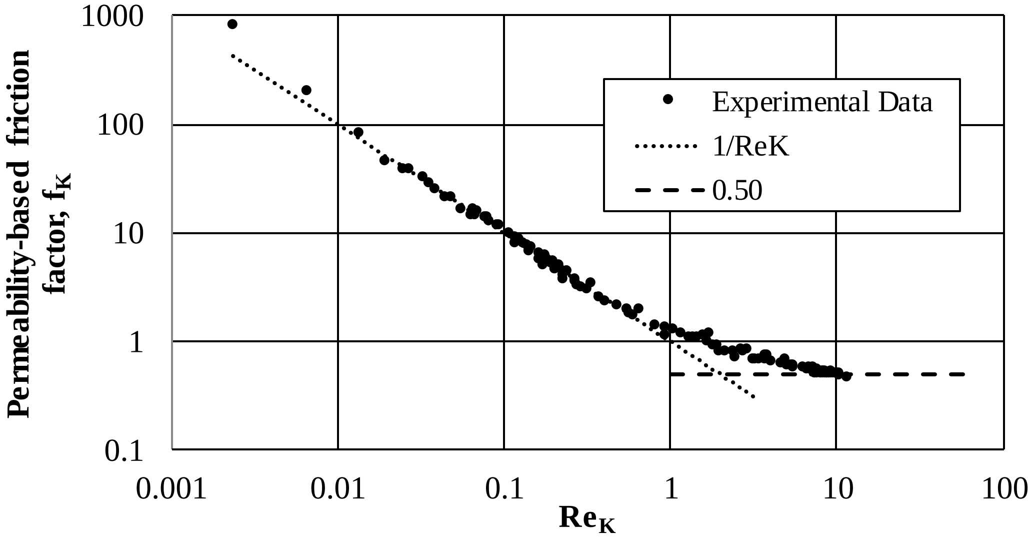

(b)

Figure 3.8 : Permeability-based friction factor versus permeability-based Reynolds number for (a) 1-mm and (b) 3-mm packed spheres.

To the knowledge of the current authors, there has been no correlation published for the behavior of resistance to flow in the pre-Darcy regime. And therefore, a new finding of the current study is that the pre-Darcy data for the 1-mm spheres are seen to follow a parallel line to $1/Re_K$ given by $0.69/Re_K$, as seen in Figure 3.8. This confirms the statement of [9]: in the pre-Darcy regime, the pressure drop seemed to be inversely proportional to the Reynolds number.

The demarcation of flow regimes of the current study is compared to what is available in the literature for similar porous media, in terms of the permeability-based Reynolds numbers in Table 3.6.

In terms of Re_K, the lower end of the Darcy regime of the current study, 0.02, is within the range of the one reported by [9], 0.013. However, the current study indicates that the Darcy regime persists over a wider range of Re_K. Other bounds of flow regimes are generally different from their counterparts reported by these two researches. [9] used glass beads, as opposed to the steel beads of the current investigation. This may be responsible for part of the disagreement. [8] did not provide permeabilities for his porous media. Flow regime demarcation was given only in terms of the particle-diameter-based Reynolds number Re_d. The regime boundaries obtained by the current authors are seen to be very different from those reported by [8] for glass beads.

The literature on porous media does not provide information regarding a) flow regime boundaries for the 1-mm spheres case and b) the upper boundary of the pre-Darcy regime for any porous media. The findings of the current study in these areas are included in Table 3.6.

3.2 Steady Flow in Metal Foam

A schematic of the experimental setup is shown in Figure 3.1. At the heart of the set-up, the stainless steel test section was replaced with a pipe made from aluminum alloy (6061-T6) having an inner diameter of 50.80 mm, a wall thickness of 6.35 mm and a length of 325 mm. Commercial aluminum foam (6101-T6 alloy), manufactured by ERG Materials and Aerospace, having 20 pores per inch and a porosity of 87.6% was brazed to the inside surface of the tube.

The test section was connected to two 50.8-mm-diameter 190-mm-long polyethylene tubes at its two ends using specially-designed flanges. Pressure taps were drilled on these tubes (Figure 3.9). The outlets of the Polyethylene tubes were connected to stainless steel pipes 32 mm in diameter and 110 cm in length. A hose and a valve were used for connecting the outlet of one steel pipe to a 50-liter tank for collecting water over a known length of time for measuring mass flow rates.

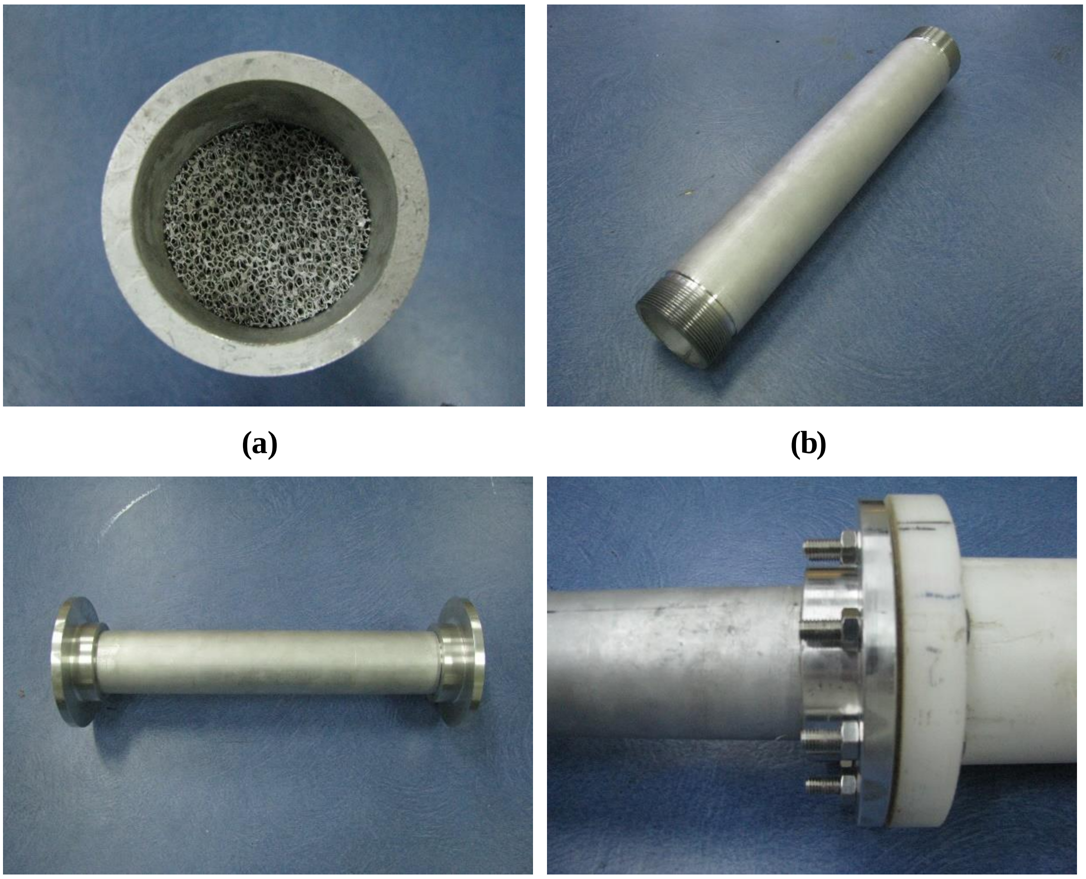

(a) (b)

(c) (d)

Figure 3.9 : Photographs of the test section: (a) 20-ppi metal foam brazed in an aluminum tube, (b) Aluminum tube with threaded ends, each 3-cm-long, (c) Flanges installed on the tube and (d) Assembly point of the flanges and the polyethylene tube.

An elevated plastic tank (diameter 41 cm, height 44 cm) with a network of hoses and valves, that guaranteed a constant water height (33.2 cm) in the tank at all times, supplied water to the foam in the test section. To increase potential energy, and thus achievable flow rates, this supply tank was elevated 3.5 m from ground level via a platform. Heavily-filtered tap water was supplied to the tank using a 1.27-cm hose. Four 1.90-cm outlet houses were attached to the tank at a height of 36.3 cm from the bottom of the tank. The supply line was positioned 41 cm from the bottom of the tank (3.7 cm higher than the four outlet hoses).

To supply constant-pressure flow to the porous medium, one end of another 1.90-cm hose was connected at 3.1 cm from the bottom of the tank, while the other end was connected to the plumbing containing the aluminum foam under investigation. This arrangement provided a constant water height of 33.2 cm in the tank during each experimental run. The flow rate provided by the tank was practically constant (less than 4% variation). The experimental rig was able to produce and hold very low water speeds (starting at 7.6×10^{-5} m/s). For high flow rates, a 2-hp pump (Standart Model No. TS268) was used, which produced average velocities of up to about 0.62 m/s through the foam.

The pressure drop was measured by two Validyne pressure-differential sensors, model DP15 and DP45. Each sensor could accommodate diaphragms having different designation codes - each suitable for a certain pressure-difference range. For example, diaphragm having codes 6–16, 6–22, 6–30 and 6–34, used with the DP45 low pressure-difference sensor, were for pressure ranges 0.35, 1.4, 8.6 and 22.0 kPa, respectively. When in use, each sensor was connected to a Validyne CD15 carrier demodulator, which provided 0–10 V as a direct-current output signal. The demodulator was connected to a multimeter where the voltage signals were read.

Each sensor/diaphragm combination had to be calibrated prior to use. Because there was a linear relation between the voltage outputs and corresponding pressure-difference values, according to the manufacturer's information, two pressure difference–voltage pairs were sufficient for calibration, one was taken at zero and one at the full scale (maximum) pressure difference. To obtain these two points, a stand with two plastic tubes and a measuring scale, all mounted vertically, was utilized. The two sides of the sensor were connected to the lower ends of the plastic tubes. To find the zero-pressure-difference point, water was added through the top ends of the tubes using a beaker to obtain equal heights in the two tubes. A syringe was used for fine adjustment of water levels. The hydrostatic pressures on both sides of the diaphragm were equal corresponding to zero pressure difference between the poles of the sensor, and the demodulator gave zero-volt signal. The water level in one of the tubes was then increased, until the pressure difference was equal to the maximum pressure difference obtainable by the installed diaphragm. The value of this pressure difference was calculated from the height of the water column, acceleration due to gravity (9.81 m/s^2) and the density of water (at the measured temperature at the time of calibration). This value corresponded to a 10-V signal—the maximum output reading. After calibration, the sensor was installed in the set-up, as shown in Figure 3.1.

For a given run, control valves were adjusted and water was allowed to flow into the foam until steady state was reached. A valve at the inlet provided fine control over the mass flow rate. Care was taken as to remove air bubbles from the system through the purger and/or by dismantling and reassembling parts of the set-up, as needed. At steady state and for a fixed valve opening (flow rate), water exiting the test section was captured in the collecting tank over a known period of time: approximately 50 s to 1.5 min for high flow rates, and 3–4 min for very low flow rates. Knowing the time and the mass of the collected water, the mass flow rate and the average flow velocity were determined. Several successive voltage readings (no less than 5) were taken during collecting a certain mass of water. These readings were averaged and recorded.

For very low flow rates, the pressure drop across the foam sample was too low to accurately measure using the pressure drop diaphragms. In order to comfortably measure that pressure drop, a known resistance was added in series with the foam. The resistance was a packed cylinder of 1-mm stainless steel spheres, Figure 3.10 (a) and (b).The packed bed had the same dimensions as the foam cylinder and had been known to provide relatively high pressure drop that can be easily and accurately measured using the existing pressure-drop sensors and diaphragms. The pressure drop in the foam was obtained using two measurements at each flow rate: (1) pressure drop across the foam and spheres, and (2) pressure drop across the spheres alone. The pressure drop in the foam was obtained by subtracting the pressure drop in the spheres from the pressure drop in the foam-sphere combination. A system of valves was used to direct the flow into the foam-spheres combination and the spheres alone.

Uncertainty in the reported data included error in the directly-measured quantities: length, mass, time and voltage; and propagated error in derived quantities, i.e., flow rate, pressure drop per unit length, reduced pressure drop, Reynolds number and friction factor [94]. The uncertainties in length and diameter of the metal foam tube were 0.33% and 0.04%, respectively. Three different mass scales were used over the range of flow rates. The precision in the low, medium and large scales were 0.01%, 0.02% and 0.008%, respectively.

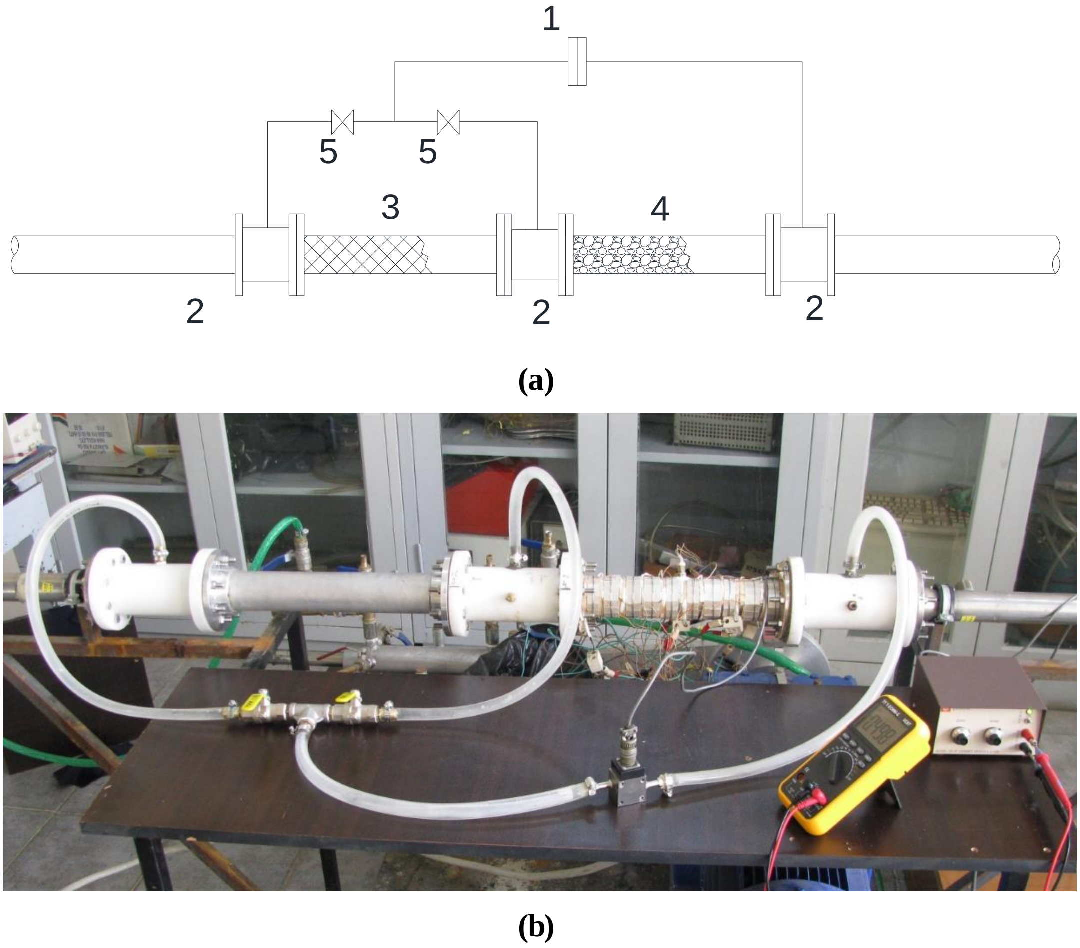

Figure 3.10 : Porous media connected in tandem: (a) Schematic of the tandem test sections: 1. Differential pressure sensor, 2. Polyethylene tubes, 3. Test section of the current study (Metal Foam), 4. Known porous medium (1-mm packed spheres), 5. Controlling valves. (b) Photograph of the porous media.

As for pressure drop measurements, two sensors were used (each with various diaphragms): DP15 and DP45 with accuracy of ±0.25% and ±0.5% of full scale, respectively. Sensor DP15 with diaphragm 3–24 which could measure up to 2200 Pa was used to obtain data in the pre-Darcy regime. The uncertainty in the pressure drop sensors was reported by the manufacturer and included effects of linearity, hysteresis and repeatability. The following average estimates were obtained: for the pre-Darcy region, the uncertainty in the pressure drop had a minimum of 0.49% and a maximum of 1.56%. For all other flow regimes the uncertainty in the measured pressure drop had a minimum of 0.13% and a maximum of 1.01%.

As an example of uncertainty in derived quantities, the uncertainty in the reduced pressure Dp/Lu had a contribution form uncertainties in Δp, L and u, and is given by [94]:

$$\frac{\delta_{\Delta p/Lu}}{\Delta p/Lu} = \pm\sqrt{\left(\frac{\delta_{\Delta p}}{\Delta p}\right)^2 + \left(\frac{\delta_L}{L}\right)^2 + \left(\frac{\delta_u}{u}\right)^2} \qquad \textbf{(3.7)}$$

which resulted in a maximum uncertainty of 1.56%. The uncertainty in the mass flow rate was obtained in the same manner, and had similar values as those obtained for the mass, due to the insignificant uncertainties in the density and the cross-sectional area. Uncertainty in other derived parameters is reported in the results section.

3.2.1 Results of the Steady-State Flow Experiments with Metal Foam

Figure 3.11, parts (a) and (b) are the plots of the pressure drop over length vs. average velocity for the metal foam. The behavior in this plot is typical for pressure drop in porous media: the pressure drop increases in quadratic fashion with velocity. Quadratic curve fit of the data is shown with a high correlation factor R^2 . The second-order Forchheimer equation (also known as the Forchheimer-extended Darcy equation and the Hazen–Dupuit–Darcy equation) is as shown in Equation (3.2).

The permeability of the porous medium, *K*, has units of area; it represents openness of the porous medium to fluid flow. The value of *K* varies widely among researchers for the same metal foam, [24]. The form-and-inertia drag coefficient *F*, known as the Forchheimer coefficient, is believed to be universal, or at least fixed for a given class of porous media, [23,24,51]. Like the permeability, *F* is strongly dependent on the internal structure of the porous medium.

By comparing the curve-fit equation of Figure 3.11 (a) to the Forchheimer equation, values of the permeability and Forchheimer coefficient are obtained. These values are listed in Table 3.3 and will be discussed later.

Table 3.3 : Permeability and Forchheimer coefficient for metal foam in different flow regimes.

	pre-Darcy	Darcy	Forchheimer	Turbulent	Al regimes
Permeability, $K\times10^{10}(m^2)$	NA	6.77	5.29	34.72	13.15
Forchheimer Coefficient, F	NA	NA	0.094	0.112	0.110

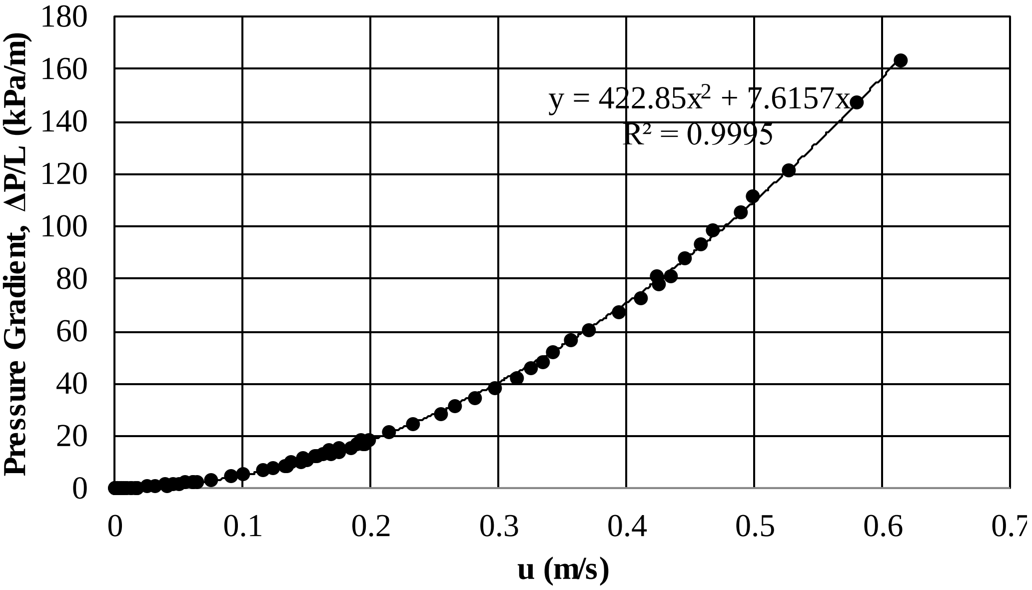

(a)

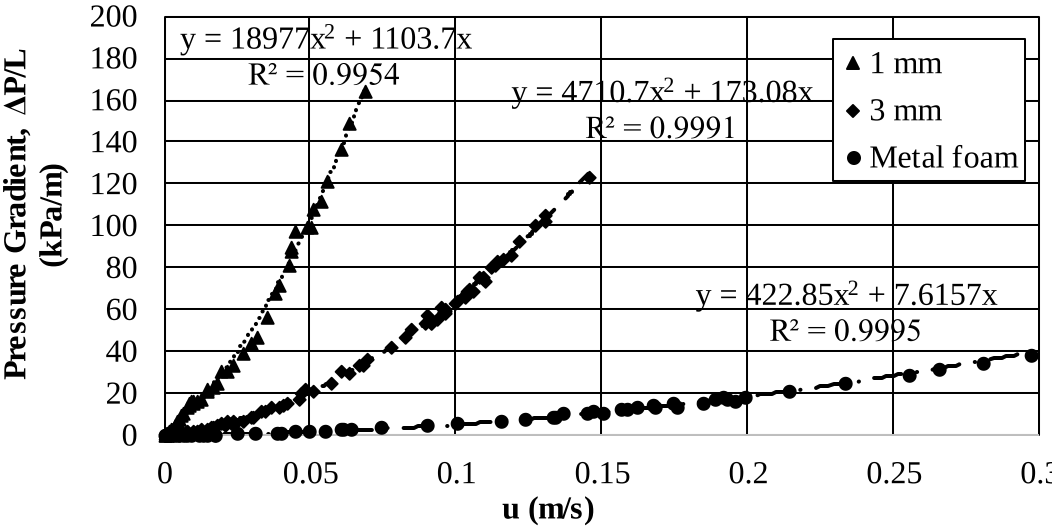

(b)

Figure 3.11 : Pressure gradient distributions: (a) Metal foam only, (b) 1- and 3-mm packed spheres, and Metal foam combined.

While common among some researchers, the choice of dependent variable of Figure 3.11 completely masks various flow regimes and transition among them. A slightly different form of the Forchheimer equation can be obtained by dividing both sides by the average velocity *u*, [2,18,22]:

$$\frac{\Delta p}{Lu} = \frac{\mu}{K} + \frac{\rho F}{\sqrt{K}} u \qquad \textbf{(3.8)}$$

This equation yields a positively sloping line in the Forchheimer regime and a horizontal line in the Darcy regime. As such, plotting the reduced pressure drop $\Delta p/Lu$ vs. velocity can clearly show various flow regimes. The choice of the average velocity as an independent variable provides an immediate physical sense of magnitude of how low or high the velocity should be in various flow regimes.

Figure 3.12 is a plot of the reduced pressure drop $\Delta p/Lu$ vs. velocity. Various flow regimes are discernible by observing where clear changes in the slope of the reduced pressure drop data. In essence, similar treatment was performed by Fand et al. [8] for packed spheres.

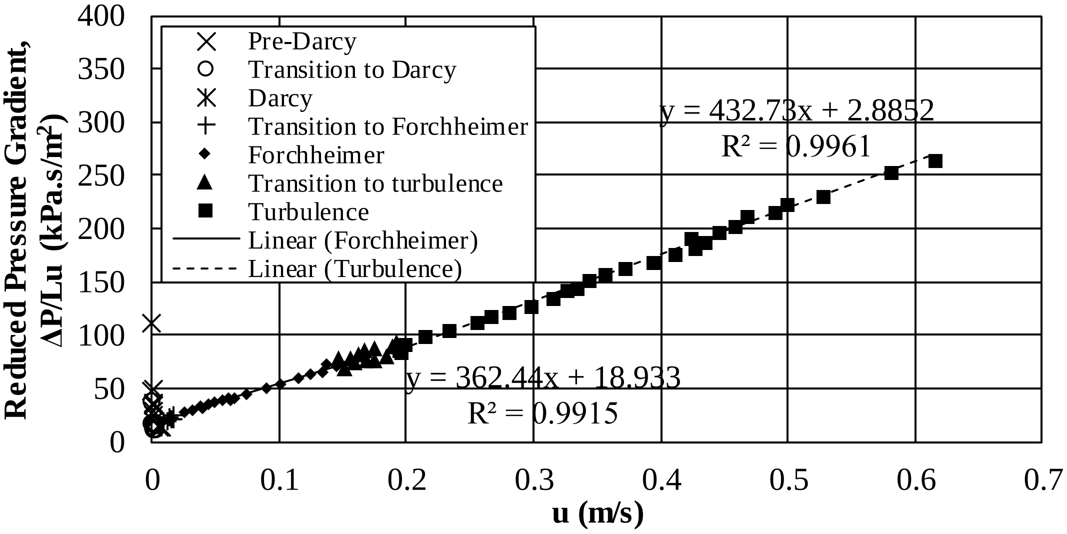

Figure 3.12 : Reduced pressure drop vs. average velocity. Uncertainty in reduced pressure drop is 1.11% in the pre-Darcy regime and 0.70% in all other regimes.

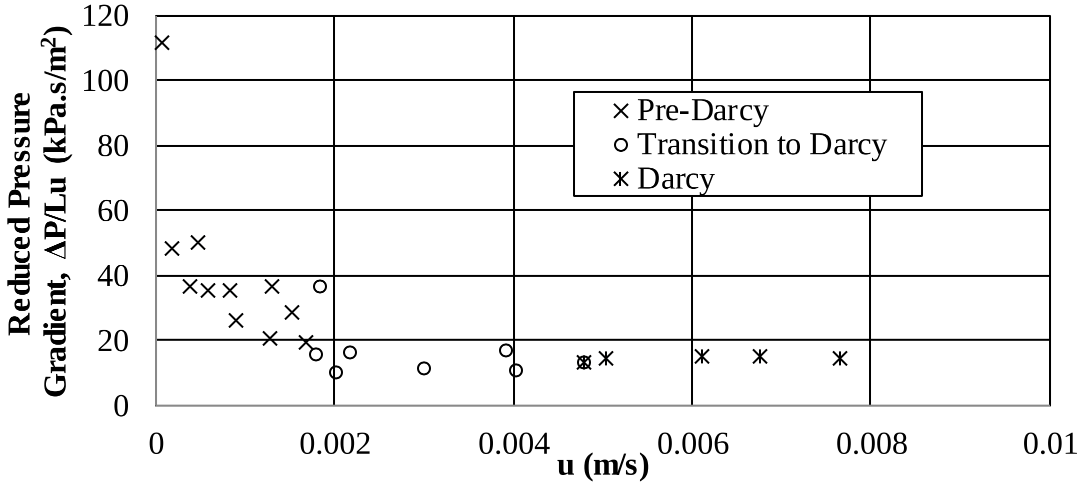

Figure 3.13 : Reduced pressure drop vs. average velocity: Darcy and pre-Darcy regimes. Uncertainty in reduced pressure drop is 1.11% in the pre-Darcy regime and 0.70% in Darcy regime.

For extremely low velocity, a pre-Darcy regime is identified, as shown in Figure 3.13, which is dedicated to the low velocity range. The pre-Darcy regime is not clearly understood and, to the knowledge of the authors, has never been presented in metal foam literature, most likely due to experimental difficulties in accurately measuring the rather small flow rates and pressure drops associated with it. According to Fand et al. [8], in this regime a fluid may exhibit non-Newtonian behavior; and the streaming potential generated by the flow can produce small counter currents along the pore walls in a direction opposite to the main flow direction. It may be postulated that these effects can be represented by a pressure-drop quantity δp that can be used to modify Darcy law to account for phenomena occurring in the pre-Darcy regime as follows:

$$\frac{\Delta p-\delta p}{L}=\frac{\mu}{K}u \qquad \textbf{(3.9)}$$

Equation (3.9) is subject to the following conditions,

- $\frac{\Delta p-\delta p}{L}<0,$ no flow.
- $\frac{\Delta p-\delta p}{L}>0,$ pre-Darcy flow.
- $\frac{\delta p}{L}=0,$ Darcy flow.

Similar treatment was presented in Bear [13] and attributed to Imray. Bolt and Groenevelt [101] also used similar treatment to account for electro-osmotic and capillary osmotic forces (or pressure drops) for flow of liquid solutions in porous media.

There is no precise information regarding the upper boundary of the pre-Darcy regime (or the lower boundary of the next flow regime, the Darcy regime) for metal foam, or any porous media for that matter. However, published Darcy-flow data for packed spheres indicate that the lower limit of Darcy flow is less than Re value of 10^{-5} [8]. For this limit, Re is based on the average (Darcy) velocity and the particle diameter. It is not an easy task to find an 'equivalent' particle diameter for the web-like structure of metal foam. The study of Kececioglu and Jiang [9], also for packed spheres, included a pre-Darcy regime, and stated that this regime prevailed over a relatively wide range of Reynolds number compared to the Darcy regime.

For the metal foam of the current study, the pre-Darcy regime seems to persist up until about 0.002 m/s, where a transition to Darcy regime begins, Figure 3.13. The purely viscous Darcy regime is identified by a constant value of the reduced pressure drop, which is a horizontal line corresponding to

$$\frac{\Delta p}{Lu} = \frac{\mu}{K} \tag{3.10}$$

The Darcy regime prevails for creeping or seepage flow; and the pressure drop is solely due to viscous drag provided by the surface of the solid phase of the foam. Because of low momentum, the flow engulfs and attaches to the surfaces of the ligaments of the foam. As such, wakes and inertial cores are non-existent, and the actual geometry of the internal structure of the foam is exposed and is directly 'experienced' by the flowing fluid. Dybbs and Edwards [7] stated that, in the Darcy regime, the exact nature of the velocity distribution was determined by local geometry. Because of this nature of flow in the Darcy regime, the permeability obtained in this regime is most closely related to the internal morphology of the foam, and it is likely to be constant for the same foam. The Darcy regime of the current foam is relatively narrow, extending from 0.004 to 0.007 m/s, approximately. For clarity purposes and because experimental data for very low velocities are rare, the obtained data for the pre-Darcy and Darcy regimes, as well as the transition between the two, are given in Table 3.4.

After Darcy regime, there is a transitional regime followed by the Forchheimer regime starting at about 0.02 m/s. Seguin et al. [11] indicated that any flow transition in porous media is expected to be gradual. Dybbs and Edwards [7] warned of the little consensus as to what the distinct flow regimes and transition points were beyond the Darcy regime.

After Darcy regime, there is a transitional regime followed by the Forchheimer regime starting at about 0.02 m/s. Seguin et al. [11] indicated that any flow transition in porous media is expected to be gradual. Dybbs and Edwards [7] warned of the little consensus as to what the distinct flow regimes and transition points were beyond the Darcy regime.

In the Forchheimer regime, flow energy dissipation becomes the sum of viscous and form (and inertia) drags. Boundary layers begin to develop near solid boundaries inside the porous medium and they become pronounced; an inertial core appears [7]. Kinetic energy degradation begins due to pore constrictions (open flow area reduction) and flow direction changes (to go around the ligaments of the foam). Nonetheless, the flow remains laminar and steady. The additional drags are captured by the term that has a second-order dependence on velocity in Equation (3.2). The Forchheimer regime extends to until about 0.14 m/s.

Table 3.4 : Actual pressure drop data for low-flow regimes.

Pre-Darcy		Transition to Darcy		Darcy	
u (m/s)	$\Delta P/Lu$ (kPa.s/m^2)	u (m/s)	$\Delta P/Lu$ (kPa.s/m^2)	u (m/s)	$\Delta P/Lu$ (kPa.s/m^2)
0.08×10^{-3}	111543	1.80×10^{-3}	15992	4.80×10^{-3}	13529
0.17×10^{-3}	48487	1.84×10^{-3}	36590	5.03×10^{-3}	14615
0.38×10^{-3}	36872	2.01×10^{-3}	10330	6.12×10^{-3}	15444
0.40×10^{-3}	36031	2.05×10^{-3}	29469	6.77×10^{-3}	15124
0.47×10^{-3}	50349	2.17×10^{-3}	16377	7.66×10^{-3}	14698
0.59×10^{-3}	35292	2.86×10^{-3}	24577		
0.77×10^{-3}	34730	3.00×10^{-3}	11453		
0.82×10^{-3}	35300	3.56×10^{-3}	18259		
0.90×10^{-3}	26101	3.91×10^{-3}	17076		
1.26×10^{-3}	15435	4.03×10^{-3}	11028		
1.27×10^{-3}	20860	4.35×10^{-3}	16260		

Beyond the Forchheimer regime, there seems to be a narrow transition regime (0.14–0.19 m/s), followed by a different regime starting at about 0.2 m/s, which is likely turbulent. In this regime, and similar to the Forchheimer regime, the reduced pressure drop is seen to be a linear function of the velocity. Fand et al. [8] showed that turbulent flow in packed spheres was described by the Forchheimer equation, but with different coefficients (permeability, K, and Forchheimer coefficient, F), Table 3.5. Skjetne and Aurliault [31] have also shown theoretically that the velocity dependence of the pressure drop in porous media subjected to turbulent flow is second order.

Table 3.5 : Permeability and Forchheimer coefficient in metal foam for various regimes

Regime	pre-Darcy	Darcy	Forchheimer	Turbulent	All Regimes
$K\times10^{8}$ (m^2)	NA	6.77	5.29	34.72	13.15
F	NA	NA	0.094	0.112	0.110

Both Darcy and Forchheimer regimes are laminar in nature, and the viscous-inertial transition from one to the other is within the laminar regime. Sometimes viscous-inertial and laminar–turbulent transitions are confused and/or used interchangeably [102]. Turbulent flow in porous media is highly chaotic and unsteady. The reader is referred to a two-part detailed study, [11,12], in which careful demarcation of transition from laminar to turbulent in porous media was given, along with physical explanation of the nature of turbulence in porous media based on intricate local measurements. Another detailed study addressing this issue was presented by Dybbs and Edwards [7].

Mechanisms influencing transition to turbulent flow in porous media include non-uniformity of pore size distribution, internal surface roughness, mixing of intersecting streams and separation of microscopic flow field from the internal local geometry. Rode et al. [10] stated that the fluctuations of the local velocity gradient in the turbulent regime were due to the passage of liquid aggregates. The dimension of the biggest aggregates was close to the average pore size, and the average dimension of the aggregates was about half the pore size, and that it did not depend on the Reynolds number. This phenomenon of aggregate formation and passage was considered a manifestation of turbulence but not necessarily fully-developed turbulence by Rode et al. [10]. There is some disagreement on transition to turbulence in porous media, [10]. Seguin et al. [12] indicated that, unlike open pipe flow, transition from laminar to turbulent regimes in porous media was gradual.

Using Figure 3.12, values of the permeability in the Darcy regime, and permeability and Forchheimer coefficient in each of the regimes beyond the Darcy regime can be calculated. The obtained values are shown in Table 3.5. It is clear that the same foam exhibits different permeabilities and Forchheimer coefficients in different flow regimes. It is also clear that when using the whole data set to calculate the permeability and the Forchheimer coefficient, significantly different values for these properties are obtained. Dukhan and Minjeur [27] have shown that K calculated in the Forchheimer regime was different from the one obtained in the Darcy regime for air flow in the same aluminium foam.

In a non-dimensional form, the Forchheimer Equation (3.2) gains the same form as Equation (3.5), or in general as depicted by other researchers, Equation (3.6).

In the non-dimensional variables f and Re, the square root of the permeability (of the Darcy regime) is utilized as a characteristic length. As to why the Darcy permeability should be used, Dybbs and Edwards [7] stated that in the purely viscous Darcy regime, the exact nature of the flow field was determined by the local internal geometry of the porous medium. As such the permeability obtained in the Darcy regime represents the actual internal structure of the foam most accurately, and it is selected as the characteristic length in the friction factor and the Reynolds number. Boomsma and Poulikakos [22] indicated that Reynolds number based on Darcy-regime permeability was the preferred parameter to indicate transition from Darcy to Forchheimer regime, since it gave the least divergent values for the three types of metal foam in their study.

There exist several opinions as what should be used as a characteristic length for correlating the pressure drop in metal foam. Bonnet et al. [28] used the cell diameter in place of the particle diameter in Ergun equation, while Dukhan and Patel [92] employed the reciprocal of the surface area density. By comparing a large set of correlations and experimental data from the literature, Edouard et al. [17] showed that the use of the pore (or cell) diameter of the foam as a characteristic length was not appropriate. The choice of a characteristic length for some porous media may be counterintuitive. For example, Kececioglu and Jiang [9] stressed that the appropriate characteristic length for packed spheres ought to be the square root of the permeability, not the sphere diameter.

It is established that the pressure drop for turbulent flow is second order in velocity, [8,31]. So Equation (3.6) is sufficient for correlating the friction factor in Turbulent flow. However, for the relatively high values of Reynolds number typical of turbulent flow, we expect the first term on the right hand side of Equation (3.6) (viscous contribution) to become negligibly small and so we can write

$$f = b \tag{3.11}$$

for turbulent flow. It is expected that b will be different for different porous media (different internal structure).

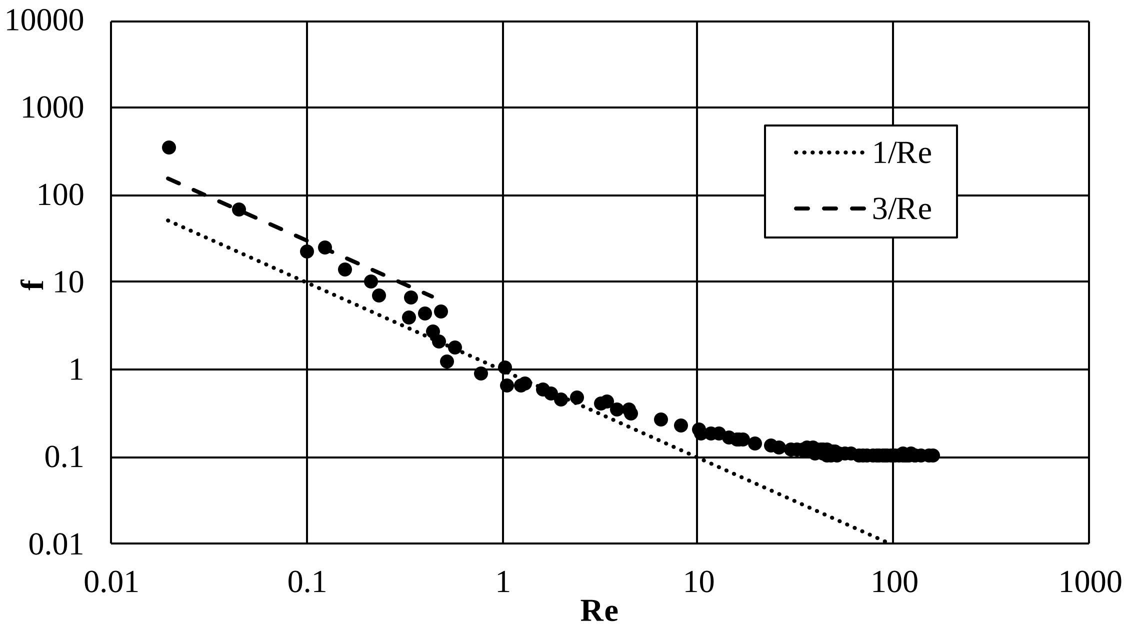

Figure 3.14 : Permeability-based friction factor vs. permeability-based Reynolds number for all flow regimes.

All of the experimental data of the current investigation is plotted as friction factor vs. Reynolds number in Fig. 6. The classical behavior, [13], of the friction factor as a function of Reynolds number is displayed according to Equation (3.6): the friction factor is generally inversely proportional to the Reynolds number.

Flow regimes are identified by comparing the experimental data to the 1/Re curve. For the Darcy regime, the data must follow the curve 1/Re as predicted by Darcy equation. Darcy regime extends from about Re of 1.2 to 1.9; the Forchheimer regime starts at about Re equal to 6.4 and ends at 37.5; while turbulent flow starts where about Re is 50. It should be noted that flow regime demarcation obtained using the friction factor were contrasted with those obtained using the reduced pressure drop of Figure 3.12 and Figure 3.13, and were found to be consistent.

The demarcation of flow regimes in terms of the permeability-based Reynolds numbers of the current study is compared to what is available in the literature, as shown in Table 3.6. Unfortunately, only two studies of flow in metal foam have transition information: Boomsma and Poulikakos [22] and Dukhan and Ali [30]—both included some points in the Darcy regime and transition to Forchheimer regime. In [22], the average velocity at which the transition took place was given, while the Darcy permeability as estimated from pressure drop plots and the Reynolds number marking the transition was calculated. As shown in Table 3.6, there is a disagreement between the bounds of the Darcy regime obtained by this study and those of Boomsma and Poulikakos [22] primarily due to difference in internal structure and porosity of [22] and [30]. There is also a disagreement between the current study and Dukhan and Ali [30], who used air. These comparisons will be explained in detail later.

The literature on fluid flow in packed-spheres porous media contains disagreement regarding transition among flow regimes and flow regime boundaries, e.g., [8,9]. The study of Kececioglu and Jiang [9] is selected for comparison since they presented their data in terms of the permeability-based Reynolds number. Fand et al. [8] used the Reynolds number based on the average sphere diameter for marking transition.

It is seen that demarcation of flow regimes in metal foam is very different from that in packed spheres, with transitions generally taking place at significantly higher Reynolds number for metal foam, except for transition to turbulent, which occurs at Re equals 50 for metal foam and at 72 for packed spheres. Seguin et al. [11] presented local instantaneous measurements of limited current intensity, along with spectral analysis of signal fluctuation, which enabled accurate determination of the end of the stable laminar regime. They noted that synthetic foam had a laminarising effect.

Table 3.6 : Flow regime boundaries of current and similar studies

		Pre-Darcy	Darcy	Forchheimer	Turbulent
Current Study, Metal Foam, Water	20 ppi, $\varepsilon = 87\%$	Re < 0.4	1.2 < Re < 1.9	6.4 < Re < 37.5	Re > 50.0
Boomsma and Poulikakos [22] water	10 ppi, $\varepsilon = 88\%$	NA	Re < 27.4	27.4 < Re	NA
	20 ppi, $\varepsilon = 69\%$		Re < 15.8	15.8 < Re	
	40 ppi, $\varepsilon = 61\%$		Re < 96.1	96.1 < Re	
Dukhan and Ali [30]air	10 ppi, $\varepsilon = 89\%$	NA	12.5 < Re < 29.2	29.2 < Re	NA
	20 ppi, $\varepsilon = 90\%$		12.5 < Re < 29.2	29.2 < Re	
Kececioglu and Jiang [9] 3-mm spheres, water	$\varepsilon = 40\%$	NA	0.013 < Re < 0.025	0.07 < Re < 0.48	Re > 72
Current Study, 1-mm spheres, Water	$\varepsilon = 35.0\%$	Re < 0.25	0.29 < Re < 0.77	1.28 < Re	NA
Current Study, 3-mm spheres, Water	$\varepsilon = 36.6\%$	Re < 0.02	0.02 < Re < 0.59	1.81 < Re < 6.2	7.16 < Re

3.2.1.1 The pre-Darcy regime

In Figure 3.14, the upper boundary of the pre-Darcy regime is at Re value of approximately 0.4. The literature on porous media does not provide any information regarding the upper boundary of the pre-Darcy regime for any porous media. While the behavior of the reduced pressure drop as a function of velocity seems to be unusual in the pre-Darcy regime, the behavior is easily discernible in the friction factor *f* vs. Reynolds number Re plot. Kececioglu and Jiang [9] stated that in the pre-Darcy regime, the pressure drop seemed to be inversely proportional to Reynolds number. This statement was based on experimental data obtained by these researchers for flow in packed spheres. For the current study, f seems to be inversely proportional to Re according to 3/Re, as suggested by the dashed line.

3.2.1.2 The post-Darcy regimes

The Forchheimer and turbulent regimes are probed according to Equations (3.6) and (3.11), respectively. Figure 3.15 is a plot of the friction factor as a function of the reciprocal of Reynolds number for the Forchheimer and turbulent regimes. The sheer ability of Equations (3.6) and (3.11) to capture the behavior of the friction factor as linearly dependent on the reciprocal of the Reynolds number in the Forchheimer regime is evident.

From the curve fits of the data in Figure 3.15, values for the adjustable parameters a and b of Eqs.(7) and (8)are obtained and listed in Table 4. For the coefficient a, Beavers and Sparrow [15] obtained 0.07 for nickel foam; and Paek et al. [103] 0.105 for aluminium foam. These values are comparable to 0.087 obtained for the Forchheimer regime of the current study. The coefficient *b* ranged from 0.26 to 0.79 for the sintered stainless-steel foam of Zhong et al. [25], which are different from those of the current study due to difference in internal structure of the foams.

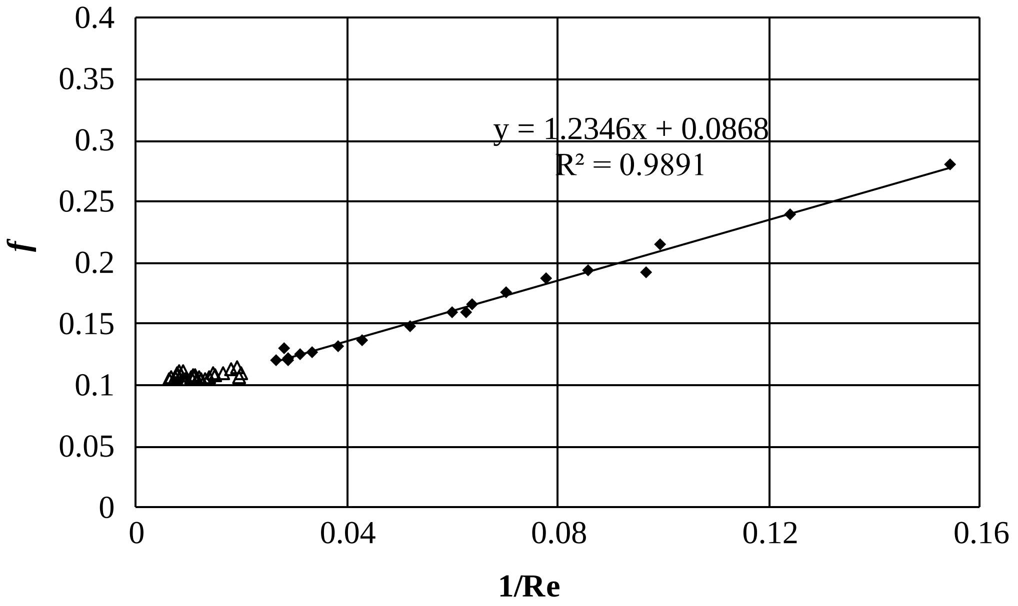

Figure 3.15 : Friction factor versus the reciprocal of Reynolds number.

3.2.1.3 Comparison to other studies

An expansive list of data sets (30 sets from 14 different studies) for pressure drop in metal foam was gathered from the literature, Table 3.7. The foam investigated in these sets was aluminium, nickel and steel. There is a good range of porosity variation for aluminum foam obtained by mechanical compression in the data sets. The pore density (ppi) ranged from 5 to 40. Some of the pressure-drop data was for water while others were for air flow. Other available data that would not provide any information such as data for foams having the same pore density and comparable porosities were not included. As mentioned above, only Boomsma and Poulikakos [22] and Dukhan and Ali [30], included some points in the Darcy regime and transition to Forchheimer regime. A set for pressure drop in packed beds of spheres [9], and a set for pressure drop in compressed steel fibers [15] are also included for reference.

Table 3.7 : Correlation coefficient *b* for various studies.

Authors	Medium	Fluid	Porosity (%)	Pore density (ppi)	b
Current Study	20 ppi Aluminum foam	Water	87	20	0.087
Zhong et al. [25]	Sintered steel	Air	38	N/A	0.706
	Sintered steel	Air	46	N/A	0.743
Mancin et al. [18]	Aluminum foam	Air	90	10	0.074
	Aluminum foam	Air	96	10	0.102
Paek et al. [103]	Aluminum foam	Air	94	N/A	0.105
Beavers & Sparrow [15]	Nickel foam	Water	N/A	N/A	0.074
	Compressed stainless steel fibers	Water	N/A	N/A	0.132
Hamaguchi et al. [104]	Nickel foam	N/A	N/A	N/A	0.076
Vafai & Tien [51]	Metal foam	Water	N/A	N/A	0.057
Hwang et al. [23]	Compressed aluminum foam	Air	80	N/A	0.068
	Compressed aluminum foam	Air	70	N/A	0.065
Antohe et al. [2]	Compressed aluminum foam	Air	72	N/A	0.371
	Compressed aluminum foam	Air	50	N/A	0.838
	Compressed aluminum foam	Air	60	N/A	0.383
	Compressed aluminum foam	Air	44	N/A	0.418
Boomsma & Poulikakos [22]	Compressed aluminum foam	Water	88	N/A	0.069
	Compressed aluminum foam	Water	69	N/A	0.108
	Compressed aluminum foam	Water	61	N/A	0.136
Kececioglu & Jiang [9]	Packed Beds of 3mm and 6mm spheres	Water	40	N/A	0.348
Dukhan & Patel [24]	Aluminum foam	Air	92	20	0.951

Table 3.7 : (Continued) Correlation coefficient *b* for various studies.

Liu et al. [29]	Aluminum foam	Air	91	5	0.100
	Aluminum foam	Air	87	20	0.099
	Aluminum foam	Air	96	20	0.340
Dukhan & Patel [92]	Aluminum foam	Air	91	10	0.073
	Aluminum foam	Air	79	10	0.127
	Aluminum foam	Air	68	10	0.176
	Aluminum foam	Air	92	20	0.078
	Aluminum foam	Air	77	20	0.203
	Aluminum foam	Air	68	20	0.254
Dukhan [105]	Aluminum foam	Air	92	40	0.086

The data sets are plotted as friction factor f vs. Reynolds number based on permeability Re in Figure 3.16 on log–log axes. It should be noted that several of the data sets were not published in terms of these non-dimensional variables. Nonetheless, there was enough information to calculate f and Re. The majority of the data sets did not include data in the Darcy regime, and thus it was impossible to calculate the Darcy permeability. For purely illustration purposes, the Forchheimer permeability was used instead, in f and Re. The major trends and conclusions are not likely affected by this operation.

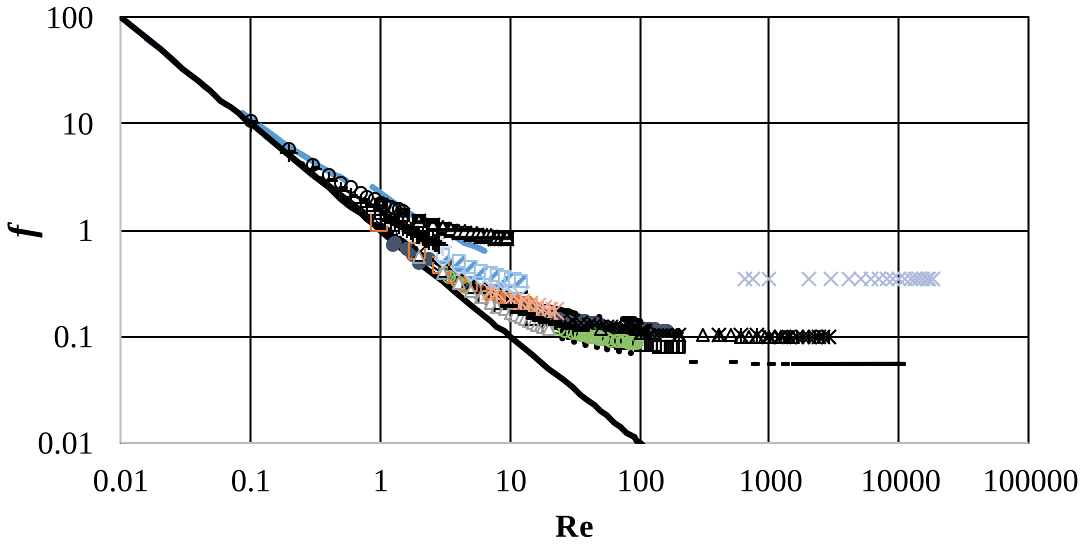

(a)

Figure 3.16 : Friction factors vs. Reynolds numbers plots from various studies: Data from Re of (a) The entire range, (b) 0.1 to 1 (c) 1 to 100, (d) 100 to 10000.

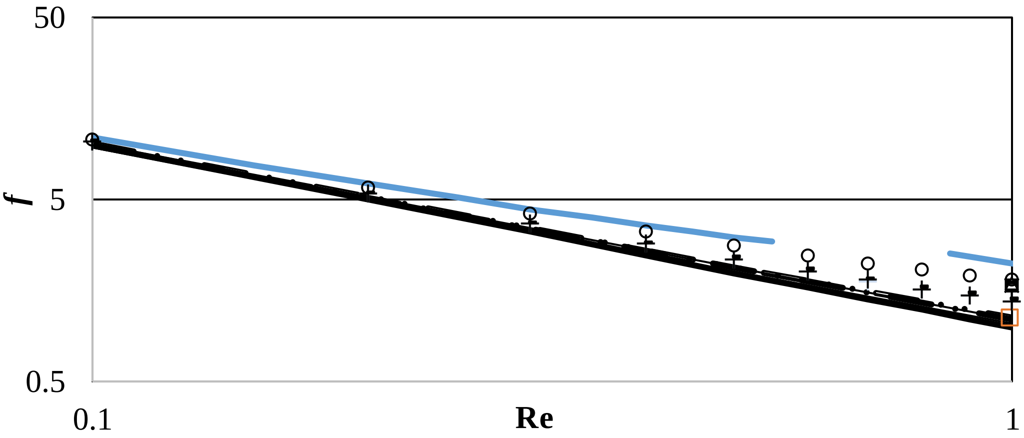

(b)

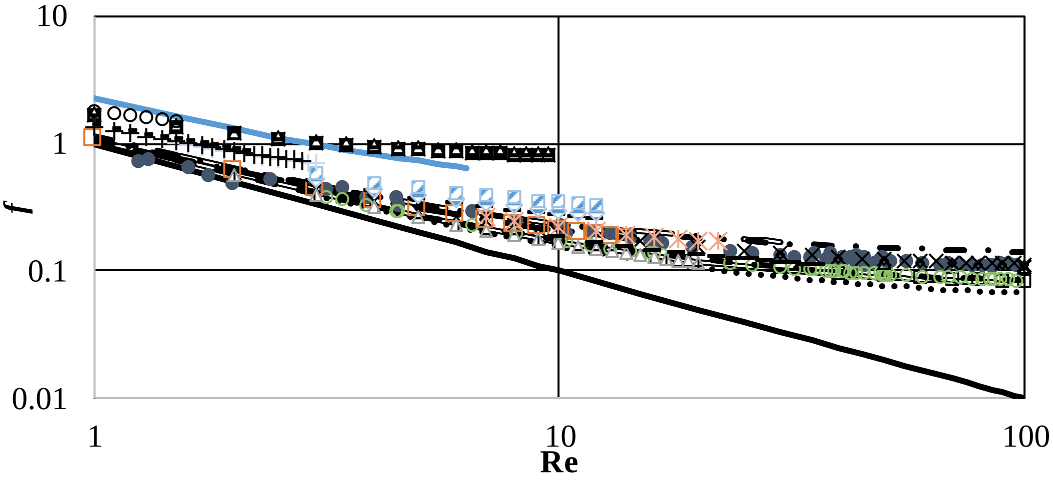

(c)

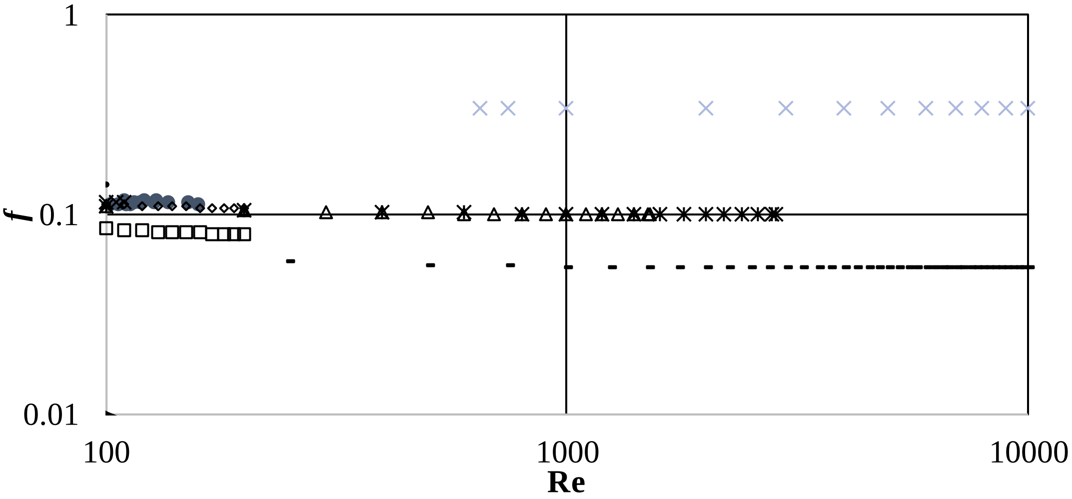

(d)

Figure 3.16 (continued) : Friction factors vs. Reynolds numbers plots from various studies: Data from Re of (a) The entire range, (b) 0.1 to 1 (c) 1 to 100, (d) 100 to 10000.

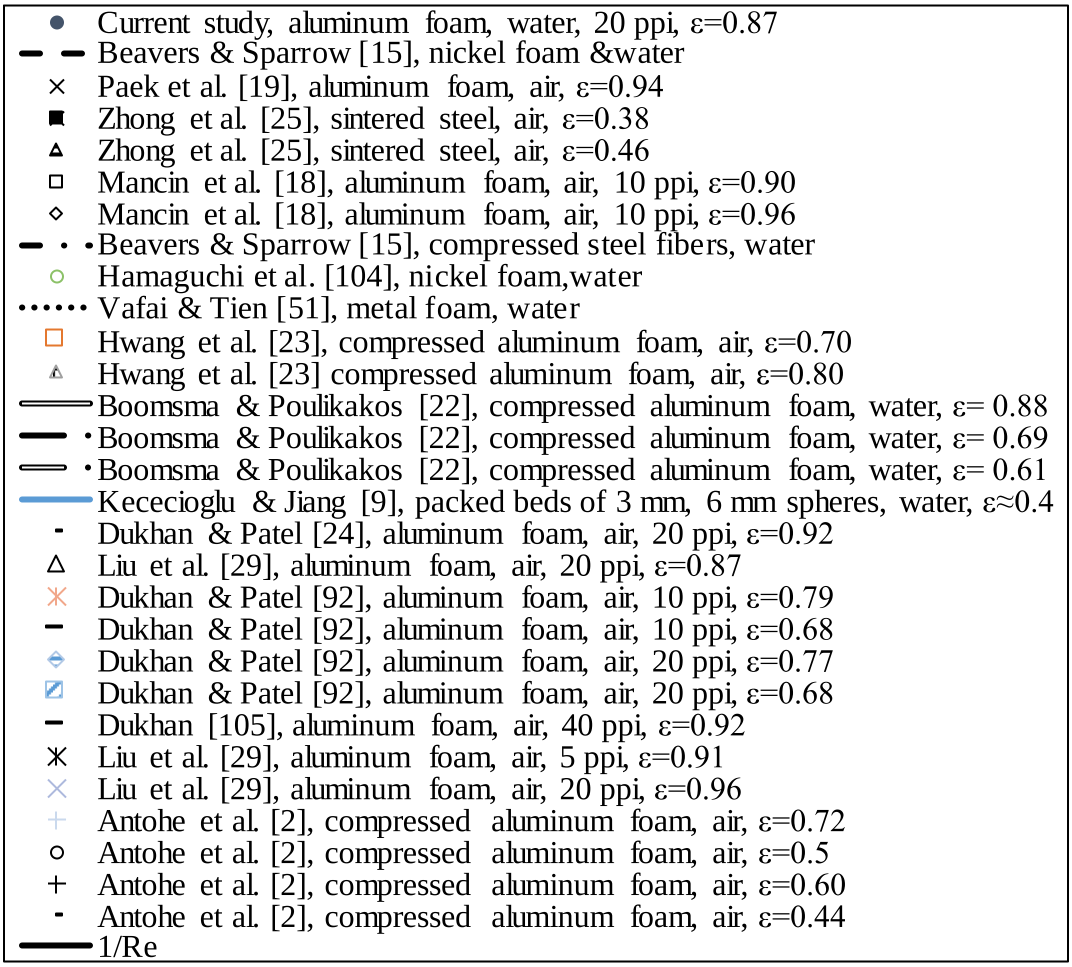

Figure 3.16 (continued) : Friction factors vs. Reynolds numbers plots from various studies: Data from Re of (a) The entire range, (b) 0.1 to 1 (c) 1 to 100, (d) 100 to 10000.

Several observations can be made:

1. The majority of the data for liquid flow lie in the Forchheimer regime and/or in the early turbulent flow regime ($1 < Re < 100$ approximately), probably due to experimental limitation of reaching higher flow rates representative of fully turbulent flow. The data for fully turbulent flow ($1 < Re < 100$ approximately) are mostly for air flow.

2. In the Darcy regime, the friction factor follows the line 1/Re for all available data: Boomsma and Poulikakos [22] in Figure 3.16 part (b) and the current study in part (c).

3. Transition from Darcy regime (departure from 1/Re) occurs at different Reynolds numbers for different porous media, indicating that this transition is affected by the

structure of the porous medium: Boomsma and Poulikakos [22] in Figure 3.16 part (b) and the current study in Figure 3.16 part (c).

4. Transition from Forchheimer to fully turbulent regime occurs in a narrow range of Reynolds number around 50, Figure 3.16 part (c); nonetheless there seems to be a dependence on the porous medium's structure.

5. For fully turbulent flow, the friction factor is independent of the Reynolds number (the pressure drop is proportional to the square of the velocity), and the viscous term a/Re can be neglected, as was predicted by (3.11).

6. The effect of porosity is shown by considering the data sets of Dukhan and Patel [92] for air flow in aluminum foam in the porosity ranged between 67% and 92%, approximately. For the same ppi, higher porosity corresponds to lower values of the friction factor.

3.3 Oscillating Flow

The schematic of the oscillating flow experimental setup is shown in Figure 3.17. The test section is the metal foam tested in the steady-state flow experiments.

The test section is connected to two 50.8-mm-diameter 190-mm-long Polyethylene tubes (2) at its two ends via flanges. Pressure taps are drilled on these tubes. The outlets of the polyethylene tubes are connected to stainless steel pipes 32 mm in diameter and 110 cm in length (3). The ends of these tubes are connected to an oscillating flow apparatus (5-9) via hoses (4). The main component of the oscillation generator is a double-acting cylinder which is connected to an electrically driven motoreductor by means of a flywheel and a crank arm. Inner diameter of hydraulic cylinder is 50 mm and the diameter of the rod bearing the piston installed inside it is 32 mm. The maximum stroke obtainable by this mechanism is 200 mm. Rotational speed of the 7.5-kW motoreductor is controlled via a variable speed AC-drive (6.99–20.97 rpm). Additionally, a groove, radially extending, mounted on the flywheel allows changes in stroke.

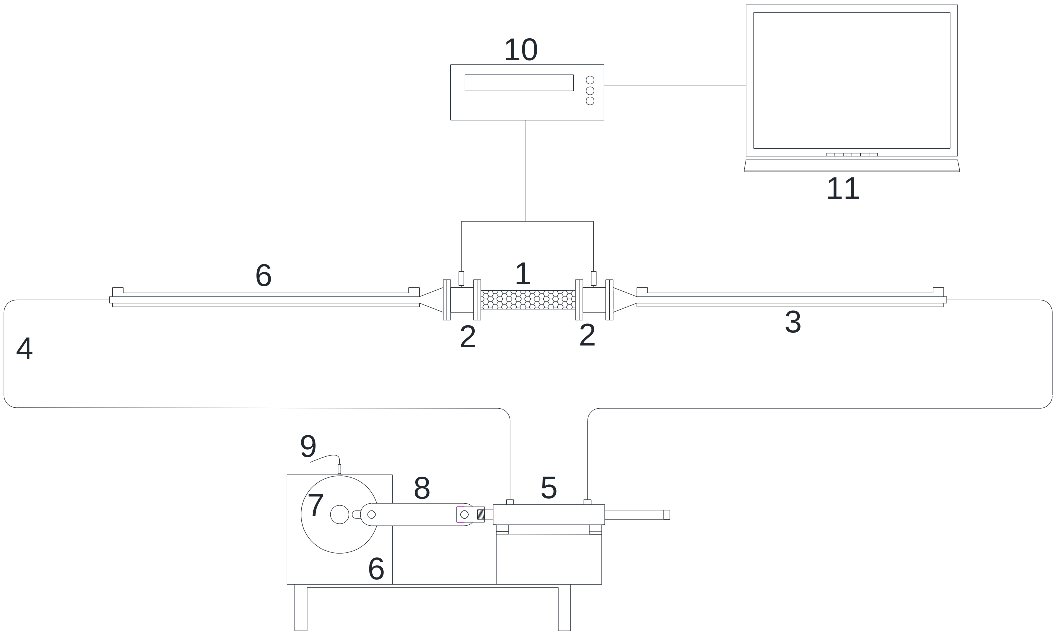

Figure 3.17 : Schematic of Experimental Setup: 1. Test Section (metal foam), 2. Polyethylene tubes, 3. Steel pipe of 32-mm in diameter, 4. Connecting hoses, 5. Oscillation Generator, 6. Motoreductor, 7. Flywheel, 8. Crank Arm, 9. Inductive Proximity Sensor, 10. Data logger, 12. Computer.

The pressure at the two ends of the test section is measured by Keller models PR-23R and PA-21Y piezoresistive transmitters, depending on the pressure level. The transmitters were calibrated by the manufacturer. PR-23R is able to measure gauge pressure up to 0.100 bars, while PA-21Y measures pressures up to 2.5 bars. The transmitters are connected to a data logger 10. They are set to provide 2–10 V as direct-current signals, which are converted to actual pressure values using a linear relation between voltage and pressure ranges. The sampling rate is set at 25 readings per second.

For oscillating flow tests, the system is filled with water while avoiding entraining air, the whole system is vacuumed down to 60 mmHg absolute. Heavily-filtered water is allowed to flow in from taps at the two ends of the piston (5). As air bubbles are impossible to avoid completely, care is taken as to remove air bubbles from the system through a purger, by tilting the whole set-up and/or by dis-mantling and reassembling parts of the set-up, as needed.

For a given oscillating flow run, the stroke length of the piston is set to a desired value, the oscillating generator is switched on, and the oscillating frequency is ramped to a targeted value. After the system stabilizes (up to 10 min), a Keithley 2700 XLINX data acquisition system, installed in the computer, communicates with the data logger and records two pressure signals from the two pressure transmitters and one signal from a clicker (9). This clicker touches a bump on a flywheel (part of the oscillation system) once per cycle, and it is used to calculate the angular speed. The above is repeated for stroke lengths (displacement of piston) 130 mm, 170 mm and 195 mm, and line frequencies of 5 Hz, 10 Hz, 15 Hz, 20 Hz, 25 Hz and 30 Hz. For the maximum stroke of 195 mm, data above 15 Hz cannot be acquired due to limitations on the experimental set-up.

Uncertainty in the reported data includes error in the directly-measured quantities, e.g., dimensions and frequency; and propagated error in derived quantities, e.g., angular frequency and maximum fluid displacement [94]. The uncertainties in length and diameter of the metal foam tube were 0.33% and 0.04%, respectively. As for pressure measurements, the transmitters had an error band of ±1% of full scale. These values were provided by the manufacturer and included effects of linearity, hysteresis and repeatability. The uncertainties in the angular frequency and maximum fluid displacement are estimated as 0.43% and 0.51%, respectively.

3.3.1 Data reduction

The mass flow rate of water for the steady-state test $\dot{m}$ is calculated as

$$\dot{m} = \frac{m}{t} \tag{3.12}$$

where m is the mass of water collected over a known period of time t.

The average velocity though the test section u is calculated as

$$u = \frac{\dot{m}}{\rho A} \tag{3.13}$$

where ρ is the density of water and A is the cross-sectional area of the test section.

For oscillating flow, maximum fluid displacements are related to the displacements of the piston: 130 mm, 170 mm and 195 mm according to conservation of mass, and the fact that water is an incompressible fluid. In this case, the maximum flow displacements ($x_{\max}$) at the entrance of the metal foam are calculated from the ratio of the cross-sectional areas of piston and entrance of porous channel as

$$x_{\max} = \frac{2RA_{\mathrm{p}}}{A} \tag{3.14}$$

where R, A_{p} and A are flywheel radius, cross-sectional areas of double acting cylinder and metal-foam pipe, respectively. This results in 74.35 mm, 97.23 mm and 111.53 mm for $x_{\max}$.

For each displacement, line frequency is changed from 5 Hz to 30 Hz by a servo drive of motor. Actual flow frequency, which is linearly proportional to line frequency, changes in the range of 0.116–0.696 Hz, depending on the 6.9–27.8 rpm speed of motoreductor. The motoreductor operates at 69.7 rpm at 50 Hz line frequency.

The displacement of the piston is taken as zero at the rear position inside the cylinder and as maximum, equal to the diameter of the flywheel, at the forward position. The piston displacement is actually equal to the fluid displacement since the fluid is incompressible. Hence, at the entrance of the foam, the fluid displacement x_{m} varies with angular frequency ω and time t according to

$$x_m(t) = \frac{x_{\max}}{2}\left(1 - \cos \omega t\right) \tag{3.15}$$

The cross-sectional mean fluid velocity in the channel is

$$u(t) = u_{\max} \sin \omega t \tag{3.16}$$

where $u_{\max} = \omega x_{\max} / 2$.

3.3.2 Results of oscillating flow experiments

The pressure at the inlet of the metal foam for the short displacement of 74.35 mm is plotted as a function of time in Figure 3.18, the medium displacement of 97.23 in Figure 3.19 and the long displacement in Figure 3.20. Part (a) of each figure is for all frequencies, while part (b) is for the low frequencies. The periodic behavior is obvious. The high frequency causes the pressure to dip below zero. This is likely due to interactions of inertia and acceleration effects combined with sudden flow reversal. These effects are mild in the low-frequency range. Pressure in this range is always positive. In the high-frequency range, the amplitude of the pressure is strongly affected by the frequency. For example, it jumps from about 30 kPa to about 70 kPa when the frequency increases from 0.464 Hz to 0.580 Hz.

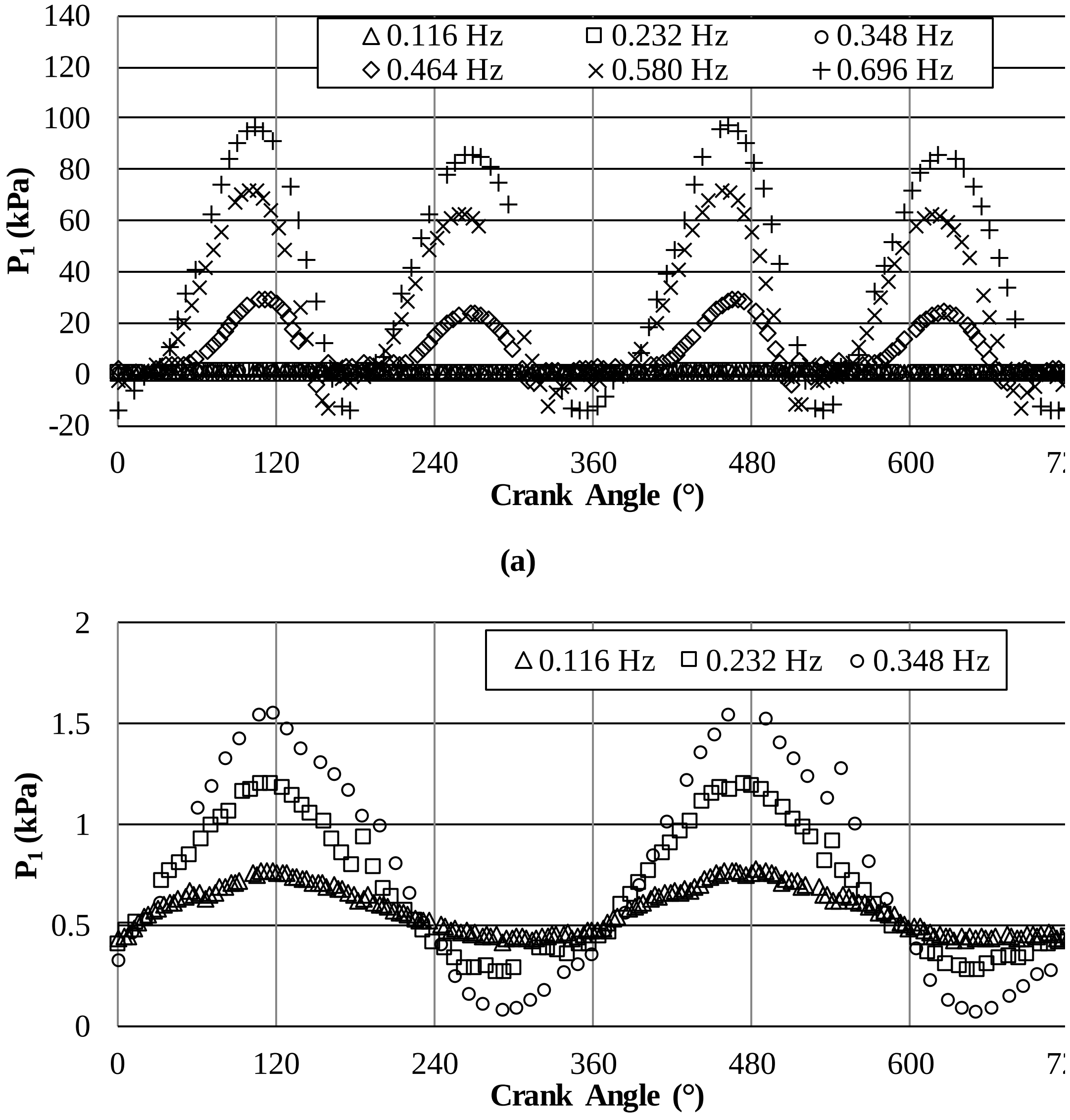

(a)

(b)

Figure 3.18 : Pressure at inlet of foam as a function of crank angle for the short fluid displacement $x_{\max}$= 74.35 mm: (a) for all frequencies and (b) for low frequencies.

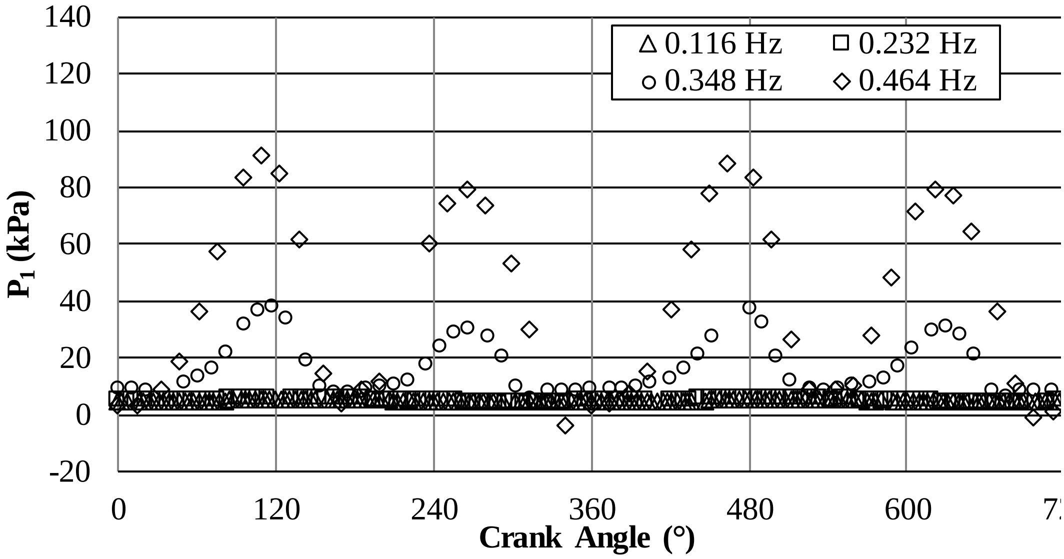

(a)

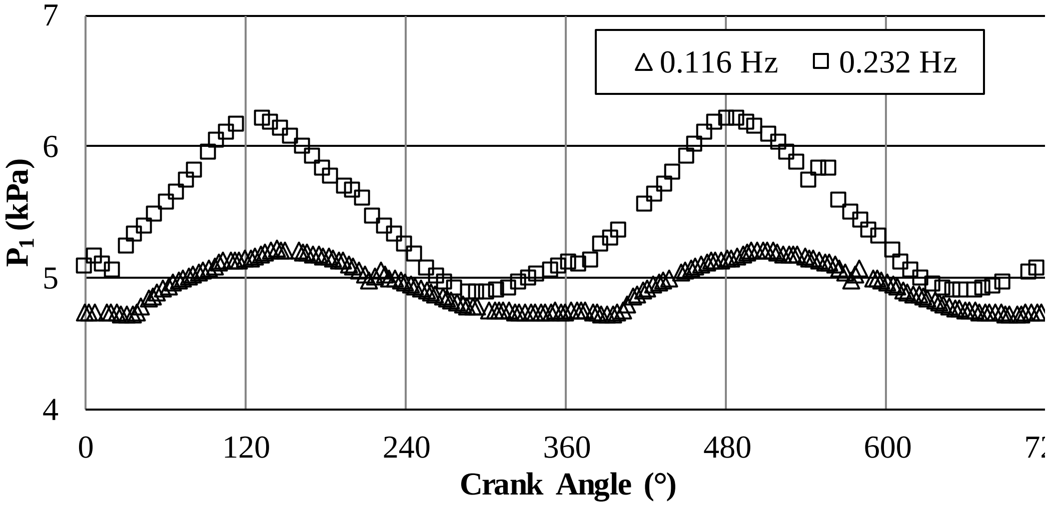

(b)

Figure 3.19 : Pressure at inlet of foam as a function of crank angle for the medium fluid displacement $x_{\max}$= 97.23 mm: (a) for all frequencies and (b) for low frequencies.

Figure 3.21 is a plot of pressure amplitude as a function of frequency for the three flow displacements. For low frequencies, the effect of frequency on pressure amplitude is very mild, especially for short and medium fluid displacements. At high frequencies (above or equal to 0.348 Hz), the frequency has a pronounced influence on the amplitude of the pressure. Also, the fluid displacement is seen to generally have a strong influence on the amplitude of the pressure, with this influence being more pronounced for frequencies higher that 0.348 Hz.

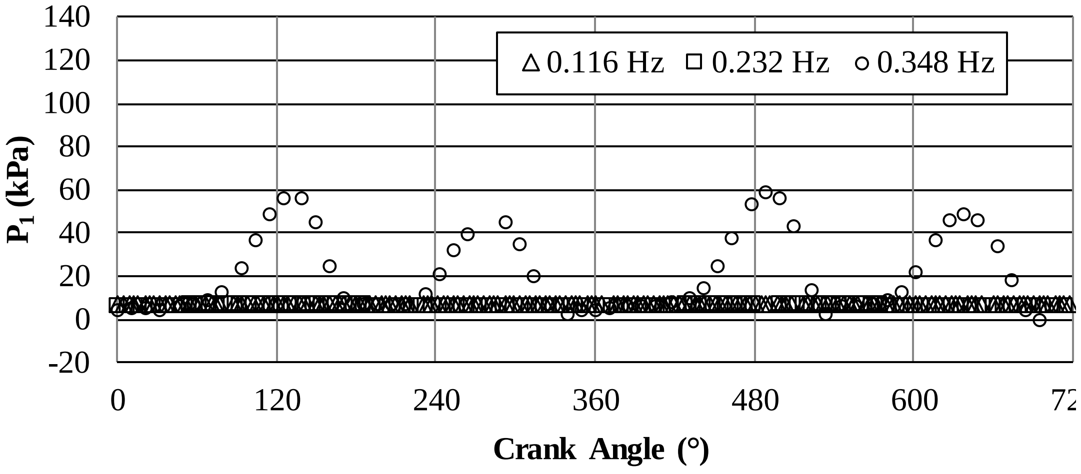

(a)

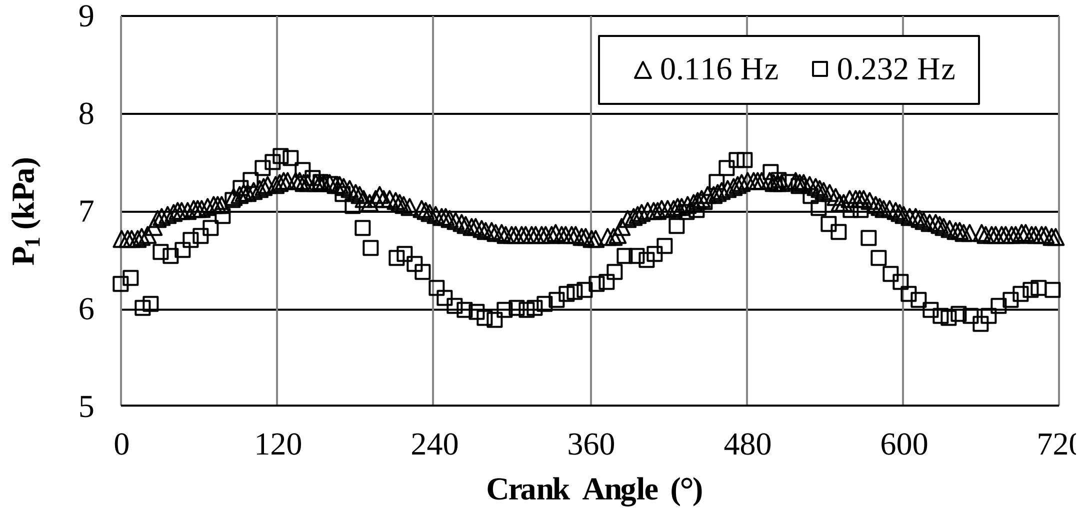

(b)

Figure 3.20 : Pressure at inlet of foam as a function of crank angle for the long fluid displacement $x_{\max}$= 111.53 mm: (a) for all frequencies and (b) for low frequencies.

In Figure 3.22 part (a), the average velocity through the foam is super-imposed on the pressures at the inlet and outlet for the case of $x_{\max}$= 97.23 mm and ω= 0.348 Hz. It is clear that there is a phase shift between these pressures and flow velocity of approximately 25°. In part (b) of Figure 3.22 for the low frequency of 0.232 Hz, the two pressures are not in phase. The phase shift between the inlet pressure and flow velocity is approximately 36°, and between the outlet pressure and flow velocity the shift is about 212°. Pamuk and Özdemir [76] reported no phase shift between the pressures and flow velocity for oscillating water flow in packed spheres. Khodadadi [72] reported a phase shift of 90° between the velocity and pressure gradient based on his analytical solution. Zhao and Cheng [73] also reported a phase shift between pressure drop and velocity for air flow in screens; this phase shift increased with frequency. The channeling effect (flow velocity exhibiting maxima next to the solid wall) reported by Khodadadi [72] could be responsible in part for this phase shift.

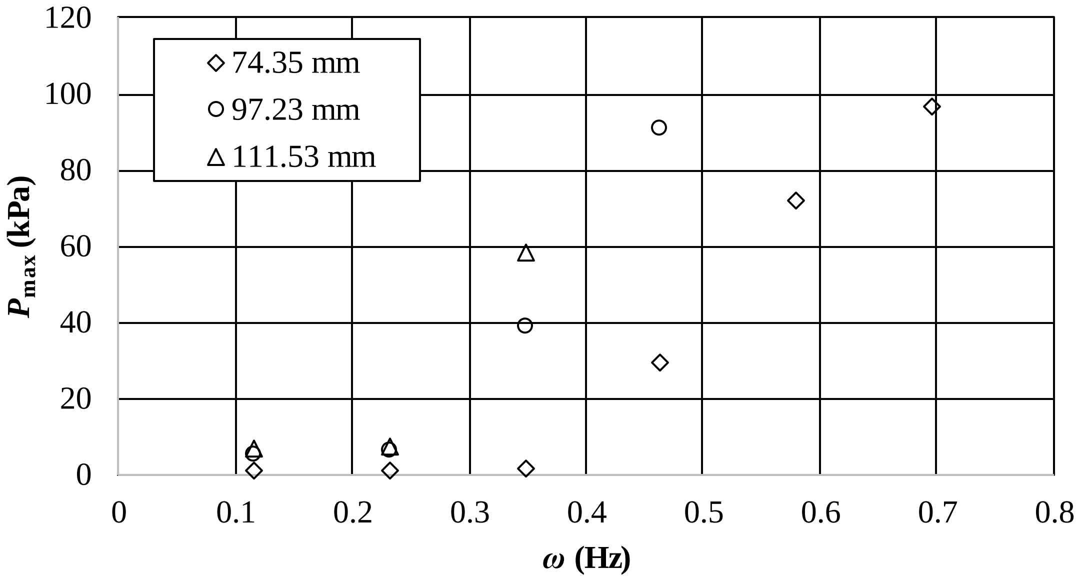

Figure 3.21 : Inlet pressure amplitude as a function of frequency for the three fluid displacements.

In Figure 3.22, the dotted lines represent the flow velocity at which the Forchheimer regime starts. What this means is that flow changes regimes between Darcy and Forchheimer more than once within a given period. Regime changes indicate frictional resistance changes; this phenomenon adds to the complexity of the phenomenon at hand.

To display the effect of frequency on inlet and outlet pressures, these pressures as a function of time, for the short stroke (x_{max} = 74.35 mm), are shown in Figure 3.23. Parts (a) through (f) are for frequencies 0.116 Hz, 0.232 Hz, 0.348 Hz, 0.464 Hz, 0.580 Hz and 0.696 Hz. Parts (a) through (d) of Figure 3.24 are for the medium stroke (x_{max} = 97.23 mm), and they are for frequencies 0.116 Hz, 0.232 Hz, 0.348 Hz and 0.464 Hz. Figure 3.25 includes the similar distributions for the first three consecutive frequencies. From these plots it is clear that the frequency has some effect on these pressures. For low frequency, there is a phase shift between the inlet and outlet pressures. This phase shift decreases as the frequency increases; and disappears for the two high frequencies of 0.348 Hz and 0.464 Hz (parts c and d) for the medium stroke. This trend is the exact opposite of what was reported by Cha et al. [75] for oscillating flow of helium through typical porous fillers of regenerators used in pulse-tube and Stirling-cycle cryocoolers (e.g. mesh screens, foam metal, stacked micro-porous nickel disks). This is most likely due to the difference in working fluid (water versus helium), difference in porosities of porous media (here 87.6% and there around 60%), and most importantly the frequency range which is extremely low for the current study compared to Cha et al. [75]. It must be mentioned here that compressibility effects had a significant effect in the case of helium.

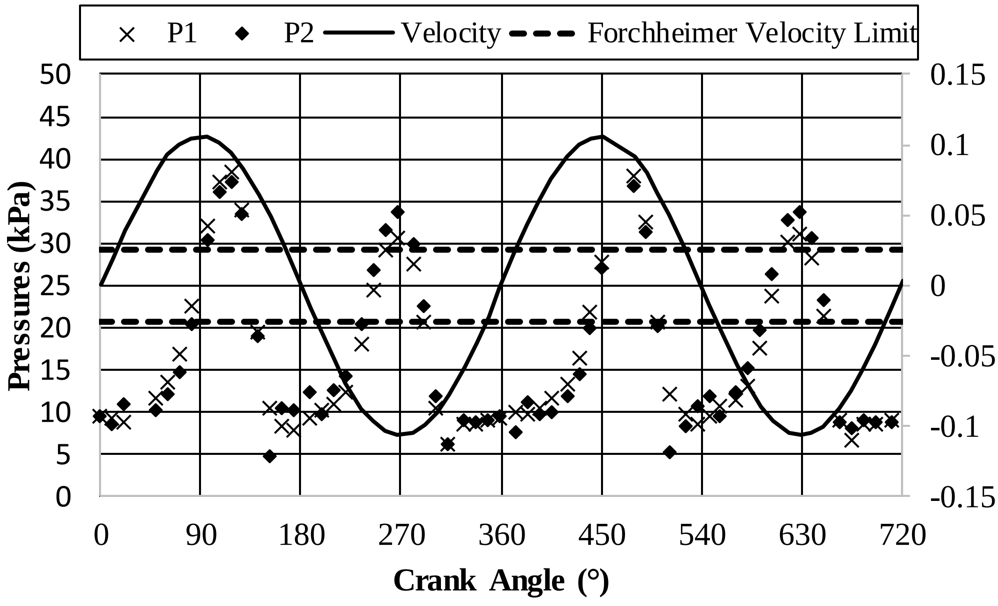

(a)

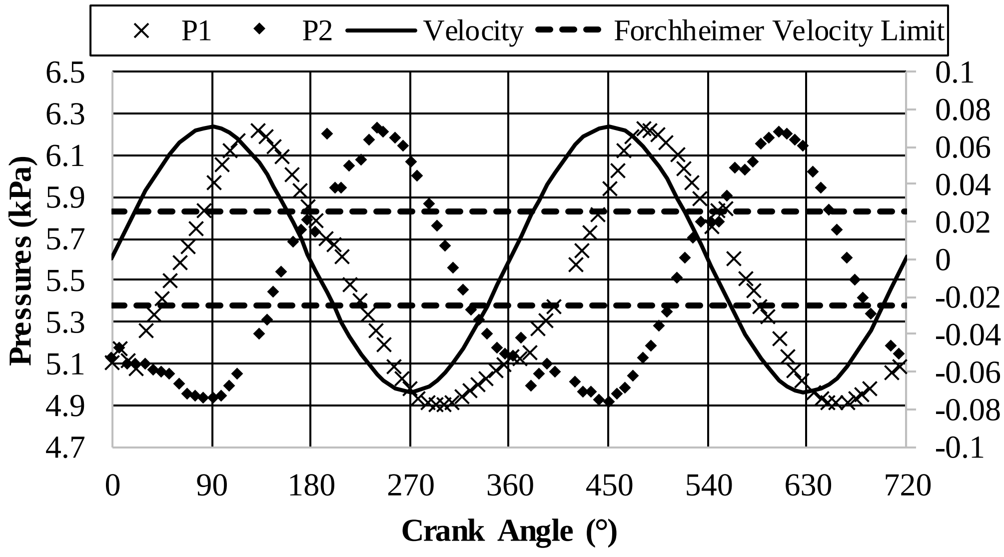

(b)

Figure 3.22 : Transient pressures at inlet and outlet and average flow velocity for $x_{\max}$= 97.23 mm: (a) ω= 0.348 Hz and (b) ω= 0.232 Hz.

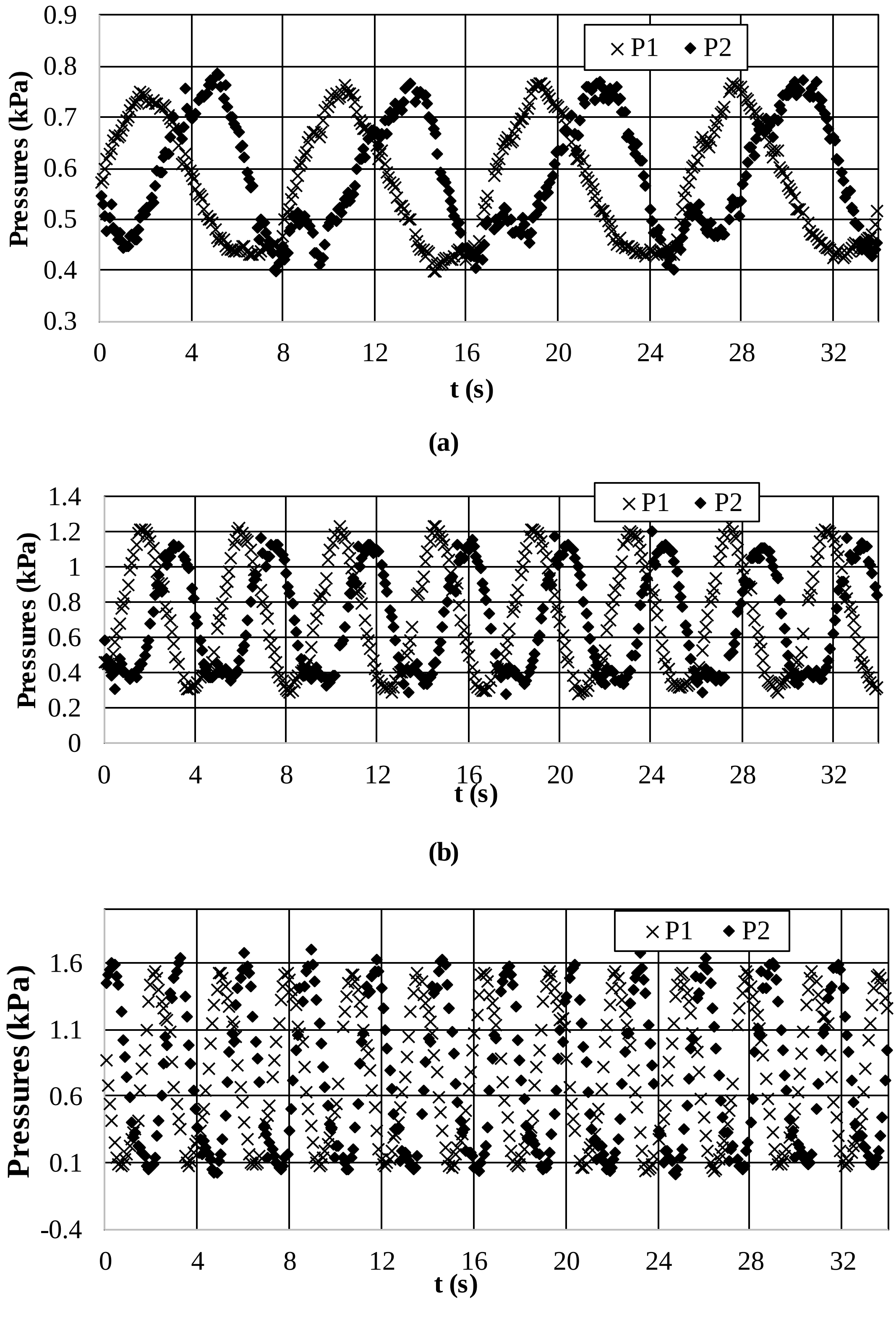

Figure 3.23 : Transient pressures at inlet and outlet for $x_{\max}$ = 74.35 mm and (a) ω = 0.116 Hz, (b) ω = 0.232 Hz, (c) ω = 0.348 Hz, (d) ω = 0.464 Hz, (e) ω = 0.580 Hz and (f) ω = 0.696 Hz.

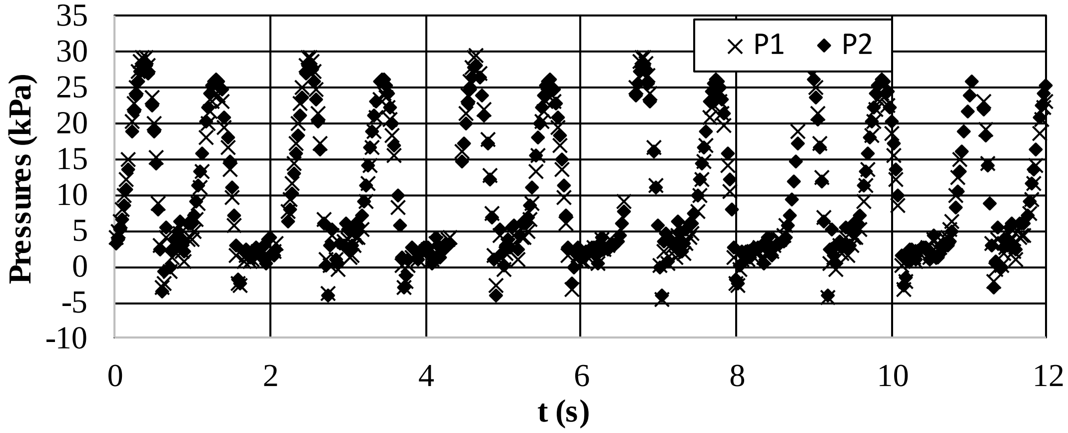

(d)

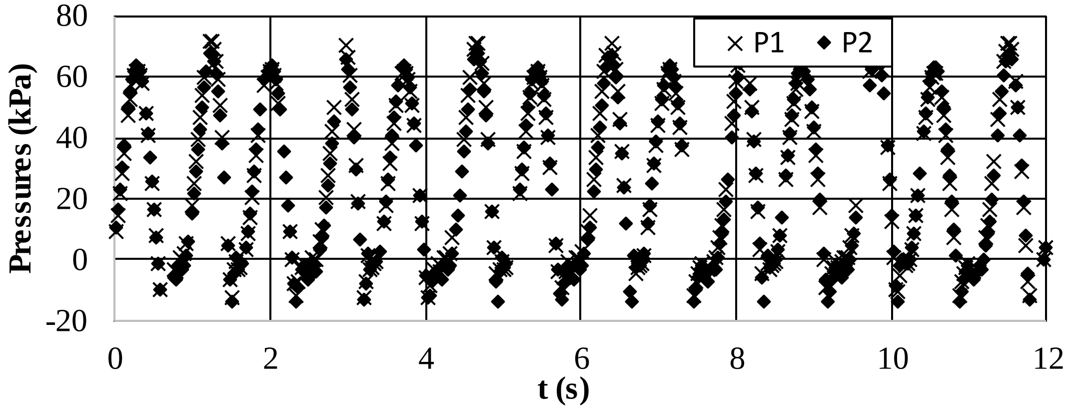

(e)

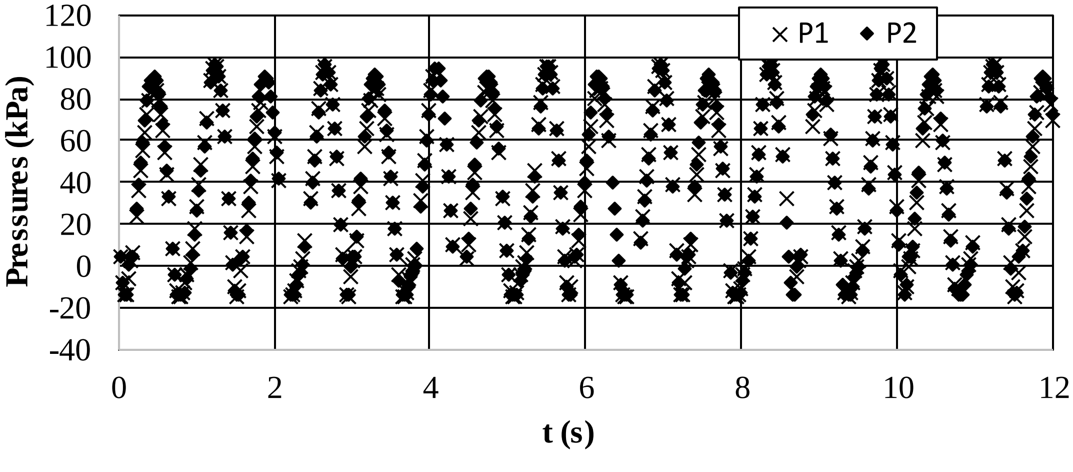

(f)

Figure 3.23 (continued): Transient pressures at inlet and outlet for $x_{\max} = 74.35$ mm and (a) $\omega = 0.116$ Hz, (b) $\omega = 0.232$ Hz, (c) $\omega = 0.348$ Hz, (d) $\omega = 0.464$ Hz, (e) $\omega = 0.580$ Hz and (f) $\omega = 0.696$ Hz.

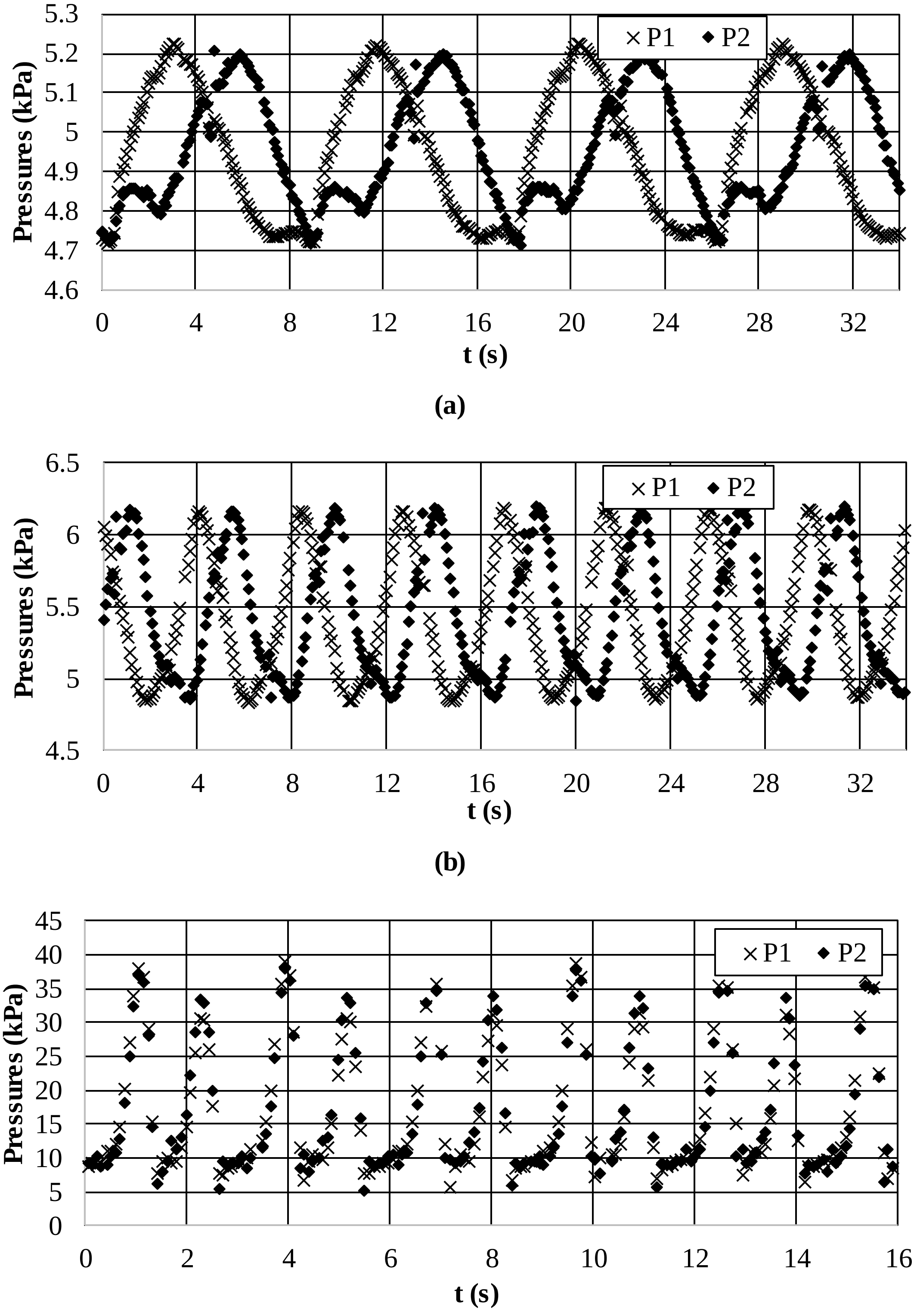

Figure 3.24 : Transient pressures at inlet and outlet for $x_{\max}$ = 97.23 mm and (a) ω = 0.116 Hz, (b) ω = 0.232 Hz, (c) ω = 0.348 Hz, (d) ω = 0.464 Hz.

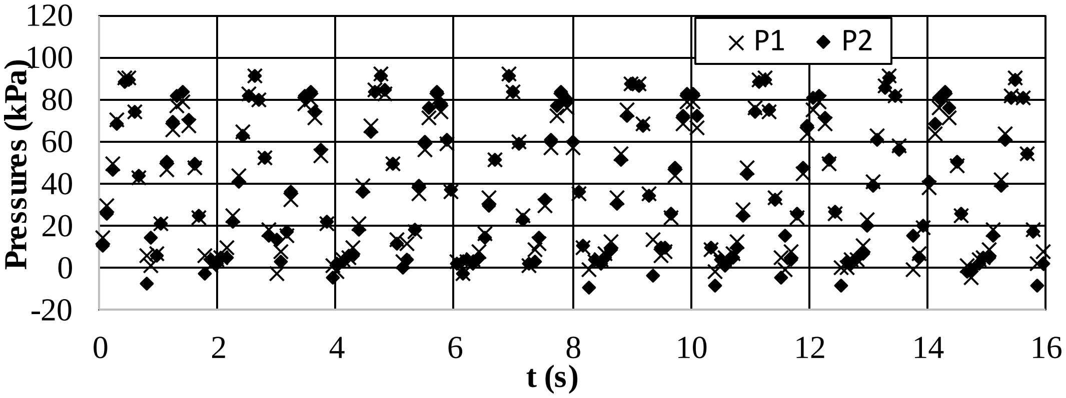

(d)

Figure 3.24 (continued) : Transient pressures at inlet and outlet for $x_{\max}$ = 97.23 mm and (a) ω = 0.116 Hz, (b) ω = 0.232 Hz, (c) ω = 0.348 Hz, (d) ω = 0.464 Hz.

Another important effect of the frequency is that there is a clear difference in the amplitudes of inlet and outlet pressures for the high frequencies of 0.348 Hz and 0.464 Hz (parts c and d), again for the medium-stroke example. For these frequencies, there is a repeating pattern with a period of about 3 s. These trends were also true for the other two maximum displacements, which suggests the existence of two regimes based on frequency. No similar observations were made by Pamuk and Özdemir [76] for oscillating water flow in packed spheres.

FFT analysis was performed on all pressure signals. It was found that there was a clear change in behavior depending on the frequency driving the flow. The pressures had up to six significant frequencies (harmonics). Hsu et al. [74] stated that, for oscillating flow through packed wire screens, the presence of harmonics was a sign of nonlinear processes, and nonlinear correlation between the pressure drop and flow velocity. This was especially true for large flow displacements.

The dominant frequency among the harmonics of the pressure drop of the current study matched the flow frequency, only for low frequencies: 0.116, 0.232, 0.348 Hz for the short displacement $x_{\max}$= 74.35 mm; 0.116 and 0.232 Hz for the medium and long dis-placements $x_{\max}$ = 97.23 and 111.53 mm. For higher flow frequencies, the flow frequency was not the dominant harmonic of the pressures. Actually, the flow frequency ranked number three in terms of dominance in the harmonics of the pressures. These results confirm the regime change based on flow frequency noted above.

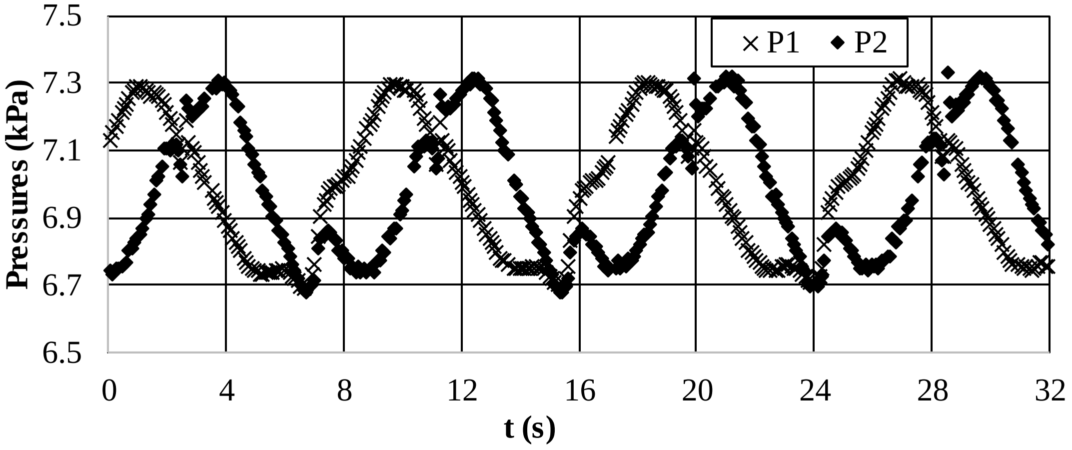

(a)

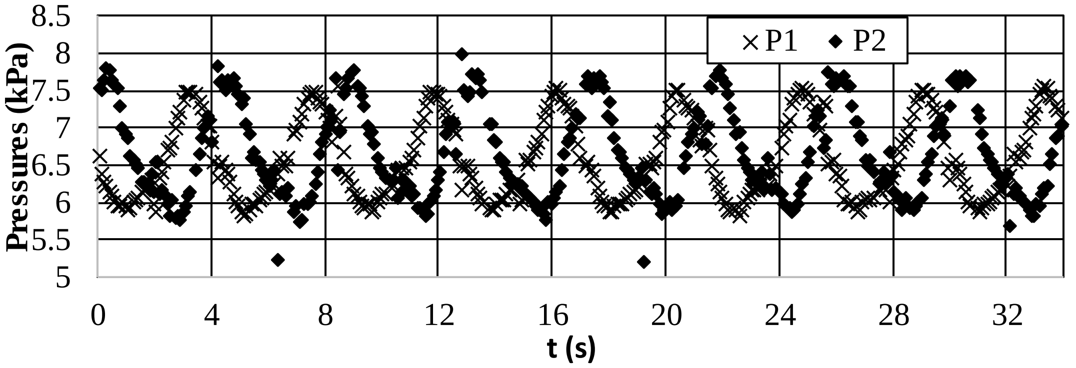

(b)

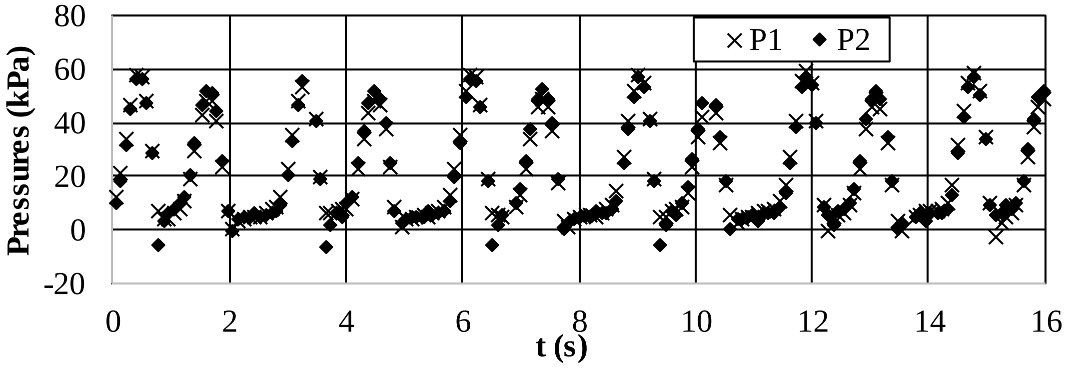

(c)

Figure 3.25 : Transient pressures at inlet and outlet for $x_{\max}$ = 111.53 mm and (a) ω = 0.116 Hz, (b) ω = 0.232 Hz, (c) ω = 0.348 Hz.

The effect of maximum fluid displacement on the pressure at the inlet of the foam is shown in Figure 3.26 for various frequencies. As expected, there is a positive correlation between the displacement and the inlet pressure. As the frequency increases, the pressure exhibits high magnitudes that look like spikes due to acceleration. The pressure exhibits a periodic behavior with the period being longer for shorter displacements.

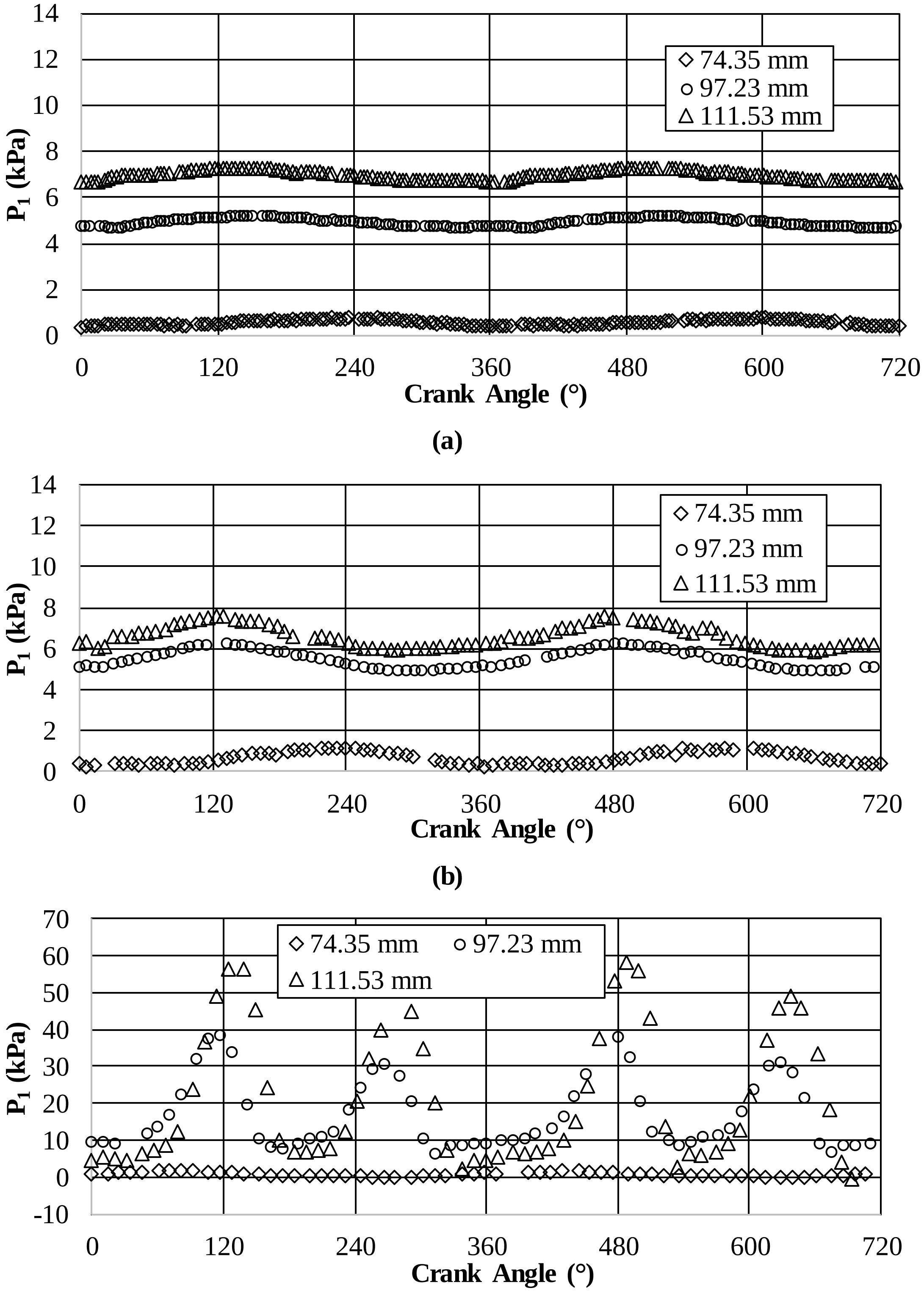

(a)

(b)

(c)

Figure 3.26 : Transient pressure at inlet vs. crank angle – effect of displacement for (a) ω= 0.116 Hz, (b) ω = 0.232 Hz, (c) ω = 0.348 Hz, and (d) ω = 0.464 Hz.

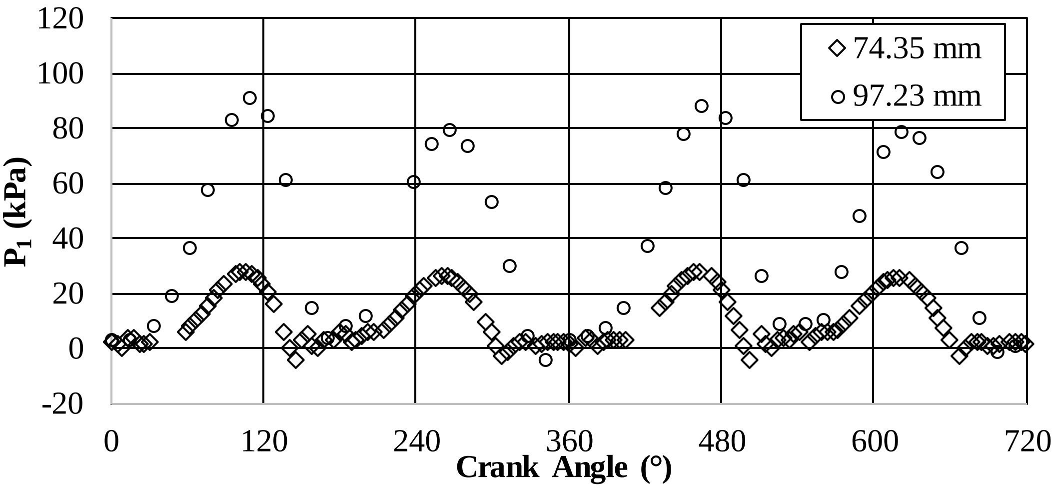

(d)

Figure 3.26 (continued) : Transient pressure at inlet vs. crank angle – effect of displacement for (a) *ω*= 0.116 Hz, (b) *ω* = 0.232 Hz, (c) *ω* = 0.348 Hz, and (d) *ω* = 0.464 Hz.

The effect of frequency on the pressure drop across the foam is shown in Figure 3.27. Part (a) is for high frequencies, while part (b) is for the low frequencies. For high frequency, the pressure drop has different amplitudes above and below the zero line. This is due to acceleration and interactions between forward and reversed flow in the porous medium. For the low frequencies, the pressure drop is sinusoidal with equal amplitudes above and below the zero line. This is due to the fact that for low frequencies, the fluid has abundant time to react to changes in flow direction, i.e., inertial effects are minimal. The maximum pressure drop increases with frequency. This is similar to what was reported by Leong and Jin [78,79,85] for air flow in metal foam, and by Zhao and Cheng [73] for air flow in a packed bed of woven screens.

The effect of maximum fluid displacement on pressure drop across the foam is shown in Figure 3.28 for various frequencies. For the low frequencies of 0.116 Hz and 0.232 Hz, the pressure drop is periodic and has equal amplitudes above and below the zero line, part (a) and (b). As the frequency increases to 0.348 Hz and 0.580, parts (c) and (d), and for the maximum displacement, there seems to be a phase shift of about 180° between the pressure drop for the short displacement of 74.35 mm on one hand and the displacements 97.23 mm and 111.53 mm on the other hand, part (c). The behavior of the pressure drop for the low frequencies of 0.116 Hz and 0.232 Hz is consistent with what was obtained by Pamuk and Özdemir [76] for water flow in packed spheres, Leong and Jin [78,79] for air flow in metal foam and by Zhao and Cheng [73] for air flow in a packed bed of woven screens. However, the trends obtained for the high frequency case of 0.348 Hz is not consistent with these previous studies. This is most likely due to difference in porous media and porosities between the current study and Pamuk and Özdemir [76] and due to the different working fluids of the current study and Leong and Jin [78].

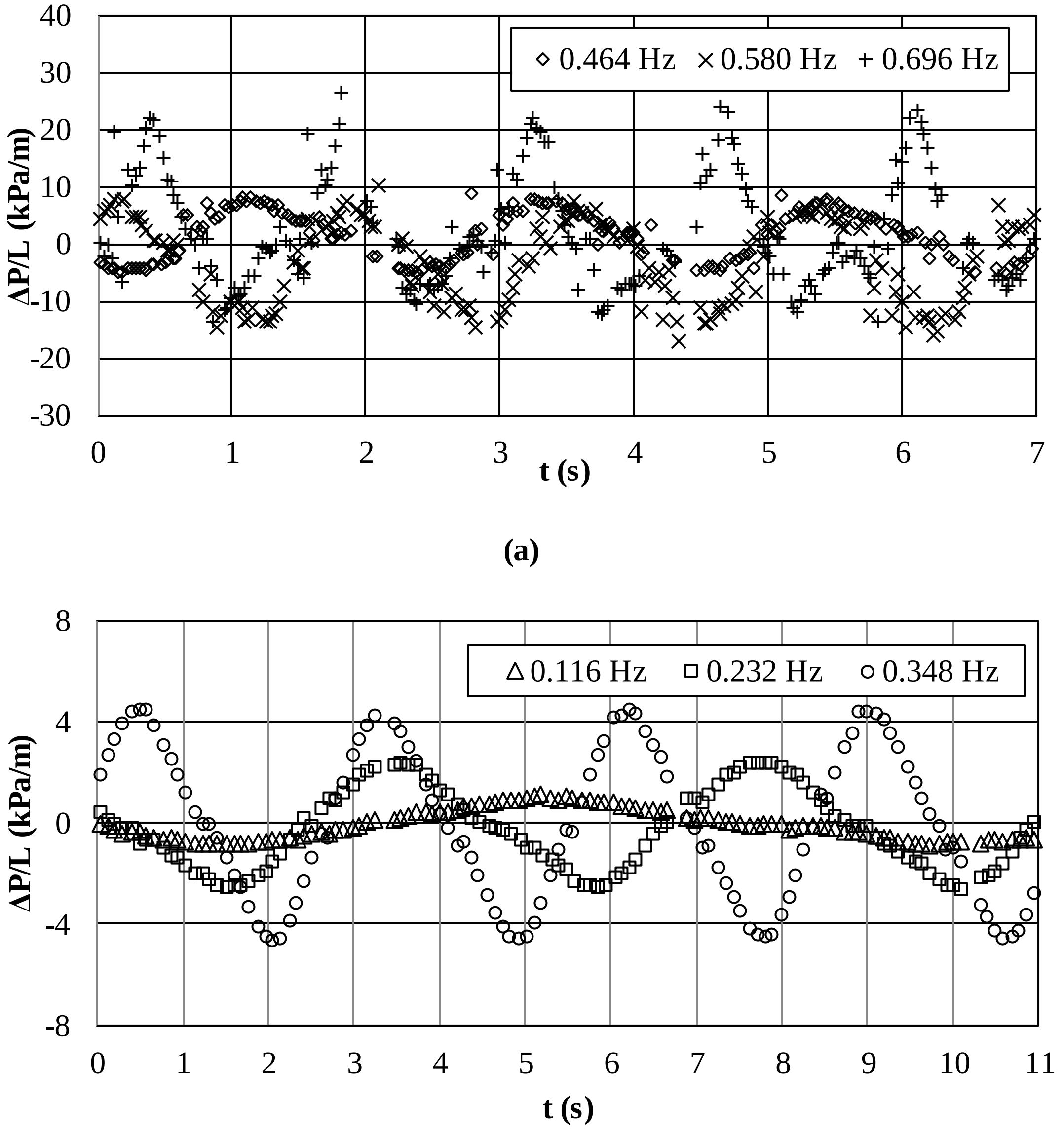

(a)

(b)

Figure 3.27 : Pressure gradient versus time – effect of frequency at a displacement of 74.35 mm: (a) high frequencies and (b) low frequencies.

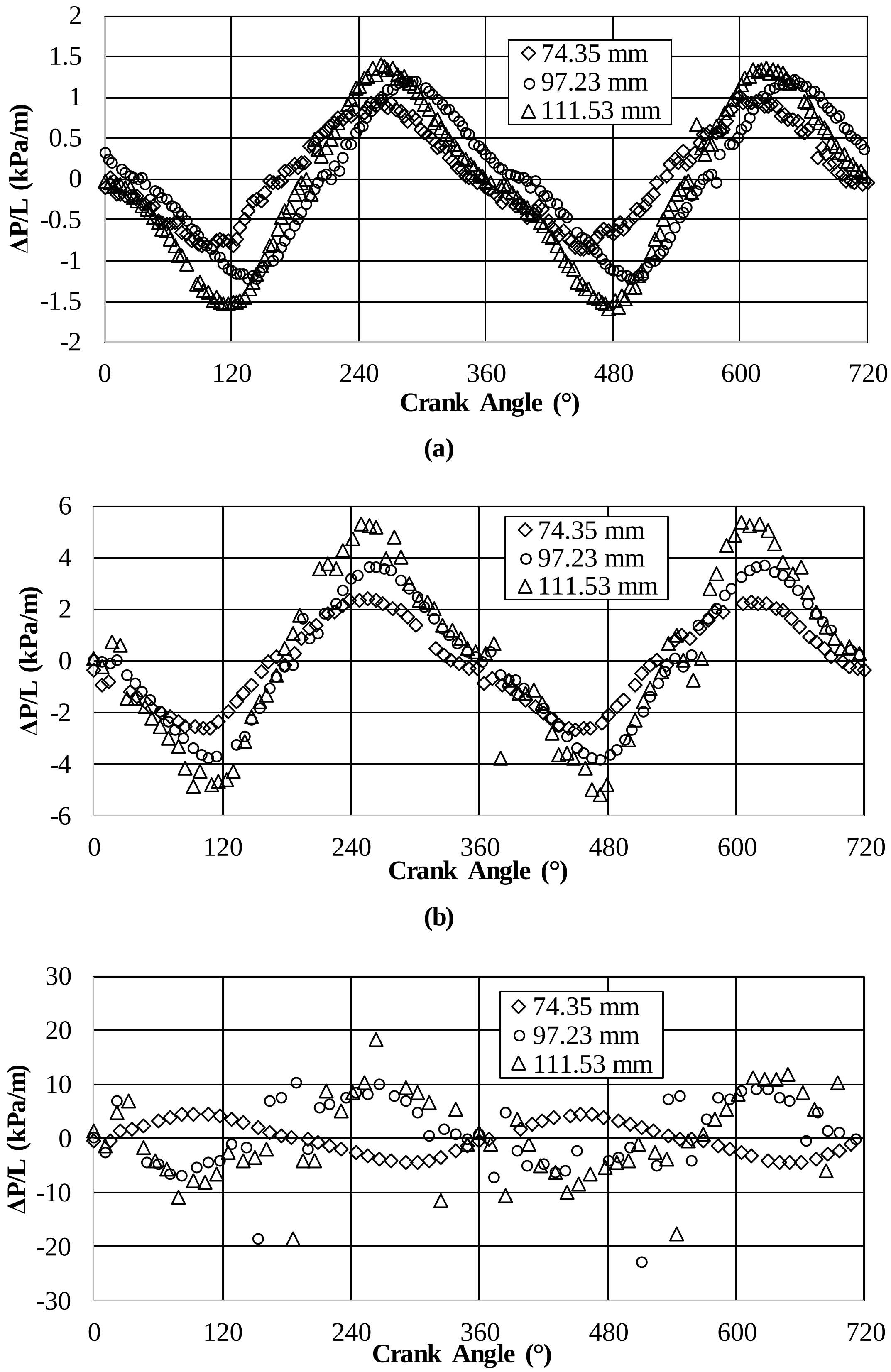

(a)

(b)

(c)

Figure 3.28 : Pressure gradient as a function of crank angle – effect of displacement: (a) *ω* = 0.116 Hz, (b) *ω* = 0.232 Hz, (c) *ω* = 0.348 Hz and (d) *ω* =0.580 Hz.

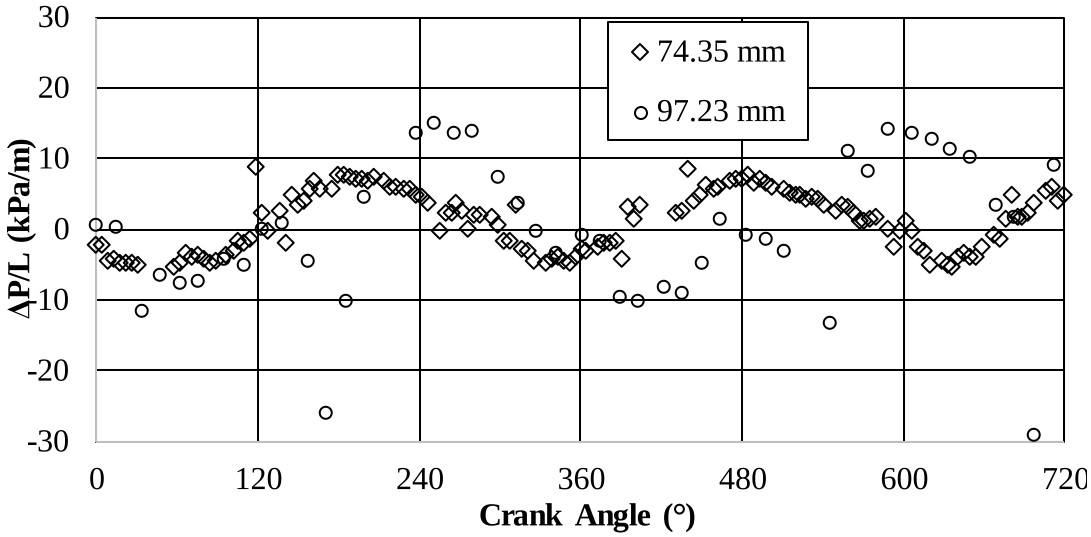

(d)

Figure 3.28 (continued) : Pressure gradient as a function of crank angle – effect of displacement: (a) ω = 0.116 Hz, (b) ω = 0.232 Hz, (c) ω = 0.348 Hz and (d) ω =0.580 Hz.

For steady-state unidirectional flow in packed beds, Dybbs and Edwards [7] experimentally confirmed that the friction factor behaved according to

$$f_D = a\left(\frac{1}{\mathrm{Re}_D}\right) + b \qquad \textbf{(3.17)}$$

where $f_D = 2\left(\Delta p / L\right) D / \rho u^2$, $\mathrm{Re}_D = \rho \mathrm{uD}/\mu$ and a and b are adjustable parameters. Here D is the tube diameter. A similar equation was derived by Kececioglu and Jiang [9].

In oscillating-flow literature, the friction factor is based on the amplitude of mean velocity, or the maximum velocity, $u_{\max}$, and maximum pressure gradient, $\Delta p_{\max}$ according to

$$f_{\max} = \frac{2\left(\Delta p_{\max} / L\right)}{\rho u_{\max}^2} \qquad \textbf{(3.18)}$$

The kinetic Reynolds number is defined as

$$\mathrm{Re}_\omega = \frac{\rho \omega D^2}{\mu} \tag{3.19}$$

where ω is the angular frequency. The Reynolds number based on maximum displacement is defined as

$$\mathrm{Re}_{\max} = \frac{\rho \omega D x_{\max}}{2\mu} \tag{3.20}$$

So these two Reynolds numbers are related according to $\mathrm{Re}_{\max} = \left(x_{\max}\,\mathrm{Re}_\omega\right)/2D$.

Table 3.8 : Correlation coefficients for steady-state and oscillating flow.

	$a,\ \tilde{a}$	$b,\ \tilde{b}$
Steady state flow	88428	39
Oscillating flow	145144	33

Figure 3.29 compares the friction factor for steady and oscillating flows. The behavior of the steady-state friction factor is consistent with the typical behavior for porous media. Equation (3.6) is seen to correlate the steady-state friction data very well with the values of a and b given in Table 3.8.

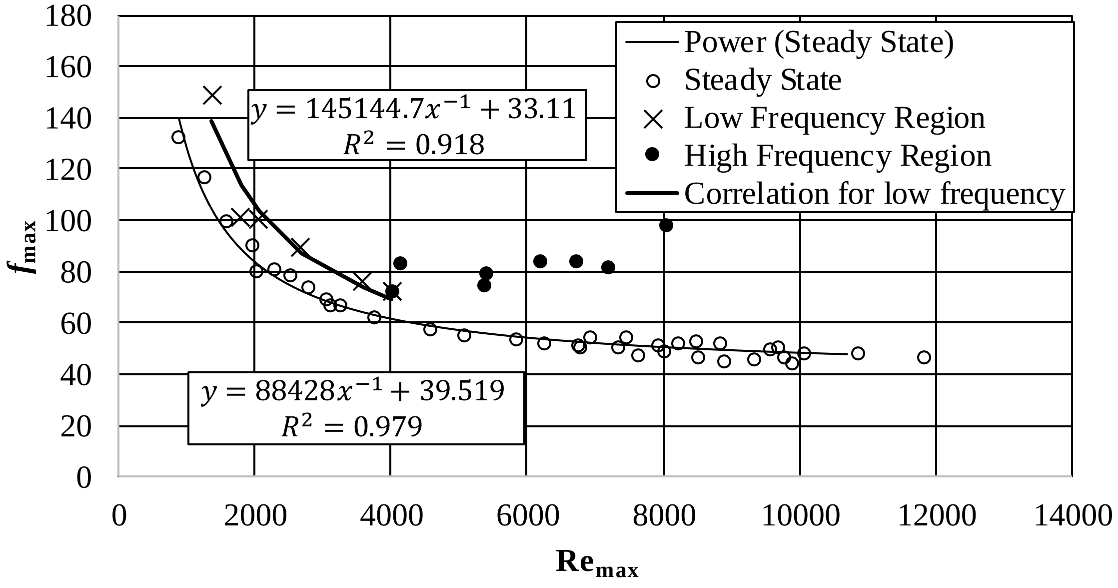

Figure 3.29 : Friction factor versus Reynolds number for steady and oscillating flow for all flow displacements.

The friction factor for the oscillating flow lies above that for steady flow, as expected, and as was obtained for the case of air flow in packed woven screens by Zhao and Cheng [73], for water flow in packed spheres by Pamuk and Özdemir [76] and for air flow in metal foam by Leong and Jin [78]. Compared to the spheres of Pamuk and Özdemir [76] , the difference between steady and oscillating friction factors is more pronounced in the case of metal foam.

The behavior of oscillating-flow friction factor suggests a regime change based on frequency starting at about $\mathrm{Re}_{\max}$= 4000. For the lower range lying before 4000, the friction factor correlates with $\mathrm{Re}_{\max}$ according to

$$f_{\max} = \tilde{a}\left(\frac{1}{\mathrm{Re}_{\max}}\right) + \tilde{b} \tag{3.21}$$

with the correlation coefficients $\tilde{a}$ and $\tilde{b}$ given in Table 3.8. For higher values of $\mathrm{Re}_{\max}$, the above correlation is not valid, and the friction factor is seen to generally increase with $\mathrm{Re}_{\max}$.

A similar correlation to Equation (3.21) was obtained by Zhao and Cheng [73] for air flow in packed woven screens, by Pamuk and Özdemir [76] for water flow in packed spheres and by Leong and Jin [78,79] for air flow in metal foam. However, in Pamuk and Özdemir [76] the friction factor continues to gradually decrease with $\mathrm{Re}_{\max}$ for $\mathrm{Re}_{\max}$ beyond 4000. As such it may be stated that there was no regime change for the case of water flow in packed spheres.

3.3.3 Comparison to other studies

Figure 3.30 compares the results of the current study with others in the literature using the friction factor as a function of Reynolds number. The effect of working fluid is ascertained by contrasting the current results with those of Leong and Jin [78] who tested oscillating air flow in similar aluminum foam having the same pore density and comparable porosity. The friction factor and Reynolds number data of Leong and Jin [78] were extracted from a correlation provided by these authors; and their data was put into the notation of the current paper so that the comparison is meaningful. It is seen that these researchers tested in a different range of Reynolds number. However, it may be safely stated that the friction factor for the case of water is about ten times higher than that for air.

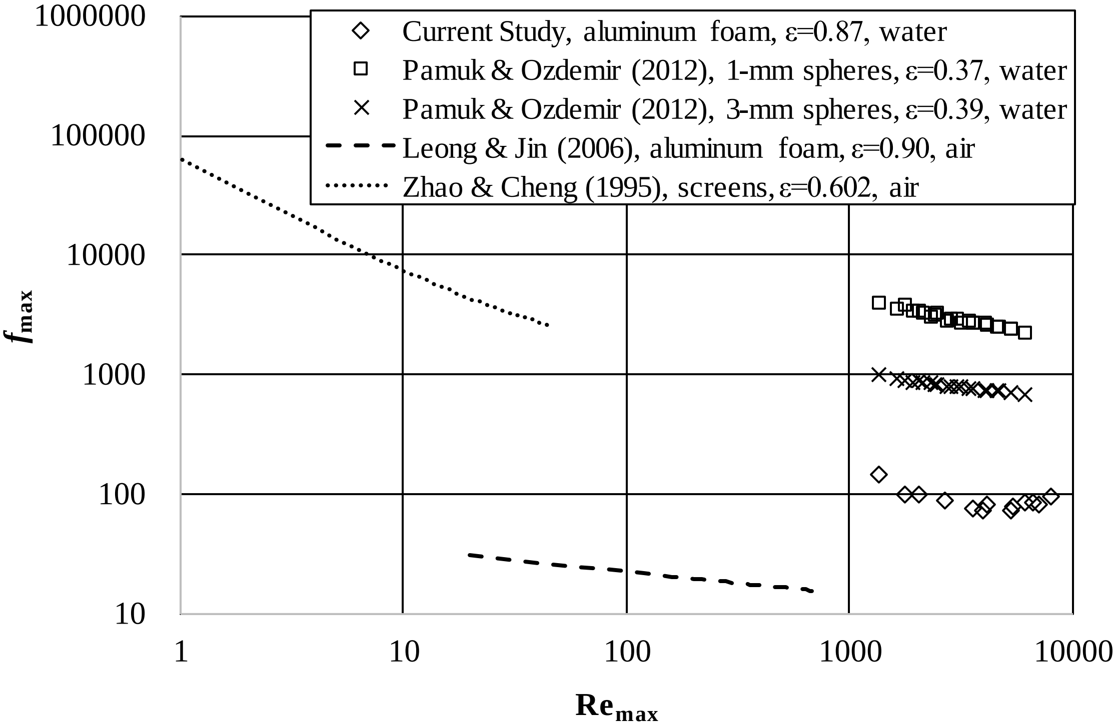

Figure 3.30 : Friction factor versus Reynolds number: oscillating flow of air and water in various porous media.

Other comparisons are made between the packed spheres of Pamuk and Özdemir [76] who also used water. It is seen that the friction factor in packed spheres is more than ten times higher than aluminum foam. The primary reason for this is the vast difference in porosity between the two porous media – 87.6% for the foam and around 36% and 39% for the spheres. Pamuk and Özdemir [76] did not report any frequency regime changes, possibly due to the high resistance to flow provided by tightly packed spheres. The friction factor for air flow in the woven screens of Zhao and Cheng [73], which had a porosity of 60.2%, sets higher than the friction factor for air and water flow in metal foam. One reason for this is the low porosity of the screens compared to that of metal foam. The friction factor and Reynolds number data of Zhao and Cheng [73] were extracted from a correlation provided by these authors.

4. HEAT TRANSFER EXPERIMENTS AND RESULTS

4.1 Steady-State Heat Transfer

As reported earlier, the test section was composed of a cylindrical aluminum tube and a commercial aluminum foam core which was brazed to the tube's internal surface. Brazing of the two similar metals minimized thermal contact resistance.

33 holes were drilled along the lateral surface of the aluminum tube and spanning only the porous region. The diameter of each hole was 1 mm and the depth was 4 mm, as seen in detail in Figure 4.1. Care was taken so as to leave equal distances of 10 mm between each hole excluding two holes at the top and the bottom ends of the porous region. Because those two holes were 1 mm away from the closest ends each, they were 11.5 mm away from the adjacent holes.

OMEGA K-type thermocouple wires with the designation code TT-K-30-SLE were used to acquire temperature data from the wall of the test section and the cross section of the polyethylene tubes. According to the designation code, the conductor wires, with a diameter of 30 AWG corresponding to 0.25 mm, were insulated with PFA (Perfluoroalkoxy). Their accuracy, as defined by the abbreviation "SLE" (Special Limit of Error) and as an ANSI standard, was ±1.1 °C or 0.4% of the measured temperature, depending on the greater value.

The thermocouple wires were firstly cut from the spool with equal lengths of 1.5 meters. For high accuracy, their tips were welded using OMEGA fine wire welder to obtain a bead junction with a diameter of 1 mm approximately.

The welded ends of the thermocouple wires were inserted in every hole on the tube wall until they touched the bottom, Figure 4.2 (a). Thermal epoxy then filled each hole, which guaranteed that there were no air pockets trapped in the holes, Figure 4.2 (b). As such, the wall temperature could be measured along the flow direction.

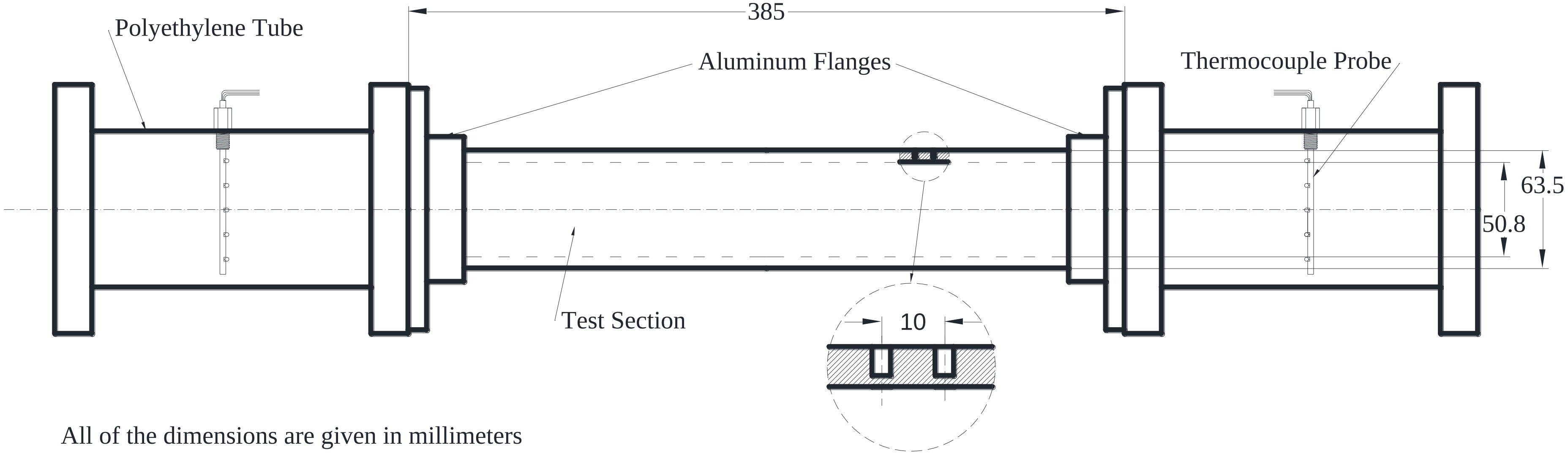

All of the dimensions are given in millimeters

Figure 4.1 : Detailed drawing of the assembly of the test section and the PE tubes and depiction all of the temperature measurement points.

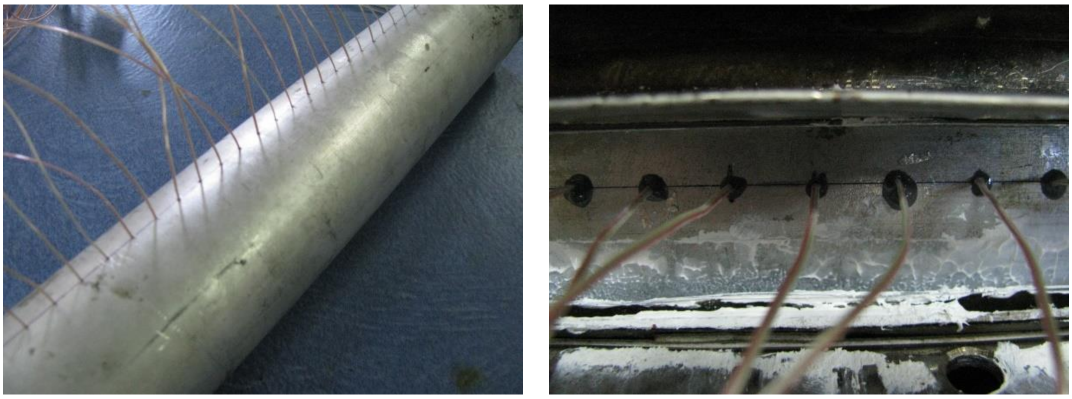
(a) **(b)**

Figure 4.2 : Outer surface of test section: (a) Thermocouples equidistantly inserted along the tube axis, (b) Thermal-epoxy-filled holes.

Before connecting the test section and the polyethylene tubes via the flanges, a surface band heater was wrapped around the tube by guiding along the axis, Figure 4.3 (a). Thermal grease was also placed between the heater surface and the pipe surface to minimize contact resistance. The heater had multiple resistance-heating ribbons each having 1.6628 Ohm/m, Figure 4.3 (b). Mica layers on both sides of the heating core provided electrical insulation; and steel sheet layers provided cover and structure to the heater. Between the outer steel sheet and the outmost mica, a set of 3 equally spaced thermocouple wires were placed for monitoring the heater temperature during each run. The heater was rated at electrical power of 1,780 Watts at 60 Volts. During the experiment, the heater was powered by two 40-VDC power supplies connected in series.


(a) **(b)**

Figure 4.3 : The surface band heater: (a) The heater wrapped around the tube, (b) The heating core component of the heater.

The whole assembly was then covered with five layers of ceramic fiber paper (4-mm thick) with thermal conductivity 0.058 W/mK in order to insulate the test section from ambient air, as Figure 4.4 (a) and (b) show in detail.

The surface of the tube which was not covered by the heater were threaded for assembling the flanges. Before connecting the flanges, teflon sealant tape was wrapped around the thread of the tube. In addition, to prevent leakage due to thermal expansion, thermally resistant silicone was placed along the circular line between the flange and the tube end. The system was made further water-proof by also using full-face fiber gaskets between polyethylene tubes, flanges and the rest of the system.

The heat transfer test section was connected to two 50.8-mm-diameter 190-mm-long polyethylene tubes - one at each side - using flanges. The upstream and downstream fluid temperatures were measured in these parts employing 5-point temperature probes. These probes were designed for the purpose of obtaining temperature data as many points as possible. 5 thermocouple wires with welded tips were inserted into a stainless steel tube, 3 mm in inner diameter, Figure 4.5, parts (a) and (b). Those tips were emerged from 5 different holes along a portion of the steel tube equal to the inner diameter in length. An adhesive sealant was used to prevent intrusion of water into the steel tube. The holes were equidistantly drilled, 10.2 mm apart from to each other. However the ones at the two ends were only 5 mm away from the inner walls of the polyethylene tubes, Figure 4.6. The outlets of the polyethylene tubes were connected to stainless steel pipes 32 mm in diameter and 110 cm in length. The outlet of one steel pipe dispensed water into a drain.

The surface of the tube which was not covered by the heater were threaded for assembling the flanges. Before connecting the flanges, teflon sealant tape was wrapped around the thread of the tube. In addition, to prevent leakage due to thermal expansion, thermally resistant silicone was placed along the circular line between the flange and the tube end. The system was made further water-proof by also using full-face fiber gaskets between polyethylene tubes, flanges and the rest of the system.

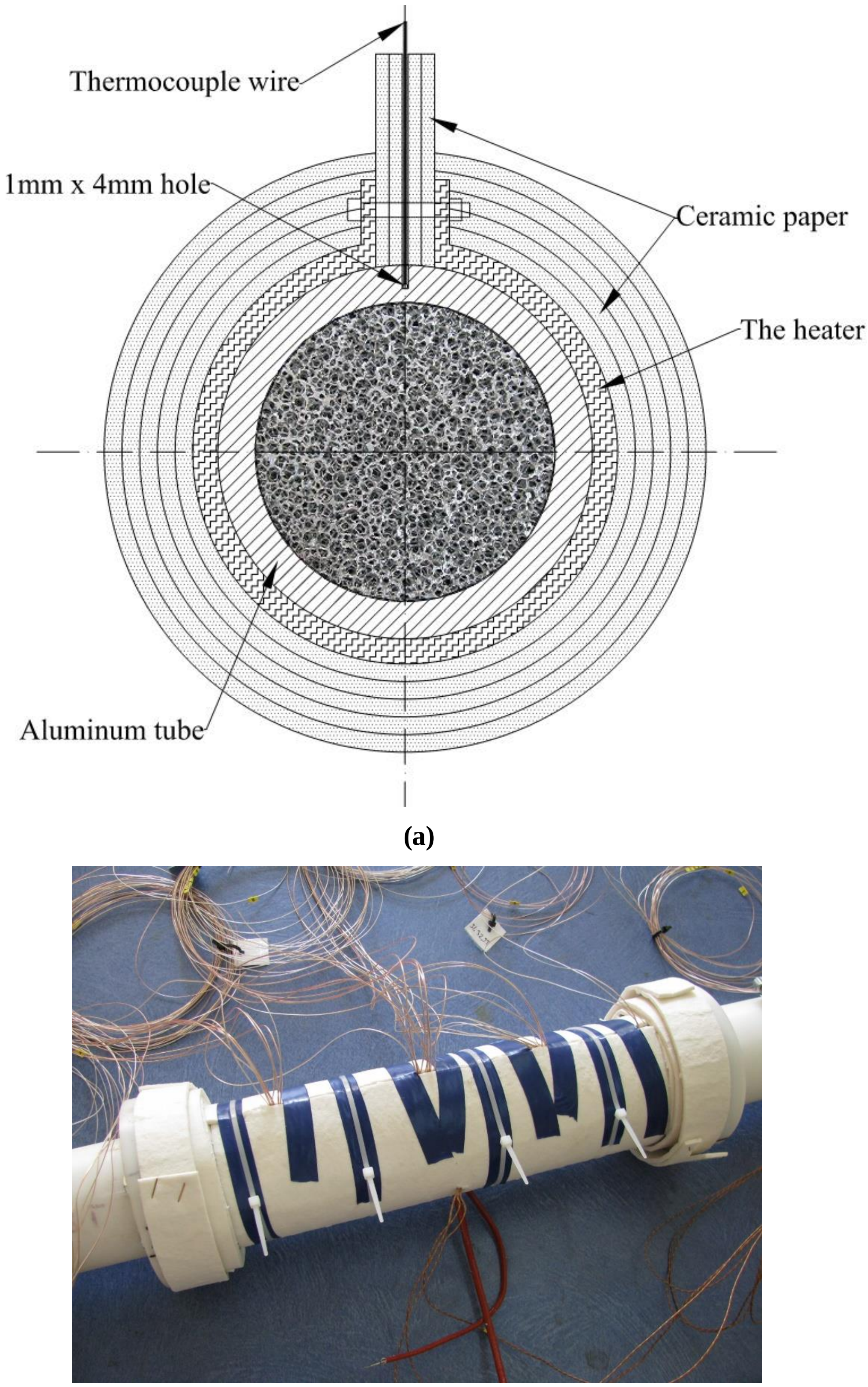

(a)

(b)

Figure 4.4 : Heat transfer test section: (a) Cross-sectional view of the foam core and the outer components (b) Photograph of the test section ready for assembling to the rest of the experiment set-up.

The heat transfer test section was connected to two 50.8-mm-diameter 190-mm-long polyethylene tubes - one at each side - using flanges. The upstream and downstream fluid temperatures were measured in these parts employing 5-point temperature probes. These probes were designed for the purpose of obtaining temperature data as many points as possible. 5 thermocouple wires with welded tips were inserted into a stainless steel tube, 3 mm in inner diameter, Figure 4.5, parts (a) and (b). Those tips were emerged from 5 different holes along a portion of the steel tube equal to the inner diameter in length. An adhesive sealant was used to prevent intrusion of water into the steel tube. The holes were equidistantly drilled, 10.2 mm apart from to each other. However the ones at the two ends were only 5 mm away from the inner walls of the polyethylene tubes, Figure 4.6. The outlets of the polyethylene tubes were connected to stainless steel pipes 32 mm in diameter and 110 cm in length. The outlet of one steel pipe dispensed water into a drain.

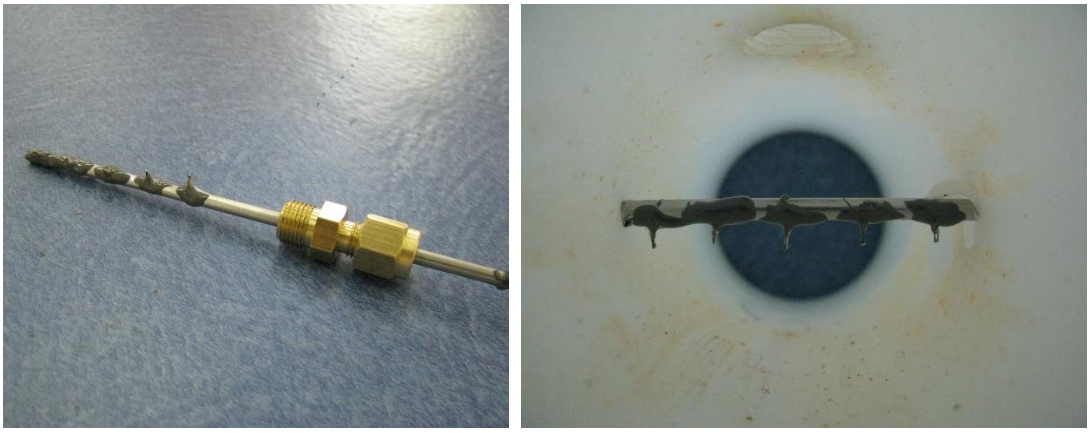

(a) **(b)**

Figure 4.5 : Temperature probe for measuring the inlet or outlet temperature: (a) Probe after production, (b) Probe spanning the flow zone inside the polyethylene tube.

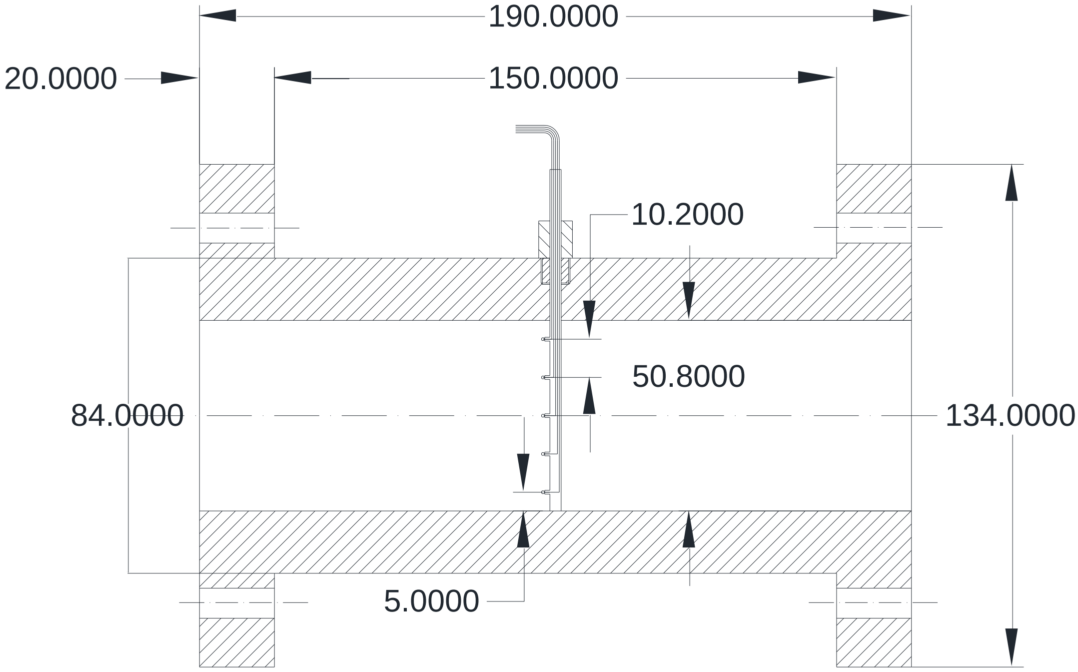

Figure 4.6 : Detailed drawing of a polyethylene tube and the inserted temperature probe.

For a given run, a valve at the inlet of the test section provided fine control over mass flow rates of water flow from the elevated tank. Heat was supplied by the heater to provide 15,518 W/m^2 for low flow rates (8.72–15.02 g/s) and 26,865 W/m^2 for higher flow rates. These fluxes were based on the inside diameter of the pipe, and they excluded an estimated heat loss of about 8.2% to the surrounding.

The system reached at steady-state conditions after about 30 min. At steady state the flow rate was measured using a Sika VMI07 magnetic inductive flow sensor at the inlet of the 110-cm steel pipe located upstream, and the average flow velocity were determined. The flowmeter gave an analogue output between 4-20 mA, and it had a range of 20 liters per minute with an accuracy of ±1.25% of the reading. The connections of the flowmeter and the free leads of the thermocouples were connected to a data logger, which sent all of the readings to a computer.

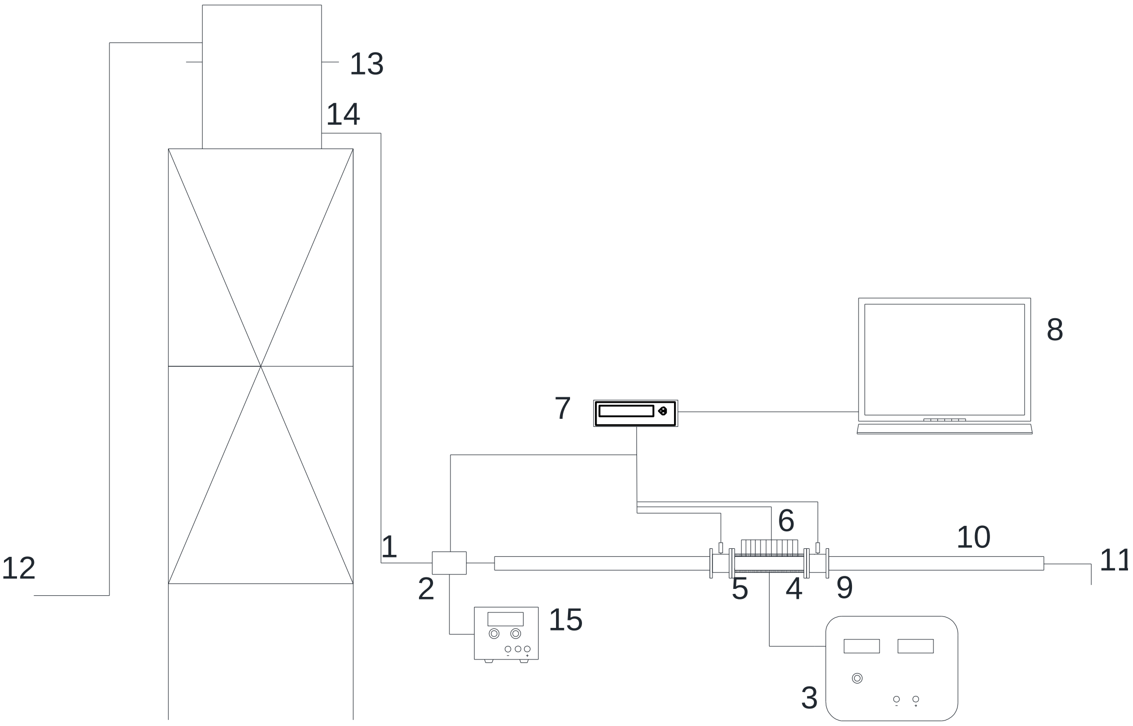

Figure 4.7 : Schematic of the experimental set-up: 1. Filtered water inlet, 2. Magnetic flow meter, 3. DC power supply, 4. Heater, 5. Test section (Metal foam), 6. Thermocouple wires, 7. Data logger, 8. Computer, 9. Polyethylene tube, 10. Stainless steel tube, 11. Water outlet, 12. Inlet from the water network, 13. Level control outlets, 14. 50-liter elevated tank, 15. DC power supply for the magnetic flow meter.

4.1.1 Uncertainty analysis

Length, mass, time and temperature were directly measured. Uncertainty in these quantities was based in errors provided by device manufacturers. The uncertainties in length and diameter of the foam were 0.18% and 1.0%, respectively.

The propagation of error in derived quantities, i.e., average flow velocity, Reynolds number and Nusselt number, was assessed via uncertainty analysis [94]. The uncertainty in Reynolds and Nusselt numbers were obtained as ±2.69% and ±14.12%, respectively.

The effective thermal conductivity of the solid aluminum ligaments of the foam was obtained from an analytical one-dimensional model given by Calmidi and Mahajan [106]. These researchers indicated that this model was excellent in matching their measured values of the effective conductivity. The fluid phase effective thermal conductivity was obtained as 0.58 W/m.K. Similarly, the uncertainty in the effective conductivity was conservatively assumed to be 10%. The uncertainty in the heat flux was assumed to be 10%.

4.1.2 Results

Heat transfer runs covered Darcy, transitional and Forchheimer regimes. These regimes have been identified previously by flow experiments using the same set-up and water at room temperature [90]. It was verified by preliminary experiments that increasing the water temperature due to heat at the wall caused little changes in the thermophysical properties of the water, which did not affect flow-regime demarcations obtained by water at room temperature as was done in [90].

The wall temperature along the foam tube is shown in Figure 4.8 (a) for the Darcy regime data; and is seen to increase in the flow direction. This trend is expected and very similar to what is provided in other experimental studies, e.g., Calmidi and Mahajan [32], Kurtbas and Celik [62] and Dukhan et al. [65]. The wall temperature is lower for higher flow velocities indicating better heat transfer rates at higher velocities.

For each velocity, the slope of wall temperature initially changes and then becomes constant at about 103 mm from the inlet (two tube diameters approximately) for all three Darcy velocities until about a distance of 282 mm. For the constant-slope region, the solid straight lines for each case have curve-fit factor R^2 greater than 0.99. The constant slope of the wall temperature decreases slightly as the velocity increases, and it is indeed a sign of thermally fully-developed heat transfer [37,107]:

$$\frac{\mathrm{d}T_w}{\mathrm{d}z} = \text{constant} \tag{4.1}$$

It can be stated that, for Darcy flow, the thermal entry length is two tube diameters and is independent of flow velocity.

After z = 282 mm, there is a sudden change from increasing to decreasing slope, for all velocities. This is most likely an exit effect, which prevails until the outlet of the foam. The exit region has a length of 23 mm, which can be significant depending on the size of metal foam, and is invariably ignored in the literature.

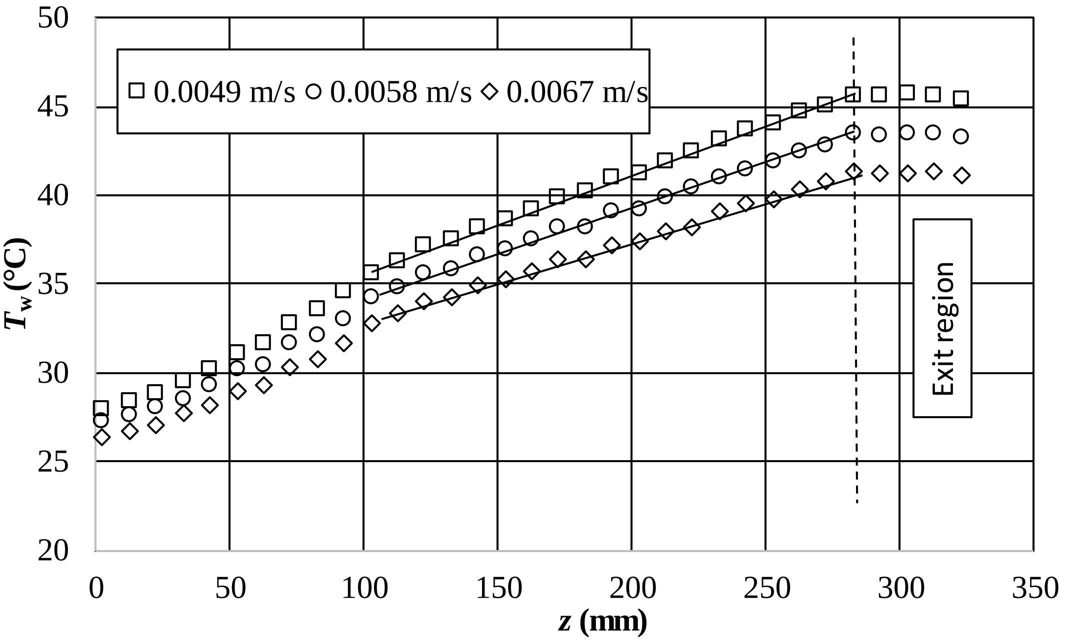

(a)

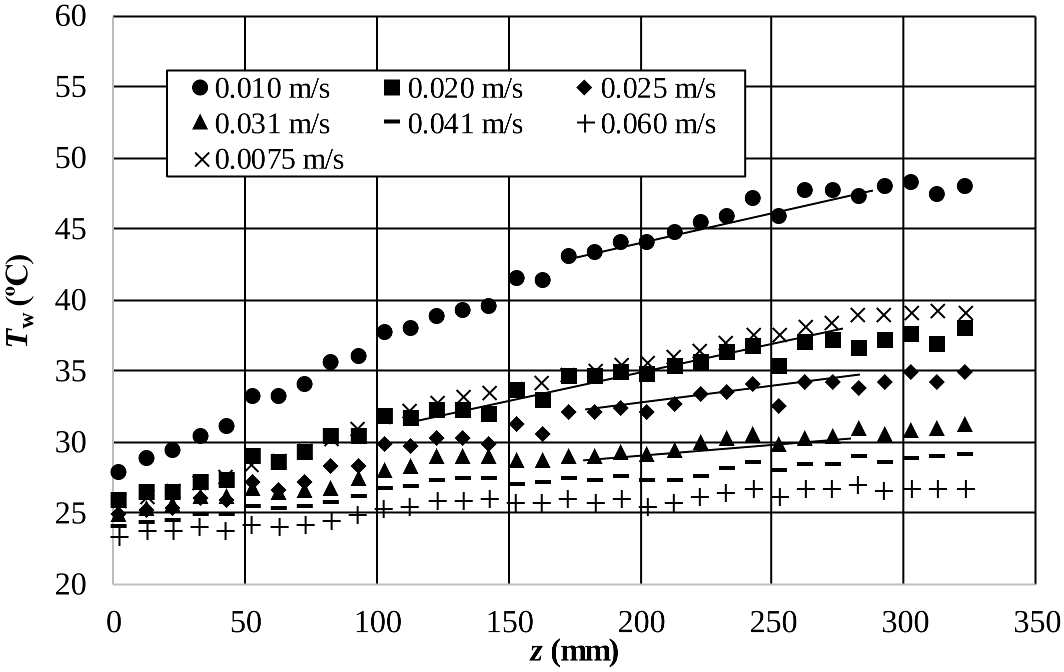

(b)

Figure 4.8 : Wall temperature points excluding the zone affected by the exit of the foam: (a) Darcy-flow cases, (b) Non-Darcy flow cases.

As the flow velocity increases, inertial effects become important and the flow regime becomes non-Darcy (transitional and Forchheimer) [90]. For such flow, Figure 4.8 (b) shows similar trends for non-Darcy flows as presented in Figure 4.8 (a) for Darcy flow, especially for the lower velocity cases of 0.010, 0.020, 0.025 and 0.031 m/s. The solid lines represent linear curve fits. They were systematically obtained by excluding data points that reduce the correlation factor R^2. As such the left-hand beginning of each solid line represents the end of the thermally developing region and the start of the fully developed region. It should be noted that the case for flow velocity of 0.0075 m/s, was subjected to a lower heat flux (15,518 W/m^2) compared to the rest of the cases in Figure 4.8 (b) which were subjected to 26,865 W/m^2.

The thermal entry length is shown in Figure 4.9. In terms of internal tube diameter, the entry length for metal foam obtained experimentally for Darcy flow was constant at about two tube diameters. For the non-Darcy cases, the entry length was also constant but much longer, approximately 3.4 diameters.

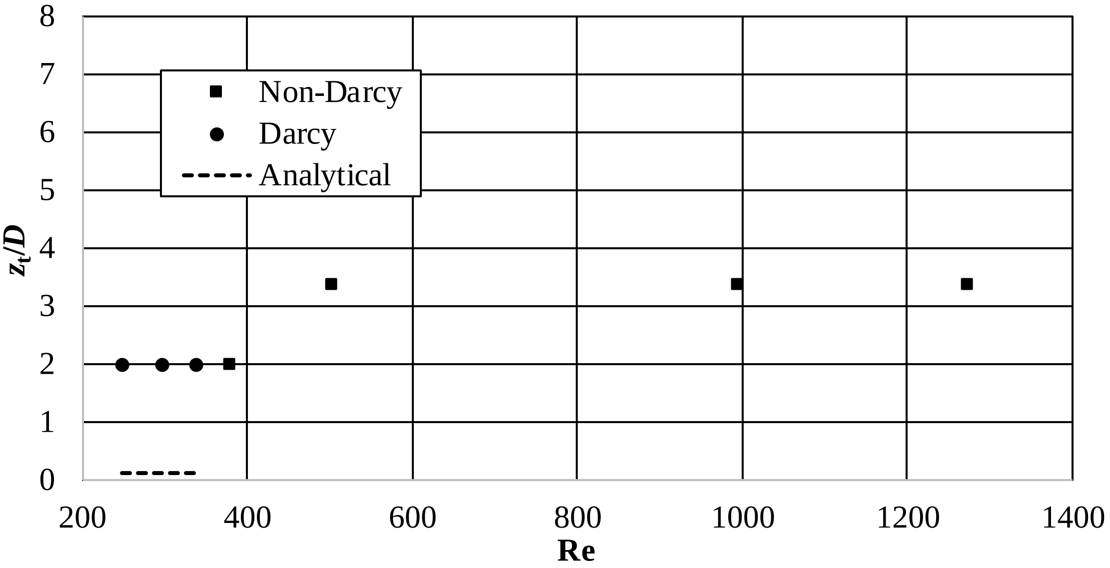

Figure 4.9 : Dimensionless thermal entry length as function of Reynolds number.

Nield et al. [46] analytically investigated thermal entry length for the case of a circular-tube porous media subjected to constant heat flux assuming local thermal equilibrium between the solid and fluid phases in the porous medium. In the current nomenclature, the thermal entry length z_t was obtained by Nield et al. [46] as

$$\left(\frac{z_t}{4r_0 Pe'} \right)^{1/2} \cong 0.1 \tag{4.2}$$

Where Pe' is the Péclet number defined by

$$Pe' = \frac{\rho c_p r_0 U}{k_e} \tag{4.3}$$

The entry length predicted by Equation (4.2) for the Darcy-flow data of the current study was a very weak function of velocity, and had values of 0.13, 0.14 and 0.15 tube diameters for the Darcy velocities 0.0049, 0.0058 and 0.0067 m/s, respectively. These values are significantly lower than the entry length obtained experimentally (two diameters). This large difference is due in part to the local thermal equilibrium assumption employed by Nield et al. [46] and their disregarding of the hydrodynamic entry length in their analysis, which was shown to be significant in metal foam, [108]. Another important cause of this difference may be attributed to the nature of the internal structure of metal foam (web of thin fibers surrounding relatively large open cells), as well as the very high porosity of metal foam. These two factors logically suggest that confined metal foam should have some attributes of open-pipe flow and heat transfer, in addition to having attributes of porous-media flow and heat transfer. For forced convection due to laminar flow in an open pipe with an internal diameter *D* and subjected to constant wall heat flux, the thermal entry length is usually given as [109]

$$\frac{z_t}{D} = 0.05\,\mathrm{Re}\,\mathrm{Pr} \tag{4.4}$$

where Pr is the Prandtl number. For the current case, the thermal entry length for the Darcy cases is in the order of a hundred diameters. For turbulent flow, the thermal entry length is ten diameters [109].

4.1.2.1 Estimation of bulk temperature

The bulk fluid temperature is defined by

$$T_b = \frac{1}{UA}\int_A uT\mathrm{d}A \tag{4.5}$$

Where *U* is the average flow velocity and *A* is the cross-sectional area. An accurate value of the bulk temperature of water along the tube is rather difficult to obtain experimentally. In the thermally fully-developed region, a reasonable estimation of the bulk temperature is inferred from the average water temperature at the exit (as an estimate of the exit bulk temperature) and the well-established analytical fact, e.g., [37], that for thermal fully-developed conditions

$$\frac{\mathrm{d}T_b}{\mathrm{dz}} = \frac{\mathrm{d}T_w}{\mathrm{dz}} = \text{constant} \qquad \textbf{(4.6)}$$

This constant slope is readily available from plots of the wall temperature (Figure 4.8). This is sufficient to obtain a straight line representing the variation of bulk temperature in the fully-developed region, namely

$$T_{bFD} = c_1 z + c_2 \qquad \textbf{(4.7)}$$

where c_1 and c_2 are constants given in Table 4.1.

In the developing region, the bulk fluid temperature is estimated by a line connecting the bulk fluid temperature at the lower boundary of the fully-developed region and the bulk fluid inlet temperature, which is approximately equal to the average temperature of the fluid at the inlet. The bulk temperature at the lower boundary of the fully-developed region can be obtained from Equation (4.7) and knowledge of the thermal entrance length obtained from the behavior of the wall temperature. The variation of the bulk fluid temperature in the entry region is thus given by

$$T_{bD} = d_1 z + d_2 \qquad \textbf{(4.8)}$$

where d_1 and d_2 are constants given in Table 4.1.

Table 4.1 : Constants for bulk temperature.

Average Velocity (m/s)	c_1(°C/mm)	c_2(°C)	d_1(°C/mm)	d_2(°C)
0.0049	0.055	19.57	0.037	21.34
0.0058	0.050	18.22	0.019	21.35
0.0067	0.046	17.52	0.013	21.01
0.0100	0.041	21.43	0.046	20.69
0.0200	0.039	18.76	0.016	21.08
0.0250	0.024	21.20	0.029	20.31
0.0310	0.020	19.91	0.018	20.37

Even though the bulk temperature obtained in the manner outlined above contains few approximations, the use of such temperature is preferred for estimating Nu as opposed to using a constant temperature, e.g., the inlet temperature or an average of the inlet and outlet temperatures, which is constant and does not really capture the actual thermal phenomenon inside the foam.

4.1.2.2 Local Nusselt number

Another way of viewing thermal development is to inspect the variation of the local Nusselt number along flow direction. The local Nusselt number is defined as [46]

$$\mathrm{Nu} = \frac{Dq''}{k_{\mathrm{fe}}\left(T_{\mathrm{w}} - T_{\mathrm{b}}\right)} \tag{4.9}$$

where k_{fe} is the effective thermal conductivity of the fluid (obtained from Calmidi and Mahajan [106]). Using T_{bD} and T_{bFD} for the developing and fully-developed regions, respectively, the Nusselt number was calculated according to Equation (4.9).

Nusselt numbers are shown in Figure 4.10; part (a) is for Darcy regime and part (b) is for non-Darcy regimes. For Darcy regime, Nu is seen to be a function of velocity in the thermal entry region, after which it is generally constant (independent of distance along the foam and of velocity), for the three Darcy velocities, which is a confirmation of thermal full development condition observed in the behavior of the wall temperature. The exit region is clearly shown to start at an axial distance of about 5.7 pipe diameters from the entrance, which is in agreement with the observation made earlier using the behavior of the wall temperature.

For Darcy flow in porous media subjected to constant heat flux, and for local thermal equilibrium between the solid and fluid phases, the theoretical Nu is [46,99]:

$$\mathrm{Nu}_{\mathrm{LTE}} = \frac{Dq''}{k_{\mathrm{e}}\left(T_{\mathrm{w}} - T_{\mathrm{b}}\right)} = 8 \tag{4.10}$$

where k_{e} is the effective thermal conductivity of the porous medium, and the subscript LTE signifies thermal equilibrium. According to Equation (4.10), Nu is independent of flow velocity and of distance along flow direction. This is consistent with the trends in the current study for Darcy flow, as seen in Figure 4.10 (a).

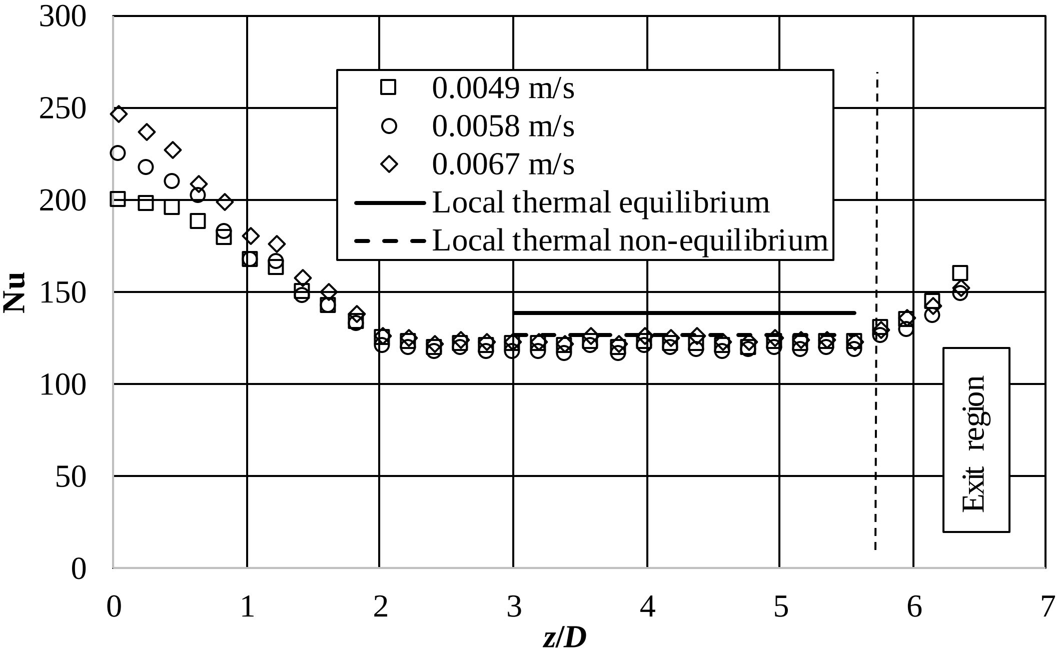

(a)

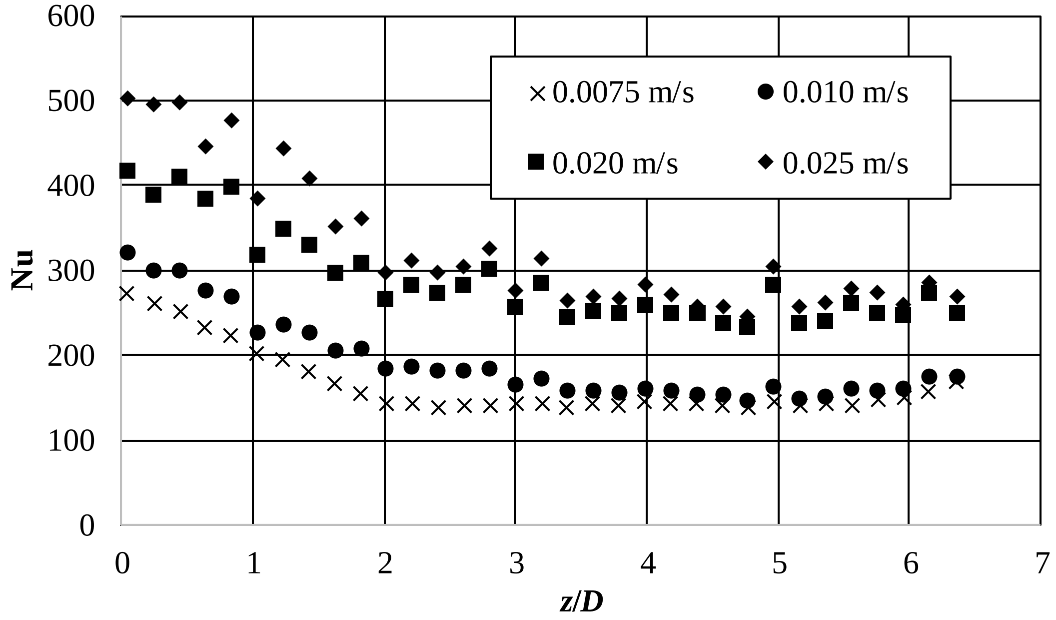

(b)

Figure 4.10 : Nusselt number along the foam excluding the zone affected by the exit region: (a) Darcy regime and comparison to analytical local-thermal-equilibrium and local-thermal-non-equilibrium solutions. (b) Non-Darcy regimes.

In Equation (4.10), the effective conductivity k_e means the total effective conductivity of the solid and fluid combined (the porous medium). The Nusselt number, Equation (4.9), in the current study is defined based on the effective thermal conductivity of the fluid (water) k_{fe}. Therefore, in order to compare the Darcy-flow results of the current study to the analytical prediction of Equation (4.10), Nu had to be adjusted according to

$$\mathrm{Nu}=\mathrm{Nu}_{\mathrm{LTE}}\frac{k_{\mathrm{e}}}{k_{\mathrm{fe}}} \tag{4.11}$$

The ratio of the effective conductivities was obtained by correlations provided by Calmidi and Mahajan [106] as 17.38, for which the analytical Nu has a value of 139.09. The average value of Nu for the three Darcy-flow cases of this study in the fully-developed region is 124.14. The difference between the two values of Nu is 12.04%, which is acceptable considering the estimation of various parameters and experimental errors. However, the analysis seems to consistently over-predict Nu most likely due to assumption of local thermal equilibrium employed by the analytical solution.

Yang et al. [110] provided analytical results for fully-developed forced convection in a tube filled with a porous medium and subjected to constant wall heat flux. Local thermal non-equilibrium and slug flow were employed. They indicated that local thermal equilibrium was invalid for the case of constant wall heat flux. The analysis was intricate in the sense that it employed the effective porosity concept which accounts for the effect of tortuosity on the stagnant thermal conductivity. For the Darcy velocities of the current study, the parameter λD (λ is a combination of stagnant, dispersion, fluid and solid thermal conductivities of the foam, volumetric heat transfer coefficient and the effective porosity [108]) varies between 766 and 779 which is much greater than unity. Moreover, the difference between the solid and fluid conductivities is very high; hence the effective porosity, ε^*, can be simplified to $(2+\varepsilon)/3$. These simplifications lead to the following expression for the fully-developed Nusselt number:

$$\mathrm{Nu}_{\mathrm{LTNE}}=\frac{Dq''}{k_{\mathrm{fe}}\left(T_{\mathrm{w}}-T_{\mathrm{b}}\right)}=8\left[\frac{2+\varepsilon}{3}+\sigma\left(\frac{1-\varepsilon}{3}\right)+\frac{\varepsilon k_{\mathrm{dis}}}{k_{\mathrm{f}}}\right] \tag{4.12}$$

where σ is the ratio of solid to fluid conductivities and has a value of 335. Various thermal conductivities, including the thermal dispersion conductivity k_{dis} were found by employing correlations proposed by Calmidi and Mahajan [32,106]. The Nusselt numbers for the three Darcy velocities of the current study that were obtained by

Equation (4.12) are plotted in Figure 4.10 (a) for comparison. The solution of [62,110] predicts a fully-developed Nusselt number that is a weak function of flow velocity. It is seen in Figure 4.10 (a) that the analytical solution for local thermal non-equilibrium matches the experimental data extremely well (within a maximum difference of 4.6%). This indicates that the assumption of local thermal non-equilibrium is more appropriate for convection in metal foam with water flow.

Figure 4.10 (b) shows that higher velocities (non-Darcy flow) produce significantly higher Nusselt numbers. For the transitional velocity of 0.0075, Nu is seen to approach a constant value after the entry region. For higher velocities (0.010, 0.020 and 0.025 m/s), there is a significant increase in Nu, which may be due to regime change from transitional to Forchheimer. An interesting, seemingly periodic, behavior for these high velocities is displayed. This trend may signify possible periodic development where the heat transfer alternate between developing and almost developed states with decaying amplitude. Similar behavior was present in the work of Kurtbaş and Çelik [62] for air flow in a foam-filled rectangular channel. There, the behavior was explained by considering buoyancy-driven secondary flows and a change in cell velocity. The periodic behavior in Nu may be related to a flow phenomenon inside the cells of the foam, e.g., formation of inertial cores. For the highest three velocities 0.031, 0.041 and 0.060 m/s, the heat transfer was enhanced significantly and the overall change in wall temperature along the foam was relatively low, which added to the relative uncertainty in the data. As such a Nusselt number could not be obtained accurately for these cases.

4.1.2.3 Correlation for fully-developed Nusselt number

In the fully-developed region, it is possible to plot the obtained Nusselt number as a function of Reynolds number as seen in Figure 4.11. As expected by theory [46] and shown in experimental data [66], Nu is independent of Re in Darcy flow regime. For the non-Darcy cases, Nusselt number is a strong function of Reynolds number according to a power law:

$$Nu = 5.91\mathrm{Re}^{0.53} \tag{4.13}$$

The power-law relation between Nu and Re for non-Darcy flow is common [32,61,66].

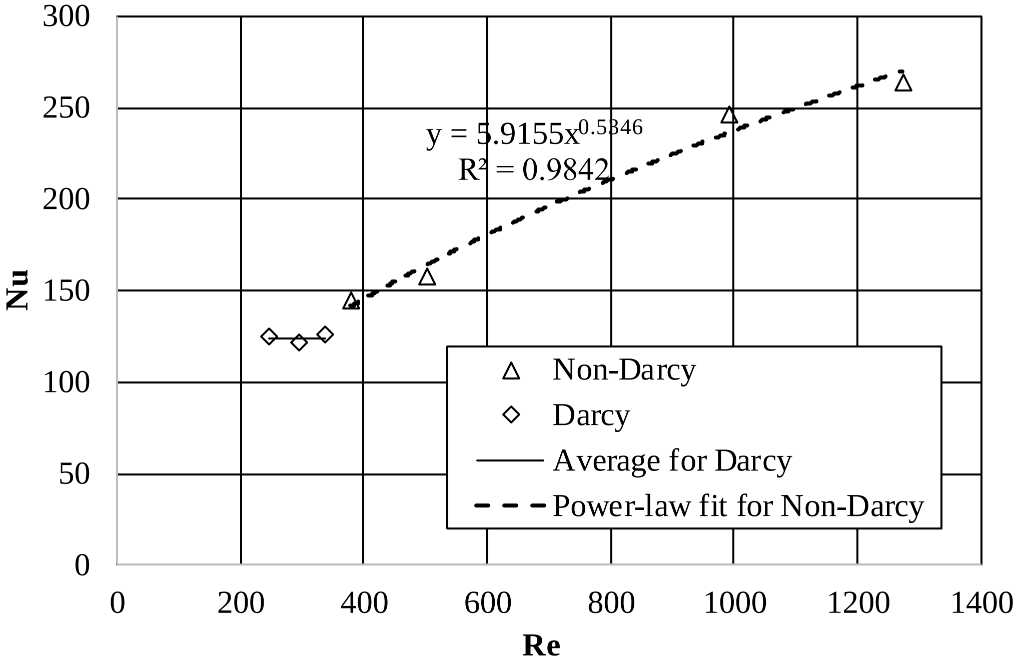

Figure 4.11 : Nusselt number variation with Reynolds number for Darcy and non-Darcy flows.

4.2 Oscillating heat transfer

Figure 4.12 is a schematic of the complete experimental setup. The test section prepared for steady-state heat transfer runs was used for the oscillating heat transfer experiments. Only the open system was changed into a closed reciprocating cycle by connecting the ends of the concentric steel pipes to the double-acting piston mechanism in the same way explained in Section 3.3. In addition, the annular parts of the steel pipes were in connection with two cooling thermostats (LAUDA Alpha RA 8) with a cooling capacity of 0.225 kW in order to provide cold water for the removal of heat supplied to the test section and to avoid overheating.

For a given run, the water coolers were switched on until they could provide cooling water at about 17 °C. The heater was then switched on to provide the desired constant wall heat flux to the foam pipe. The stroke length of the piston was set to a desired value, the oscillating generator was switched on, and the oscillating frequency was ramped to a targeted level. After the system stabilized (2.5 hours approximately), a Keithley 2700 XLINX data acquisition system, installed in a computer, communicated with a data logger and recorded signals from all sensors. A signal from a clicker that touched a small bump on a flywheel (part of the oscillation system) once per cycle;

was used to calculate the angular speed. The sampling rate changed between 10 and 30 readings per second depending on device limitations. At displacement of piston 130 mm, 170 mm and 195 mm, measurements at line frequencies of 5, 10, 15, 20, 25 and 30 Hz were sought.

The uncertainties in derived quantities angular frequency and maximum fluid displacement were estimated at 0.43% and 0.51%, respectively [88].

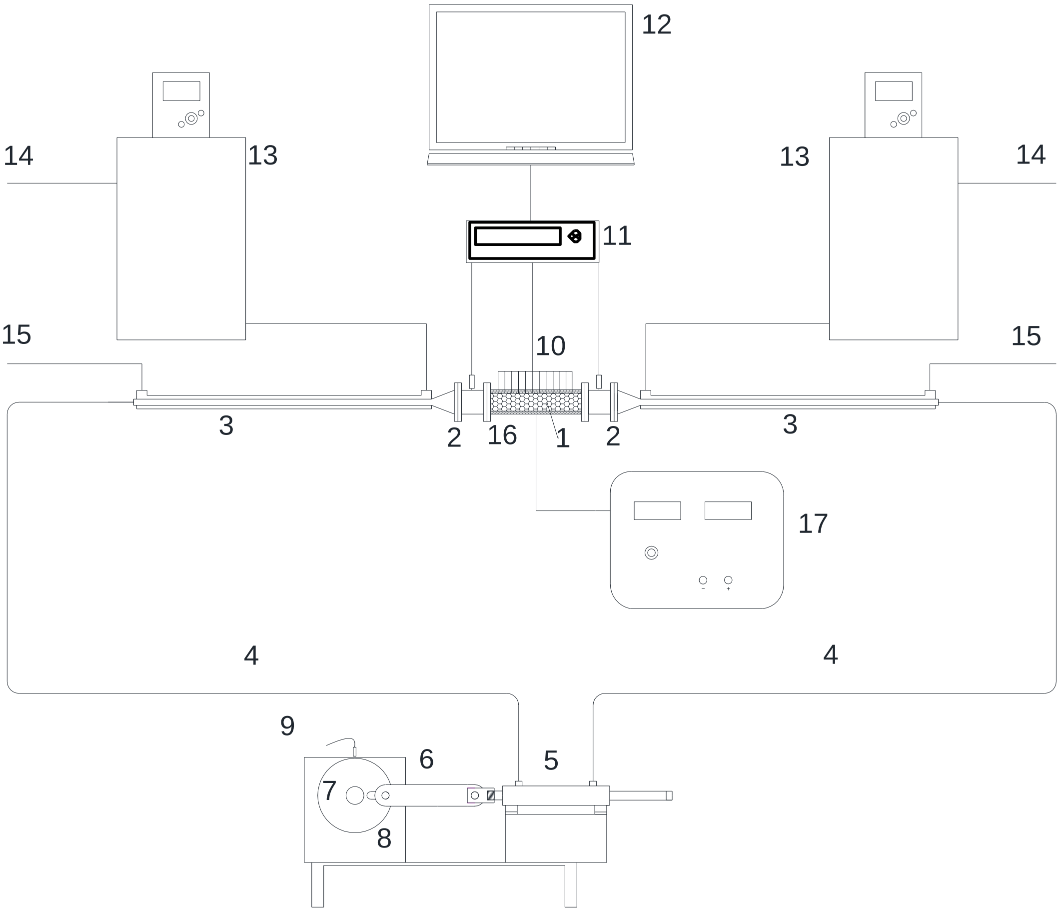

Figure 4.12 : Schematic of Experimental Setup: 1. Test Section (metal foam), 2. Polyethylene Tubes, 3. Steel Pipes, 4. Connecting Hoses, 5. Oscillation Generator, 6. Crank Arm, 7. Flywheel, 8. Motoreductor, 9. Inductive Proximity Sensor, 10. Thermocouple Wires (from metal foam and polyethylene tubes), 11. Data Logger, 12. Computer, 13. Cooling Thermostats, 14. Water Inlet for Thermostats, 15. Water Outlet, 16. Heater, 17. DC-power supply.

4.2.1 Results

The maximum fluid displacements ($x_{\max}$) are related to the displacements of the piston according to conservation of mass, as also previously described in Section 3.3.1 and the fact that water is incompressible. The maximum fluid displacements were calculated as 74.4 mm, 97.2 mm and 111.5 mm. The non-dimensional displacement is

$$A_0 = \frac{x_{\max}}{D} \tag{4.14}$$

where D is the foam pipe inner diameter. A_0 values for short, medium and long maximum fluid displacements were found as 1.5, 1.9 and 2.2, respectively.

For each displacement, line frequency was changed from 5 Hz to 30 Hz by a servo drive of motor. Actual flow frequency, which was linearly proportional to line frequency, changed from 0.116 to 0.696 Hz. The volume of fluid displaced by the piston, which was directly proportional to the diameter of the flywheel, was essentially the same as the volumetric fluid displacement through the test section since water is incompressible. Hence, as described in Section 3.3.1 at the entrance of the foam, the transient fluid displacement x_m, and the cross-sectional mean fluid velocity u were functions of angular frequency ω and time t. The reader can refer to the same section for the expression for the kinetic Reynolds number Re_ω. The values of the kinetic Reynolds number targeted were in the range 1873 to 9366. These values correspond to flow frequencies 0.116 to 0.696 Hz.

Preliminary runs established symmetry of the test section around the midpoint of the foam pipe. Those runs were conducted at the longest fluid displacement and the lowest frequency with a heat flux of 8866.13 W/m^2. Figure 4.13 (a) shows the temporal change of temperature values along the foam wall. The wall temperature was seen to be maximum at the midpoint (z/D= 3.2) and it decayed gradually to reach a minimum at the two inlets as seen in Figure 4.13 (b). Due to symmetry, only one half of the test section (z/D= 0.04 to 3.2) was subjected to further measurements, which reduced the load on the limited data acquisition system, without loss of critical information.

Figure 4.14 shows the wall temperature at various locations along half of the foam pipe as well as the flow velocity as functions of time for non-dimensional displacement A_0= 1.5. Parts (a) through (e) are for kinetic Reynolds numbers 1873, 3746, 5619, 7493 and 9366, respectively. There is no oscillation of the wall temperature at the middle point of the test section (z/D= 3.20) as expected due to symmetry and uniformity. The wall temperature oscillation is in phase with velocity for all kinetic Reynolds numbers (or frequencies). For porous media made of packed steel spheres of porosities 35% and 36.6%, Pamuk and Özdemir [77] reported a phase shift of π radians between velocity and wall temperature. Differences in porosity, thermal conductivity and internal structure between packed steel spheres and open-cell aluminum foam are responsible for this phase shift. Phase shifts were also present in Pathak et al. [80] for heat transfer due to oscillating helium flow in a 75%-porous medium composed of square cylinders. There was no mention or discussion of a phase shift between velocity and wall temperature in oscillating heat transfer studies due to air flow in metal and graphite foams [79,85-87]. The plots in these studies did not show any phase shifts either.

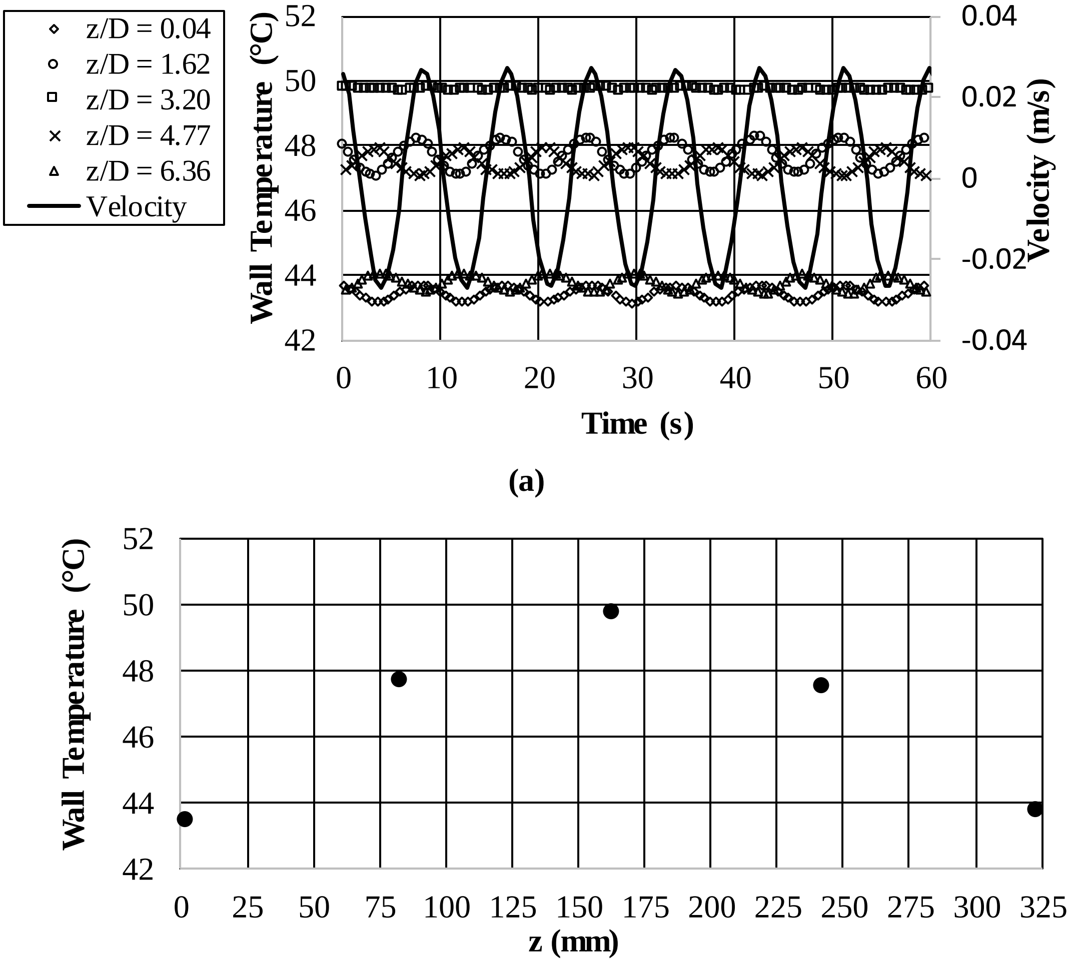

(a)

(b)

Figure 4.13 : Plots for testing symmetry of temperature along the foam wall: (a) Transient temperature values from equally-spaced points along the foam wall, (b) Cycle-averaged temperature values from the same run along the foam wall.

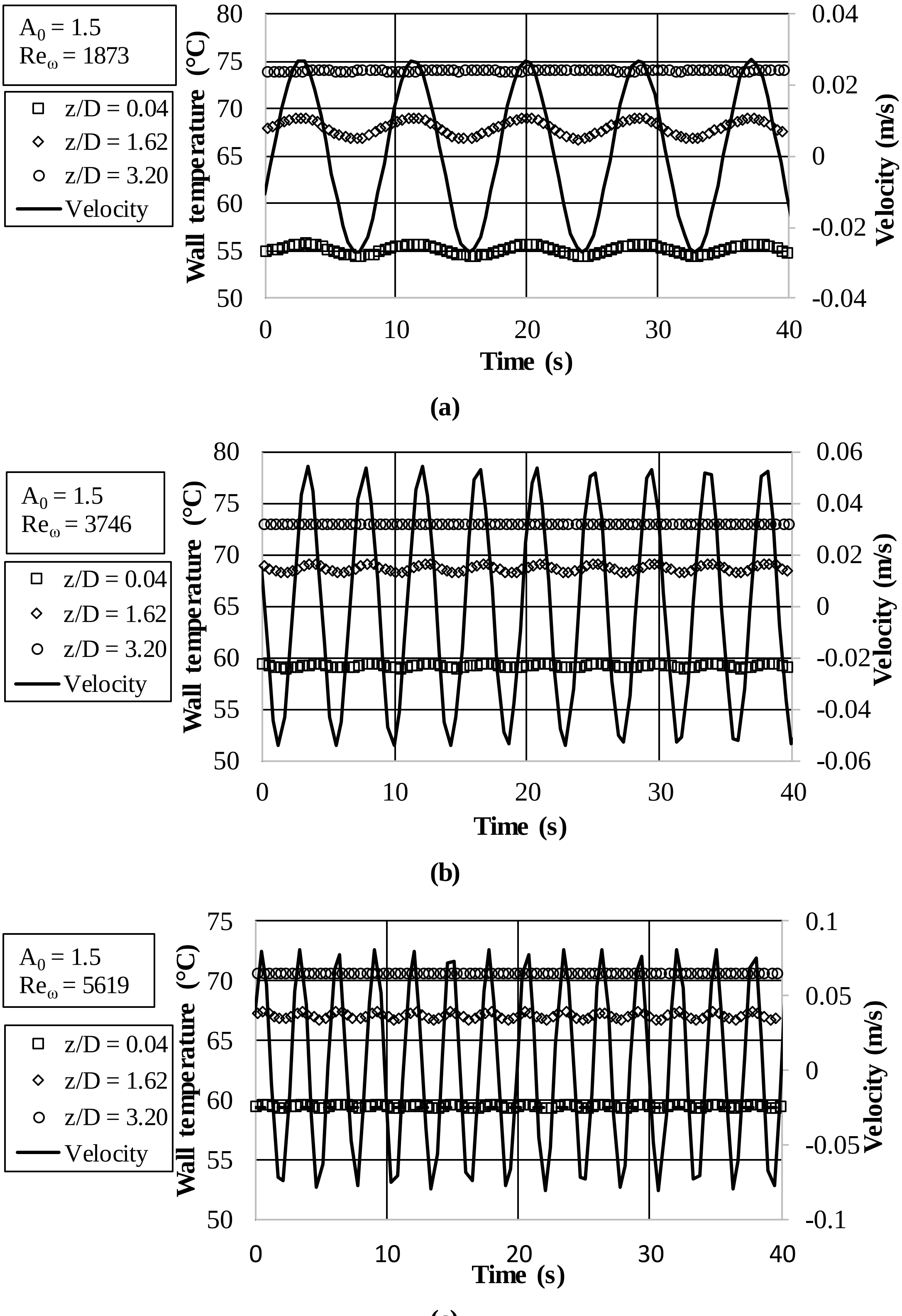

(a)

(b)

(c)

Figure 4.14 : Wall temperature and flow velocity as functions of time for fluid displacement A_0= 1.5 for (a) Re$_\omega$= 1873, (b) Re$_\omega$= 3746, (c) Re$_\omega$= 5619, (d) Re$_\omega$=7493 and (e) Re$_\omega$=9366.

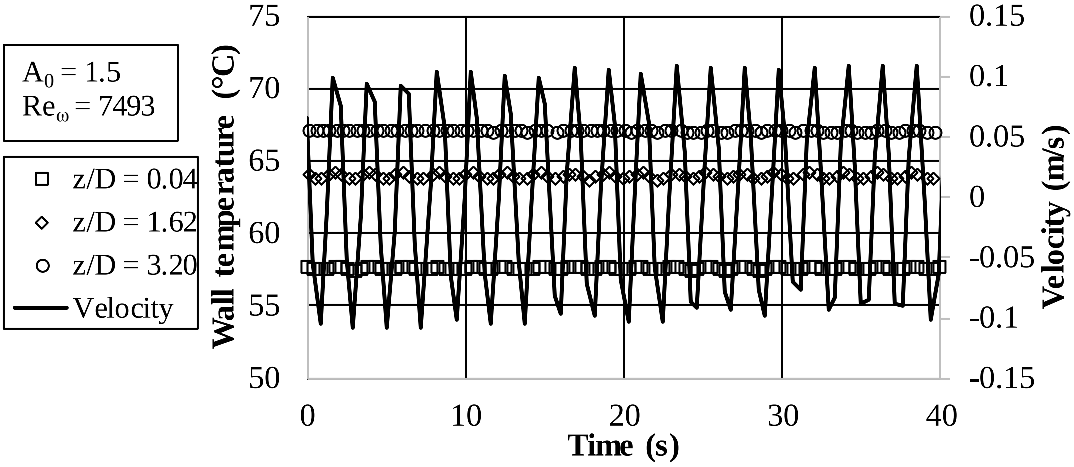

(d)

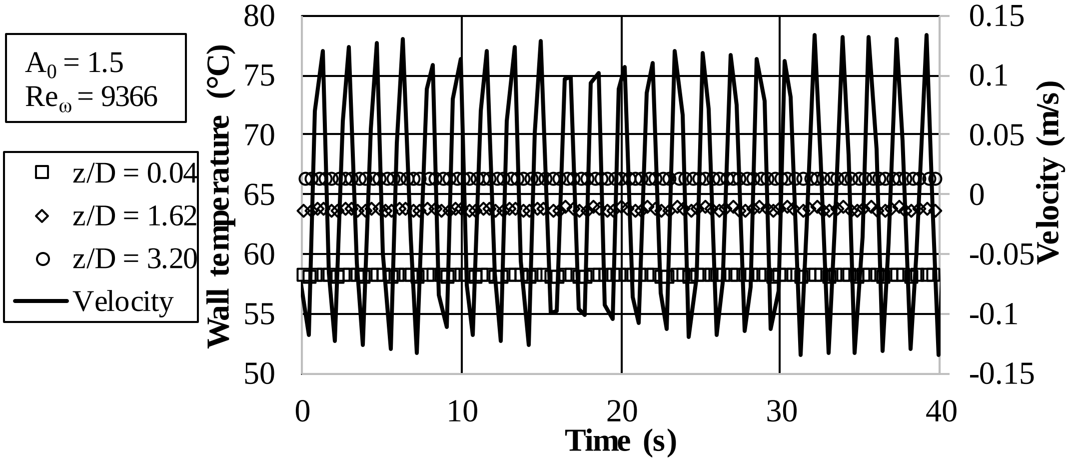

(e)

Figure 4.14 (continued) : Wall temperature and flow velocity as functions of time for fluid displacement A_0= 1.5 for (a) Re$_\omega$= 1873, (b) Re$_\omega$= 3746, (c) Re$_\omega$= 5619, (d) Re$_\omega$=7493 and (e) Re$_\omega$=9366.

Increasing the frequency, at the same displacement, has three effects: a) it lowers the wall temperature at the middle point of the foam pipe, b) it elevates the wall temperature close to the entrance, and c) it generally lowers the amplitude of the wall temperature. These effects combined suggest that increasing the frequency leads to a more uniform and lower wall temperature - attractive attributes for electronics cooling.

As the non-dimensional fluid displacement A_0 increases to 1.9 and 2.2, the same trends are present in the wall temperature, Figure 4.15 and Figure 4.16. However, the wall temperature in all locations along the foam pipe is generally lower, indicating better rates of heat transfer for longer fluid displacements. It should be noted that for the medium displacement A_0= 1.9, no data could be obtained for the highest kinetic Reynolds number Re$_\omega$= 9366 due to safety concerns and limitation of the experimental set-up. Similarly, no data could be obtained for Re$_\omega$= 7493 and 9366 for the highest displacement A_0= 2.2.

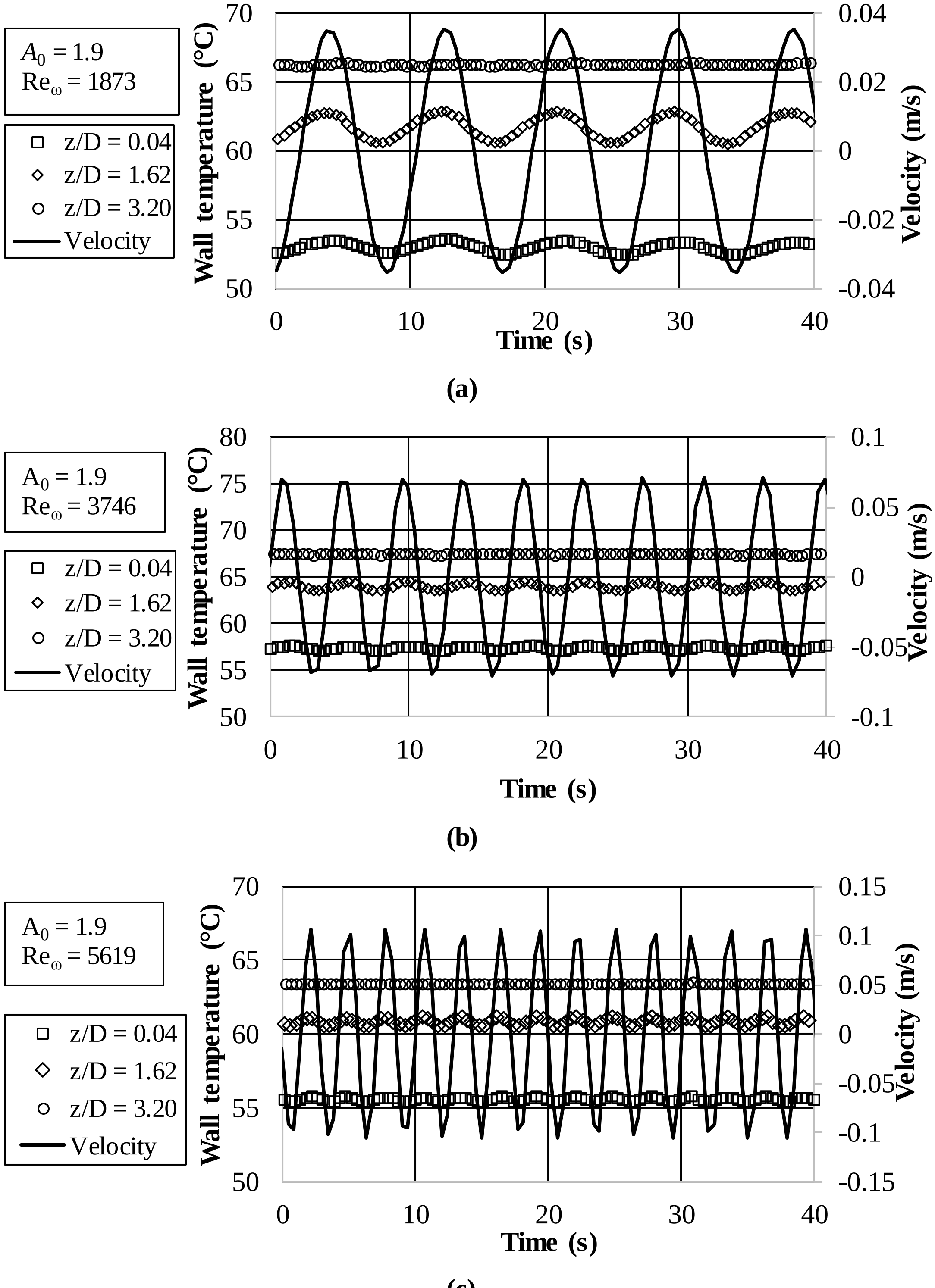

Figure 4.15 : Wall temperature and flow velocity as functions of time for fluid displacement A_0= 1.9 for (a) Re$_\omega$= 1873, (b) Re$_\omega$= 3746, (c) Re$_\omega$= 5619 and (d) Re$_\omega$=7493.

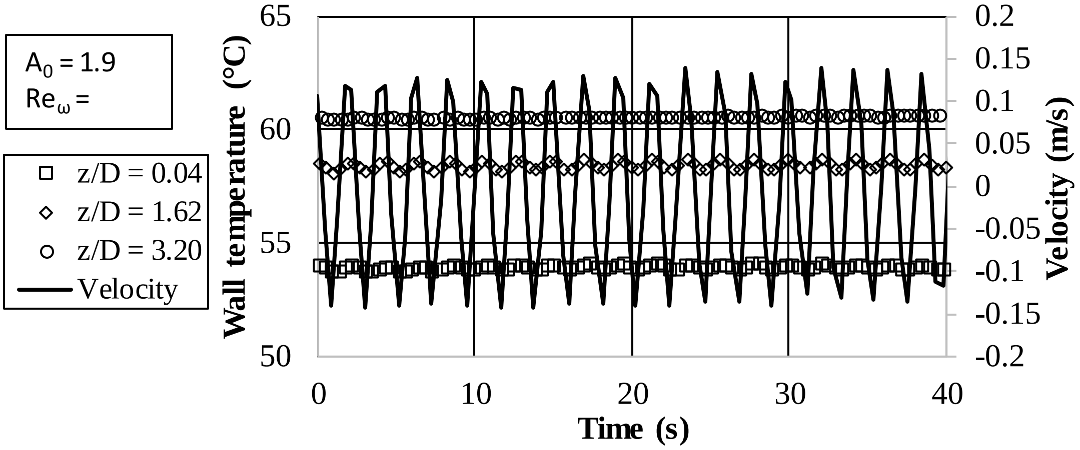

(d)

Figure 4.15 (continued) : Wall temperature and flow velocity as functions of time for fluid displacement A_0= 1.9 for (a) Re_ω= 1873, (b) Re_ω= 3746, (c) Re_ω= 5619 and (d) Re_ω=7493.

Figure 4.17, parts (a) to (c) are plots of the cycle-averaged wall temperature along half of the foam pipe for all frequencies tested at each displacement. Generally, the time-averaged wall temperature gradually increases as the distance from the entrance increases, and it reaches a maximum at the middle of the test section z/D= 3.2. This trend is similar to what occurred in heat transfer due to oscillating water flow in packed spheres[77], oscillating air flow in aluminum foam [79] and [85] and copper foam [86], and in oscillating flow of air in graphite foam [87]. At a given displacement, the wall temperature is seen to decrease as the frequency increases, especially away from the entrance of the foam pipe. As the displacement increases, the average wall temperature decreases. The combination of long displacement, A_0= 2.2, and high frequency, Re_ω = 5619, produces the lowest and most uniform wall temperature, as seen in Figure 4.17 (c). In Figure 4.17 (b), the case for the low frequency (Re_ω= 1873) produces lower wall temperature than the case for the higher frequency (Re_ω= 3746), which is not consistent with the rest of the data: higher frequency reduce wall temperature. This anomaly may be explained by the fact that the experiment for that case was run for a long time during the same day, and as a result the ambient temperature surrounding the test section got hotter, and the rate of heat loss from the test model was reduced.

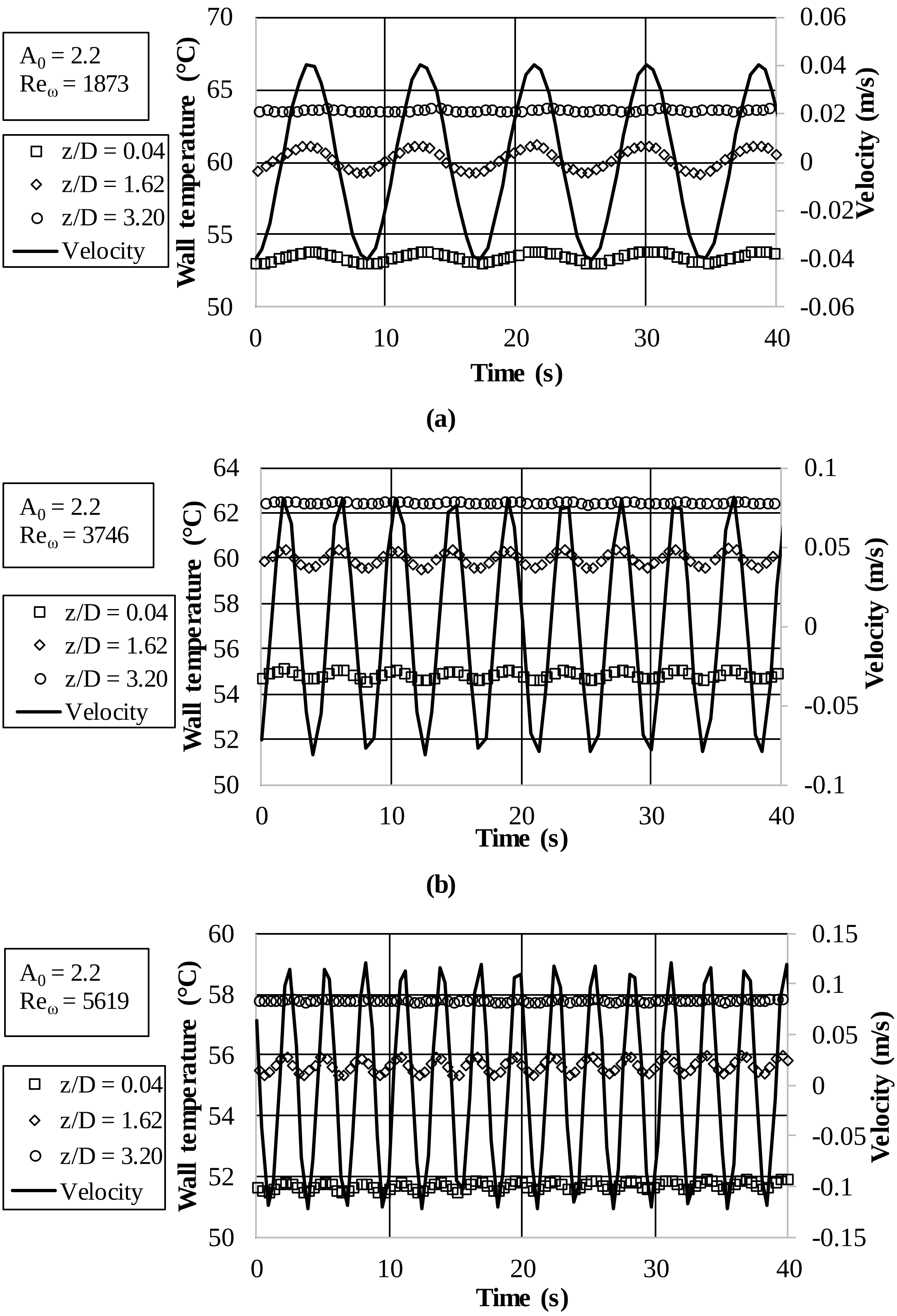

(a)

(b)

(c)

Figure 4.16 : Wall temperature and flow velocity as functions of time for fluid displacement A_0= 2.2 for (a) Re_ω= 1873, (b) Re_ω= 3746 and (c) Re_ω= 5619.

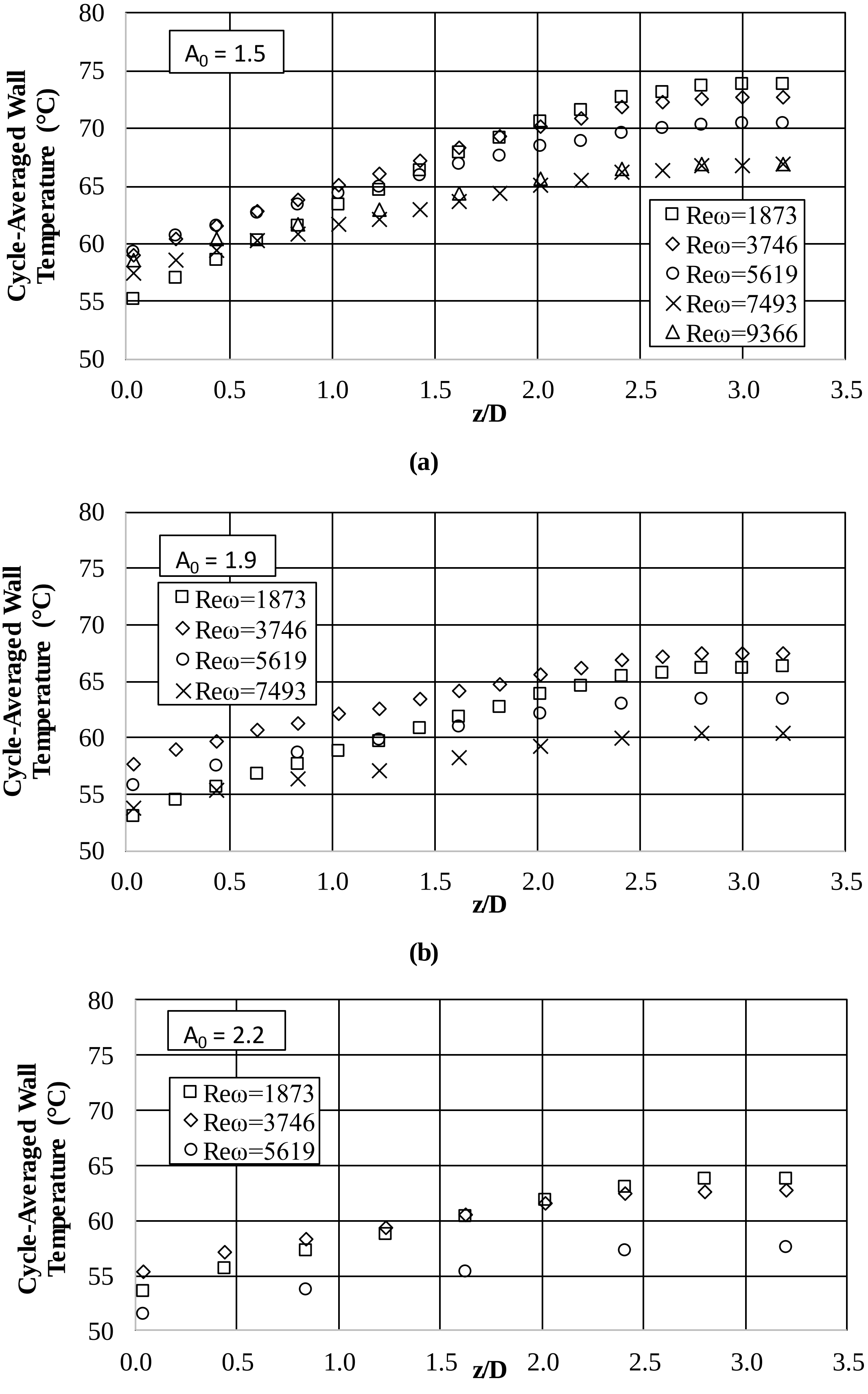

(a)

(b)

(c)

Figure 4.17 : Cycle-averaged wall temperature for (a) $A_0 = 1.5$, (b) $A_0 = 1.9$ and (c) $A_0 = 2.2$.

Leong and Jin [86] and Fu et al. [87] defined the temperature uniformity index *I* as

$$I = \frac{T_{\max} - T_{\min}}{T_{\max}} \tag{4.15}$$

where $T_{\max}$ and $T_{\min}$ are the wall maximum and minimum temperatures in [K], respectively. In order to assess the advantage of oscillating flow over steady flow heat transfer, the temperature uniformity indices for the two cases are compared in Figure 4.18. Reynolds number Re_D is defined as

$$\mathrm{Re}_D = \frac{\rho \tilde{\tilde{U}} D}{\mu} \tag{4.16}$$

where $\tilde{\tilde{U}}$ is the average flow velocity for steady-state flow. For oscillating flow, $\tilde{\tilde{U}}$ is the time-averaged maximum velocity obtained as [87]

$$\tilde{\tilde{U}} = \frac{2u_{\max}}{\pi} \tag{4.17}$$

The temperature uniformity index is generally lower for oscillating flow indicating more uniform wall temperature, as compared to steady state heat transfer. The same trend was present for oscillating air flow in metal foam [86] and [87]. The only exception is the oscillating case for the short displacement $A_0 = 1.5$ and low kinetic Reynolds number $\mathrm{Re}_\omega = 1873$. Uniform surface temperature is sought in electronic cooling for mitigating hot spots and avoiding thermal stresses.

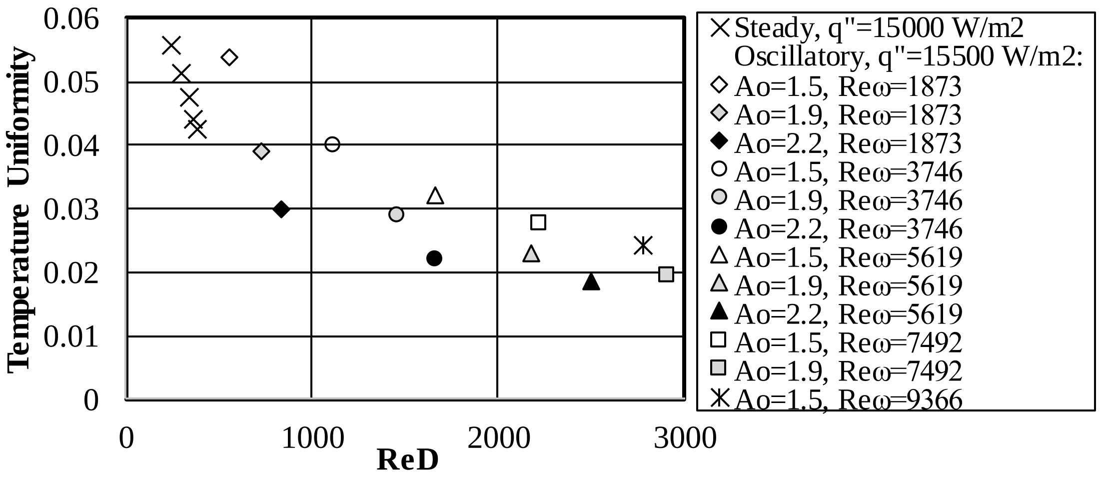

Figure 4.18 : Uniformity index, *I*, for wall temperature for steady and oscillating flow.

For oscillating heat transfer, the local cycle-averaged Nusselt number is defined as [79] and [87]

$$\mathrm{Nu}_z = \frac{q''D}{k_f\left(T_w - T_i\right)} \tag{4.18}$$

where q'' is the heat flux, k_f is the fluid conductivity, T_w is the local wall temperature and T_i is the inlet temperature. It must be noted here that during preliminary unidirectional steady-state runs, an average random heat loss of approximately 8.2% was recorded by applying an overall energy balance to the test section. This loss was subtracted from the supplied heat flux when calculating Nusselt number. The cycle-averaged local Nusselt number decays gradually as the distance from the entrance increases, as shown in Figure 4.19. It reaches a minimum at the middle point of the foam pipe. These trends are valid for all fluid displacements (parts (a), (b) and (c) of Figure 4.19) and for all frequencies at a given displacement. The effect of frequency is seen to be more severe for long displacement, Figure 4.19 (c). The highest Nusselt number is realized at the longest displacement and highest frequency, which is consistent with observations made earlier. There is no appreciable difference in Nu_z for $\mathrm{Re}_\omega = 7493$ and 9366 for $A_0 = 1.5$, Figure 4.19 (a); similarly, there is no significant difference in Nu_z for $\mathrm{Re}_\omega = 1873$ and 3746 for $A_0 = 2.2$, Figure 4.19 (c).

The general behavior of Nu_z is similar to that of oscillating air flow in aluminum, copper and graphite foam [79,85-87]. For oscillating water flow in packed steel spheres (1 and 3 mm), Pamuk and Özdemir [77] showed that the cycle-averaged Nusselt number increased along the porous medium for long displacements, and it decreased for short fluid displacements. These trends may be attributed to the large difference in porosity between the foam (87.6%) and packed spheres (35.0% and 35.6%). Another difference is in the thermal conductivity between aluminum foam and steel packed spheres. This is in addition to the obvious difference in internal topology of the two porous media and in surface area per unit volume, which plays a critical role in flow and heat transfer.

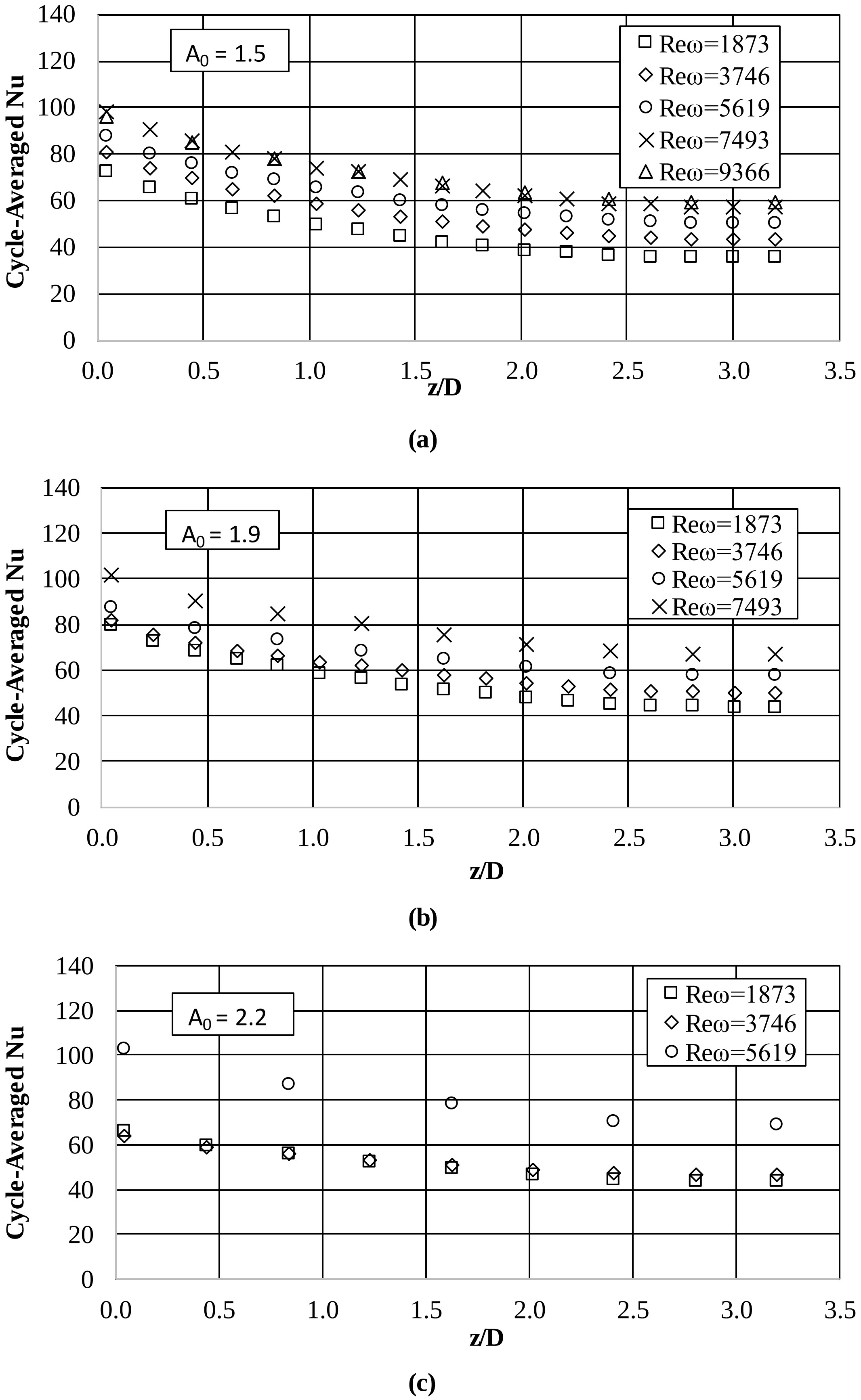

Figure 4.19 : Cycle-averaged Nusselt number for (a) A_0 = 1.5, (b) A_0 = 1.9 and (c) A_0 = 2.2.

A meaningful comparison can be made with the results of Leong and Jin [85] who studied heat transfer in 20-ppi aluminum foam due to oscillating air flow. In Figure 4.20, the length-averaged Nusselt number for oscillating air flow is higher than that for oscillating water flow in the same kind of foam. This is opposite to what is expected, and can be explained by the following differences between [85] and the current study: first, the foam rectangular channel of [85] was heated on one side only (heat-sink arrangement), second, the non-dimensional displacement A_0 employed in [85] was 4.08 (calculated based on the hydraulic diameter of their channel), while the maximum A_0 for the current study was only 2.2, and third, the height of the channel of [85] was only 10 mm or only 4 foam cells, approximately. This indicates that there might have been considerable size effects in the results of [85]. For size effects in metal foam, see [26] and [111].

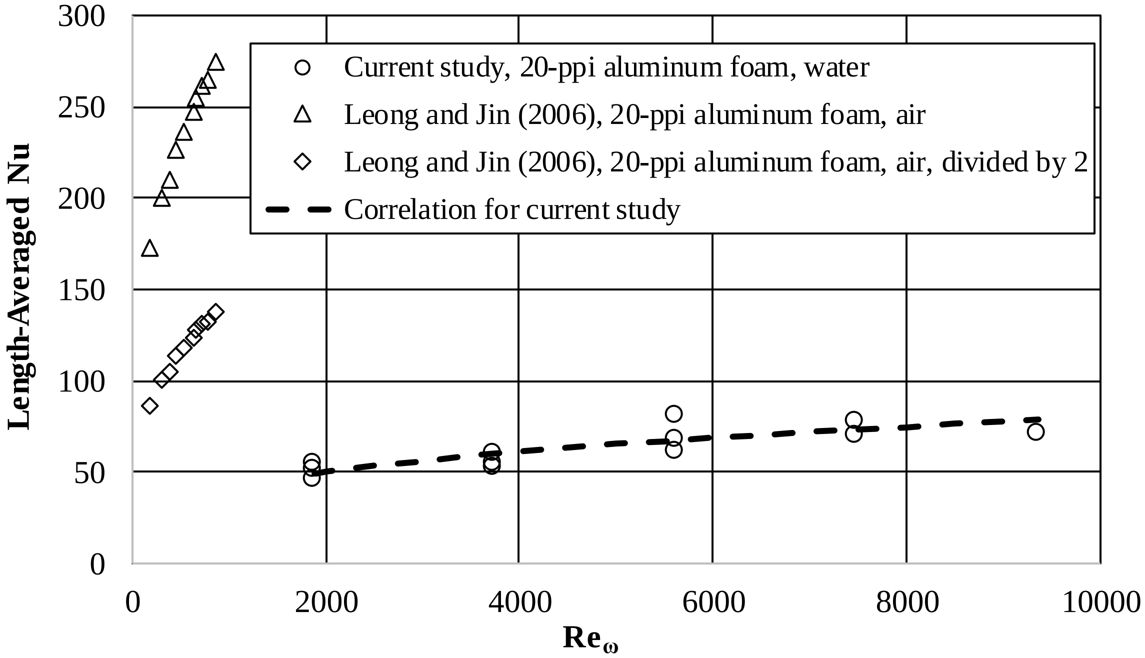

Figure 4.20 : Length-averaged Nusselt number for oscillating water flow (current study) and for oscillating water flow Leong and Jin [85].

To bridge the gap between the current study and [85], Nu of [85] is divided by two (because it was heated on one side only) and plotted in Fig. 10. This was done to compensate for the fact that in [85] only one side was heated. Nu for oscillating air flow in the same kind of metal foam [85] is still higher than Nu for oscillating water flow of the current study, even though the flow frequency of the current study is considerably higher. This comparison suggests rather strongly that the flow displacement has a profound effect on oscillating heat transfer in metal foam. This can be exploited by using long flow displacements at relatively lower frequencies to achieve high heat transfer rates, which is advantageous in terms of low noise and low vibrations.

The length averaged Nusselt number obtained experimentally in the current study correlates well the kinetic Reynolds number according to

$$\mathrm{Nu} = 4.19 A_0^{0.37}\,\mathrm{Re}_\omega^{0.29} \tag{4.19}$$

Equation (4.19) predicts the experimental data rather well. The relative, absolute and standard deviations were found to be 0.57%, 5.28%, 8.31%, respectively. This form of the correlation is similar in form to one obtained by Leong and Jin [79] for oscillating air flow in 40-ppi aluminum foam. The exponents of Re_ω obtained here (0.29) and 0.31 obtained by Leong and Jin [79] are comparable. For oscillating water flow in packed spheres, Pamuk and Özdemir [77] obtained 0.34 as an average exponent for Re_ω, which is also similar to what was obtained in Equation (4.19). This points to the possibility of a universal (mild) dependence of average Nusselt number on kinetic Reynolds number for oscillating heat transfer in porous media. The exponent of the flow displacement and the multiplier of Equation (4.19) are different from those of [77] and [79].

A comparison between steady-state and oscillating heat transfer in the same metal foam of the current study is presented in Figure 4.21. The length and time averaged Nusselt number, defined by Equation (4.18), is plotted against Reynolds number defined by Equation (4.16). Counter what is typically believed, the steady-state flow clearly produces more heat transfer compared to oscillating flow. A careful look into this issue reveals that heat transfer, or Nusselt number, indeed depends not only on the nature of flow (steady or oscillating), but also on other critical variables, i.e. flow displacement relative to length of porous medium, how and where the heat is removed in a closed oscillating flow system and, and to a lesser degree, on the range of flow frequency (kinetic Reynolds number).

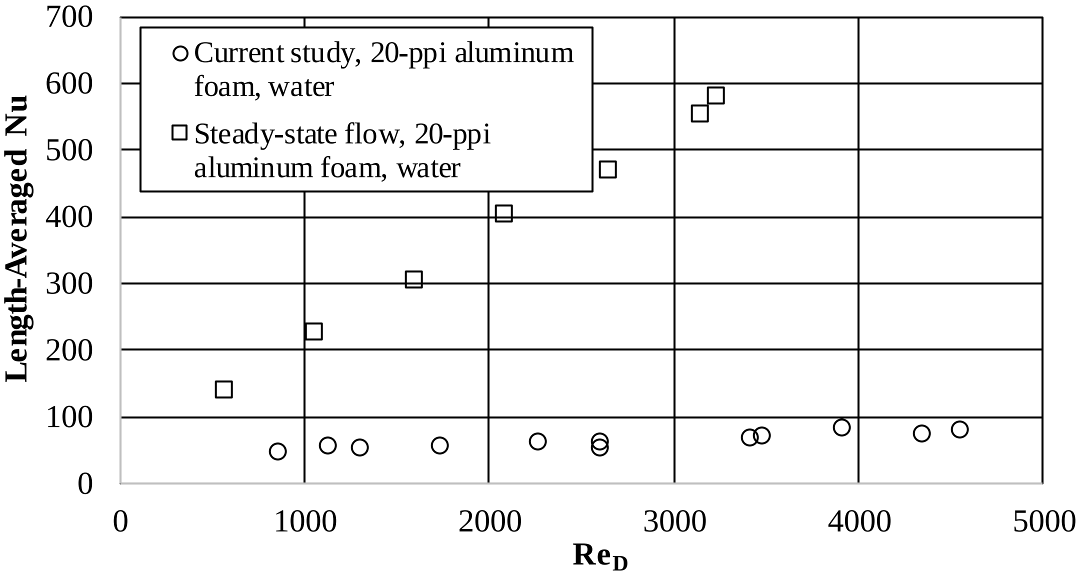

Figure 4.21 : Length-averaged Nusselt number for oscillating and steady-state water flow.

If the flow displacement is short, as in the current study, steady flow may well produce higher heat transfer. If, on the other hand, the flow displacement is long, as in [87], oscillating flow may produce higher rates of heat transfer. The location and manner in which the heat is removed from oscillating flow (closed) set-up dictates the inlet fluid temperature to the porous medium. This temperature can drastically change the value of the Nusselt number as defined in Equation (4.18). Therefore care should be taken when designing oscillating flow heat transfer systems in order to ensure more heat is removed and to avoid complication and energy waste.

4.3 Comparison with Numerical Results and Discussion

4.3.1 Steady-state flow

As stated in Section 2.2, the pressure gradient results of the simulations for steady-state flow were in good agreement with those of the experimental runs. The heat transfer results of the model, the details of which were given in Section 2.3.1, on the other hand, need to be discussed per regime as the computational model exhibited a diverging behavior at high velocities.

As listed in Table 2.3, models with different boundary conditions, namely inlet velocities and heat fluxes through the wall, were simulated for Darcy, transition and Forchheimer regimes. The mesh was the same in all of the runs.

For the experimental heat transfer part, the bulk temperatures along the foam were found by taking into consideration the fully developed region. However, the bulk temperature for the computational runs were found easily by post-processing the 3-dimensional data of the cylindrical porous domain, employing Equation (4.5). As will be seen in the following figures below, the bulk temperatures were well predicted.

Figure 4.22 (a) shows a mismatch in the thermally developing region for a run in the Darcy regime, with a superficial velocity of 0.00668 m/s. As distance from the entrance grows, the computational wall temperature curve converges to the experimental result. Figure 4.22 (b) clearly shows that the porous media model of Fluent is incapable of capturing the thermal entry region behavior. However, in the fully developed zone, there seems to be a 13% difference which is in the uncertainty range of Nusselt number previously found.

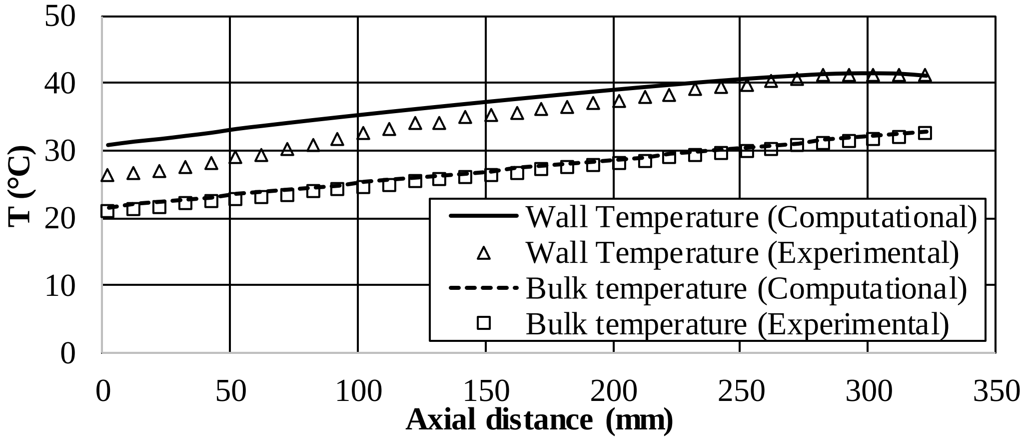

(a)

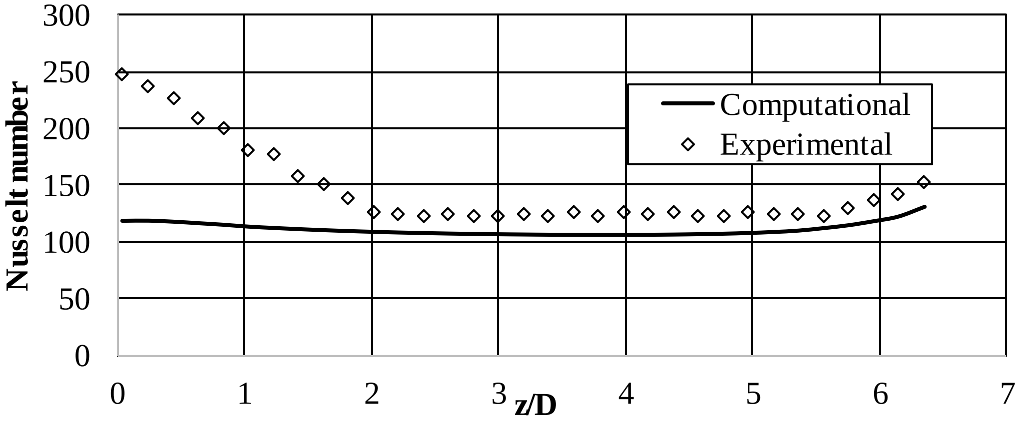

(b)

Figure 4.22 : Comparison of computational and experimental heat transfer results in Darcy region: (a) Wall temperature and bulk temperature distribution along the foam, (b) Nusselt number distribution along dimensionless distance *z/D*.

Because there is no viable approach for heat transfer in transition zone, a method similar to that for determining the hydrodynamic entry was employed. For the pressure gradient source terms for the two sets of flow runs, coefficients from Darcy and Forchheimer regimes were invoked separately. Unlike the hydrodynamic analysis, no significant deviation of results from each other was detected. The average percent difference between the wall temperatures was 0.2 %. It was negligibly lower for the bulk temperatures.

The differences between the computational and the experimental results, on the other hand, were higher than that for the Darcy regime. Figure 4.23 (a) and (b) show the computational results to their experimental counterparts for the Darcy velocity of 0.0099 m/s. The bulk temperatures were found almost the same for the two types of studies. However, the computationally-found wall temperatures were found to be 10.8 % higher than the experimentally-found values, even in the fully-developed region, where the Darcy regime exhibited a good agreement. Nusselt number distribution also varied significantly, with a percentage of 29.3 %.

The accuracy of the built-in porous media heat transfer model was lower for velocities in Forchheimer regime. Figure 4.24 (a) and (b) show the comparisons for temperature and Nusselt number distributions for the superficial velocity of 0.0596 m/s. The differences were drastically high for this regime. The differences between numerical and experimental results for wall temperatures and Nusselt numbers were 40.7 % and 60.0 %, respectively. These results can be either caused by the fact that the porous media model for Fluent was actually produced for traditional media such as granular packed beds with low porosities, or the fact that at high temperatures, it is harder to observe the thermally-developed region. Nevertheless, these aspects of the outcomes of this model caused loss of confidence in its use for oscillating heat transfer due to the inherent velocities.

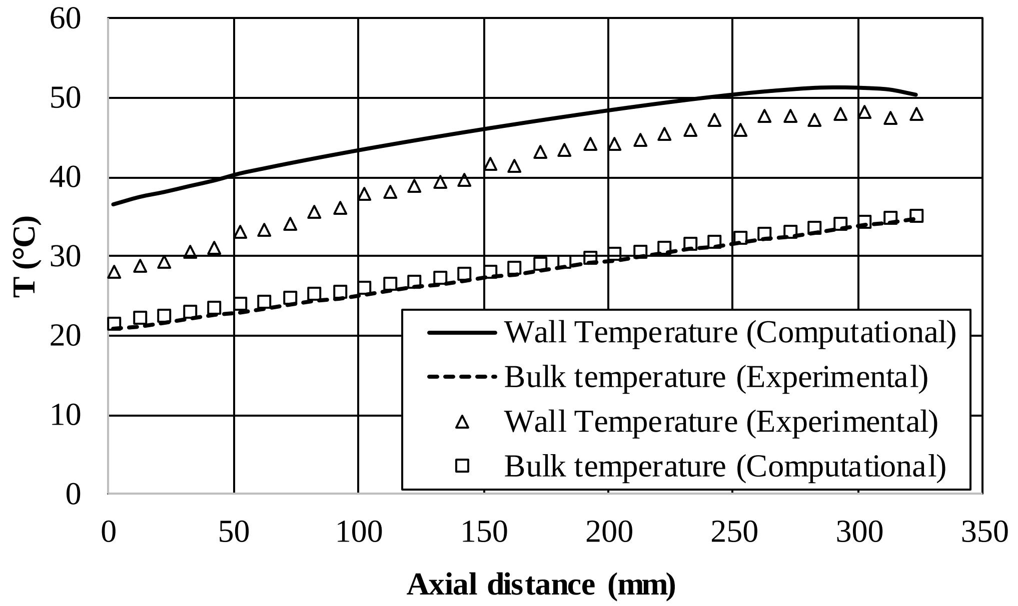

(a)

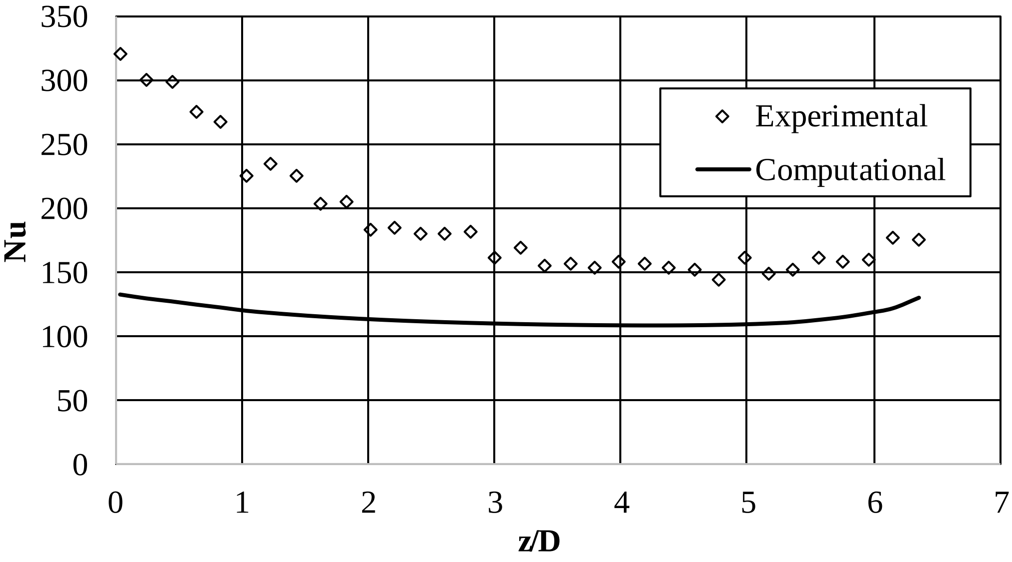

(b)

Figure 4.23 : Comparison of computational and experimental heat transfer results in the transition region from Darcy to Forchheimer: (a) Wall temperature and bulk temperature distribution along the foam, (b) Nusselt number distribution along dimensionless distance *z*/*D*.

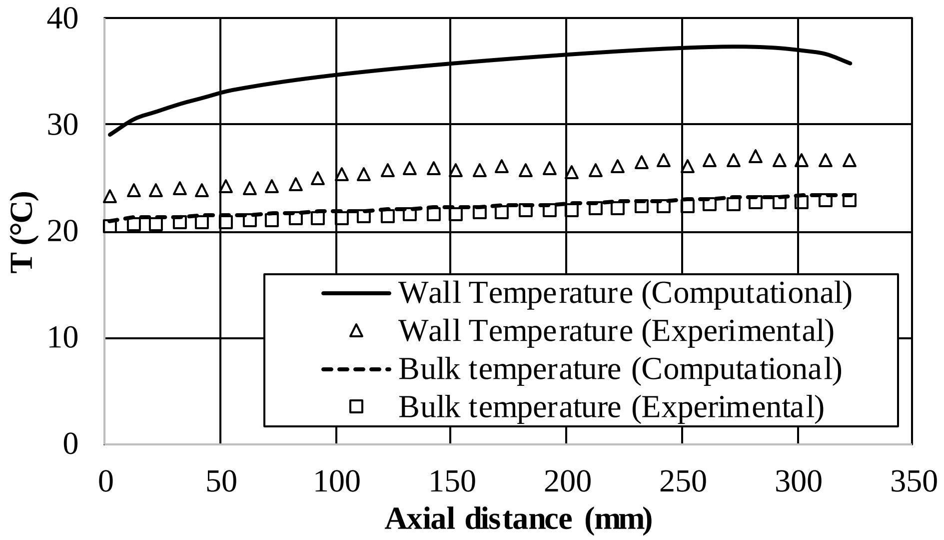

(a)

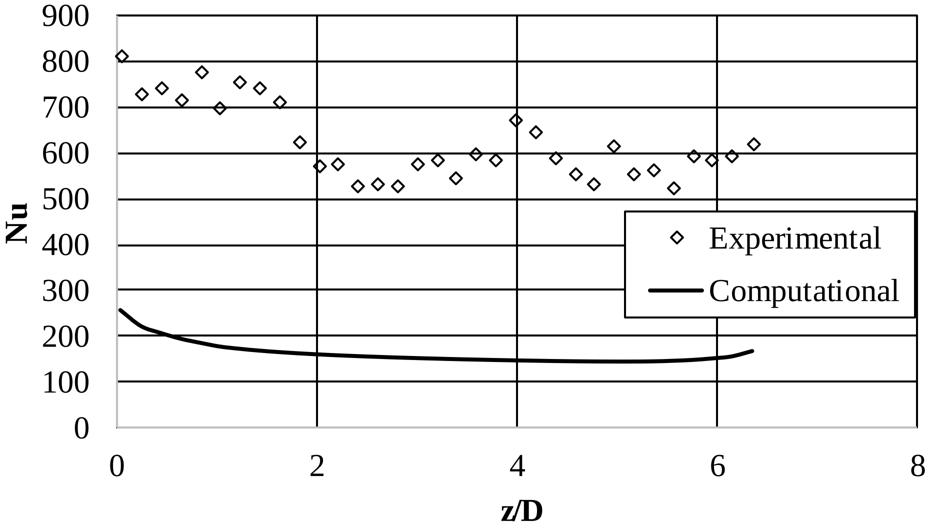

(b)

Figure 4.24 : Comparison of computational and experimental heat transfer results in the Forchheimer regime: (a) Wall temperature and bulk temperature distribution along the foam, (b) Nusselt number distribution along dimensionless distance *z*/*D*.

4.3.2 Oscillating flow

The reciprocating flow was introduced to the domain by attributing counteracting axial velocities to the both end surfaces where they were uniformly distributed, and transient in a sinusoidal manner. Equation (3.16) was entered as a velocity-inlet boundary condition for one end by compiling a user-defined function. As for the other end, the same function with a negative sign was presented to the domain likewise. Because the velocity was introduced uniformly rather than with a fully-developed-flow distribution, the steel pipe zone was left extending to its original length to allow the flow become developed in the vicinity of the test section.

Short stroke and the lowest frequency corresponding to 74.35 mm and 0.116 Hz, respectively, was selected as the oscillatory flow case for the simulation. Figure 4.25 shows that the computational and experimental results for oscillating flow in metal foam are in good agreement with each other.

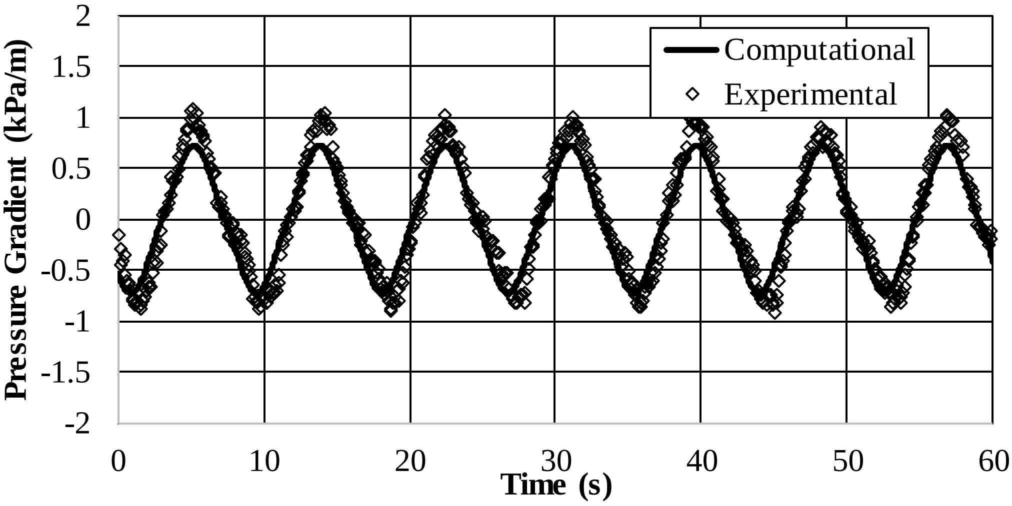

Figure 4.25 : Comparison of the experimental and computational pressure drop data for oscillating flow.

Figure 4.26 shows the wall temperatures versus time for points in the middle of the tube and on one end. There is an error in computational results about 16% with respect to the experimental counterparts. With the reasons reported previously, it can be said that the macro model is not applicable for transient heat transfer in metal foam.

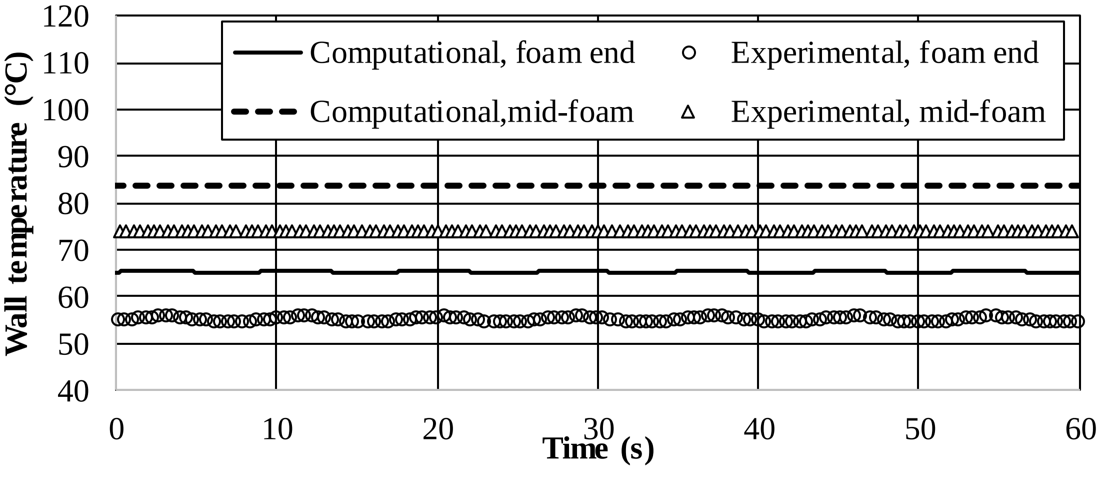

Figure 4.26 : Comparison of the experimental and computational wall temperature data at the end and midpoint of the foam for oscillating heat transfer.

5. CONCLUSIONS

Experimental qualification study of water flow in two distinct porous media composed of spheres of 1- and 3-mm diameter were conducted and presented as a preliminary work for experimental research on metal foam. Various flow regimes were identified, along with transitional regimes in between them. The same porous medium was seen to exhibit different values of permeability and Forchheimer coefficient in different flow regimes. When possible, flow regimes demarcation was contrasted to others in the literature. Several differences were found.

Using the square root of the Darcy-regime permeability as a length scale (in Reynolds number and friction factor), was seen to correlate the pressure-drop data very well, including the pre-Darcy-regime data. Beyond the pre-Darcy regime, the friction factors for the two packed beds were practically the same. The experimental data clearly indicated that friction factor was a linear function of the reciprocal of the Reynolds number in all regimes.

The coefficients of the Ergun relation were determined. A exhibited some variations with diameter and was higher for turbulent flow, while B exhibited some variations with diameter and decreased for turbulent flow. As for the Carman–Kozeny constant, the current investigation generally produced lower values for this constant.

In addition, recent theoretical development regarding the range of applicability of the quadratic and cubic corrections in strong and weak inertia regimes was checked and was shown to be in disagreement with what was exhibited by the experiment results.

After the qualification study, pressure-drop results for steady-state water flow in metal foam were presented. Virtually all known flow regimes (from pre-Darcy to turbulent) were identified, along with transitions from one to another.

The following statements can be made:

- The Darcy regime was rather narrow, while the Forchheimer regime was relatively wide.
- Transition from Forchheimer to turbulent regime was smooth.

- The same metal foam exhibited different values of permeability and Forchheimer coefficient in different post-Darcy flow regimes as well as 1- and 3-mm packed spheres.
- Using the square root of the permeability, measured in the Darcy regime, as a characteristic length for defining Reynolds number and friction factor correlated the pressure-drop data extremely well, including the pre-Darcy regime as was the case for the packed beds.
- When possible, flow regime demarcations for metal foam were contrasted to others in the literature. Severe differences were found and possible reasons were stated.
- The fully turbulent regime was identified by the friction factor becoming constant and independent of Reynolds number.

As for study on transient flow through metal foam, characteristics of oscillating water flow were experimentally acquired and presented for three flow displacements and several frequencies. The following statements can be made:

- The pressure drop increases with both flow displacement and frequency, with the increase being more pronounced for high frequencies.
- There was a phase shift between the inlet and outlet pressures and flow velocity, with this shift being a function of frequency.
- The functional relationship between the friction factor and Reynolds number for oscillating flow in porous media was applicable to the result of the current study for water flow in metal foam, and was consistent with other studies for air and water flows in various porous media.
- The results of the current study suggested the existence of two regimes based on frequency.

When compared to other studies, the following was found for oscillating flow in metal foam:

- The friction factor for the case of oscillating water flow in metal foam was about ten times higher than that for air flow.

- The friction factor for oscillating water flow in packed spheres was more than ten times higher than that for flow in high-porosity metal foam.
- The friction factor for oscillating air flow in woven screens was higher than the friction factor for oscillating water flow in metal foam.

For steady-state water flow in an aluminum tube internally brazed to metal foam, thus with low thermal contact resistance, and subjected to constant heat flux, the wall temperature and average inlet and outlet temperatures were measured. Flow rates were in the Darcy, transitional and Forchheimer regimes. A thermal entrance region and a thermally fully-developed region were identified. An exit region was observed, as well. The thermal entry length was determined and was seen to be significant. It was higher for higher flow velocities. In the Darcy regime, the thermal entry length was much higher than predicted by analysis in porous media with thermal equilibrium between the solid and fluid phases. As such, the thermal entry region in metal foam should not be causally ignored. For non-Darcy regimes, previously unknown heat transfer phenomenon was observed: a seemingly periodic behavior of Nusselt number along the foam. The bulk fluid temperature was estimated and the local Nusselt number was calculated. For the thermally-fully developed cases of the Darcy regime, Nusselt number compared well with analytical predictions employing local thermal equilibrium and local thermal non-equilibrium assumptions. However, the analytical solution with the local thermal equilibrium assumption seemed to over-predict the Nusselt number. The analytical solution for local thermal non-equilibrium matched the experimental data extremely well (within a maximum difference of 4.6%). This indicates that the assumption of local thermal non-equilibrium is more appropriate for convection in metal foam with water flow. In the thermally-fully-developed region of the non-Darcy regime, Nusselt number correlated well with the Reynolds number in a power law.

Heat transfer results and instantaneous velocity of oscillating water flow in metal foam were experimentally obtained for three flow displacements and a range of frequencies. For the frequencies encountered in this study, the wall temperature was in phase with flow velocity. Higher fluid displacements and higher frequencies generally lowered the wall temperature and caused more uniformity in the wall temperature. The cycle- and length-averaged Nusselt number correlated well with the non-dimensional flow displacement and kinetic Reynolds number in a power law. Upon comparison to other studies, it seemed possible that the dependence of average Nusselt number on kinetic Reynolds number might be universal for oscillating heat transfer in porous media.

The current range of flow displacement and frequency produced lower heat transfer as compared to a previous study employing oscillating air flow in similar metal foam, but with significantly longer flow displacements. This suggests that flow displacement plays a dominant role in oscillating heat transfer. Based on a comparison between oscillating and steady-state heat transfer in the same foam, it was found that steady-state flow may produce higher heat transfer rates than certain oscillating flows employing short flow displacements and low frequencies.

Computational results of the model for steady-state water flow through open-cell metal foam were presented. The model seemed to return accurate values of pressure-velocity couples. Entry and exit lengths were observable along the flow axis. Because there is a gap in interpreting the hydrodynamic behavior in transition regime, coefficients from neighboring regimes had to be used to approximate the entry and exit lengths therein.

The oscillating flow and heat transfer were also modeled. The flow results matched the experimental values well. However, there was a significant mismatch of heat transfer results, exceeding the experimental uncertainty. This was a result of employing the built-in porous media model and inadequate mixing due to the current turbulence model in the numerical tools.

For further research on flow of water and heat transfer metal foam, following recommendations can be listed:

- Metal foams with exactly same bulk geometries and similar porosities but different pore densities can be studied under the same flow conditions.
- Stroke length can be increased so that the volumetric flow displacement can be equal to the void volume of the metal foam.
- Models in micro scales can be prepared and used in simulations for comparable and more detailed results.

REFERENCES

[1] **Dukhan, N.** (2013). *Metal Foams: Fundamentals and Applications*: Destech Publications.

[2] **Antohe, B. V., Lage, J. L., Price, D. C., & Weber, R. M.** (1997). Experimental Determination of Permeability and Inertia Coefficients of Mechanically Compressed Aluminum Porous Matrices. *Journal of Fluids Engineering, 119*(2), 404-412.

[3] **Tadrist, L., Miscevic, M., Rahli, O., & Topin, F.** (2004). About the use of fibrous materials in compact heat exchangers. *Experimental Thermal and Fluid Science, 28*(2–3), 193-199.

[4] **Boomsma, K., Poulikakos, D., & Zwick, F.** (2003). Metal foams as compact high performance heat exchangers. *Mechanics of Materials, 35*(12), 1161-1176.

[5] **Mahjoob, S., & Vafai, K.** (2008). A synthesis of fluid and thermal transport models for metal foam heat exchangers. *International Journal of Heat and Mass Transfer, 51*(15–16), 3701-3711.

[6] **Ergun, S.** (1952). Fluid flow through packed columns. *Chemical Engineering Progress, 48,* 89.

[7] **Dybbs, A., & Edwards, R. V.** (1984). A New Look at Porous Media Fluid Mechanics — Darcy to Turbulent. In J. Bear & M. Y. Corapcioglu (Eds.), *Fundamentals of Transport Phenomena in Porous Media* (Vol. 82, pp. 199-256): Springer Netherlands.

[8] **Fand, R. M., Kim, B. Y. K., Lam, A. C. C., & Phan, R. T.** (1987). Resistance to the Flow of Fluids Through Simple and Complex Porous Media Whose Matrices Are Composed of Randomly Packed Spheres. *Journal of Fluids Engineering, 109*(3), 268-273.

[9] **Kececioglu, I., & Jiang, Y.** (1994). Flow Through Porous Media of Packed Spheres Saturated With Water. *Journal of Fluids Engineering, 116*(1), 164-170.

[10] **Rode, S., Midoux, N., Latifi, M. A., Storck, A., & Saatdjian, E.** (1994). Hydrodynamics of liquid flow in packed beds: an experimental study using electrochemical shear rate sensors. *Chemical Engineering Science, 49*(6), 889-900.

[11] **Seguin, D., Montillet, A., & Comiti, J.** (1998). Experimental characterisation of flow regimes in various porous media—I: Limit of laminar flow regime. *Chemical Engineering Science, 53*(21), 3751-3761.

[12] **Seguin, D., Montillet, A., Comiti, J., & Huet, F.** (1998). Experimental characterization of flow regimes in various porous media—II: Transition to turbulent regime. *Chemical Engineering Science, 53*(22), 3897-3909.

[13] **Bear, J.** (1972). *Dynamics of Fluids in Porous Media*: Dovers, New York.

[14] **Dukhan, N., Bağcı, Ö., & Özdemir, M.** (2014). Experimental flow in various porous media and reconciliation of Forchheimer and Ergun relations. *Experimental Thermal and Fluid Science, 57,* 425-433.

[15] **Beavers, G. S., & Sparrow, E. M.** (1969). Non-Darcy Flow Through Fibrous Porous Media. *Journal of Applied Mechanics, 36*(4), 711-714.

[16] **Montillet, A., Comiti, J., & Legrand, J.** (1992). Determination of structural parameters of metallic foams from permeametry measurements. *Journal of Materials Science, 27*(16), 4460-4464.

[17] **Edouard, D., Lacroix, M., Huu, C. P., & Luck, F.** (2008). Pressure drop modeling on SOLID foam: State-of-the art correlation. *Chemical Engineering Journal, 144*(2), 299-311.

[18] **Mancin, S., Zilio, C., Cavallini, A., & Rossetto, L.** (2010). Pressure drop during air flow in aluminum foams. *International Journal of Heat and Mass Transfer, 53*(15–16), 3121-3130.

[19] **Kim, S. Y., Paek, J. W., & Kang, B. H.** (2000). Flow and Heat Transfer Correlations for Porous Fin in a Plate-Fin Heat Exchanger. *Journal of heat transfer, 122*(3), 572-578.

[20] **Bhattacharya, A., Calmidi, V. V., & Mahajan, R. L.** (2002). Thermophysical properties of high porosity metal foams. *International Journal of Heat and Mass Transfer, 45*(5), 1017-1031.

[21] **Boomsma, K., Poulikakos, D., & Ventikos, Y.** (2003). Simulations of flow through open cell metal foams using an idealized periodic cell structure. *International Journal of Heat and Fluid Flow, 24*(6), 825-834.

[22] **Boomsma, K., & Poulikakos, D.** (2001). The Effects of Compression and Pore Size Variations on the Liquid Flow Characteristics in Metal Foams. *Journal of Fluids Engineering, 124*(1), 263-272.

[23] **Hwang, J. J., Hwang, G. J., Yeh, R. H., & Chao, C. H.** (2001). Measurement of Interstitial Convective Heat Transfer and Frictional Drag for Flow Across Metal Foams. *Journal of heat transfer, 124*(1), 120-129.

[24] **Dukhan, N., & Patel, K.** (2011). Effect of sample's length on flow properties of open-cell metal foam and pressure-drop correlations. *Journal of Porous Materials, 18*(6), 655-665.

[25] **Zhong, W., Li, X., Liu, F., Tao, G., Lu, B., & Kagawa, T.** (2014). Measurement and Correlation of Pressure Drop Characteristics for Air Flow Through Sintered Metal Porous Media. *Transport in Porous Media, 101*(1), 53-67.

[26] **Dukhan, N., & Ali, M.** (2012). Strong wall and transverse size effects on pressure drop of flow through open-cell metal foam. *International Journal of Thermal Sciences, 57*(0), 85-91.

[27] **Dukhan, N., & Minjeur, C., II**. (2011). A two-permeability approach for assessing flow properties in metal foam. *Journal of Porous Materials, 18*(4), 417-424.

[28] **Bonnet, J.-P., Topin, F., & Tadrist, L.** (2008). Flow Laws in Metal Foams: Compressibility and Pore Size Effects. *Transport in Porous Media, 73*(2), 233-254.

[29] **Liu, J. F., Wu, W. T., Chiu, W. C., & Hsieh, W. H.** (2006). Measurement and correlation of friction characteristic of flow through foam matrixes. *Experimental Thermal and Fluid Science, 30*(4), 329-336.

[30] **Dukhan, N., & Ali, M.** (2012). On the various flow regimes in open-cell metal foam. *International Journal of Transport Phenomena, 3*, 85-97.

[31] **Skjetne, E., & Auriault, J.-L.** (1999). High-Velocity Laminar and Turbulent Flow in Porous Media. *Transport in Porous Media, 36*(2), 131-147.

[32] **Calmidi, V. V., & Mahajan, R. L.** (2000). Forced Convection in High Porosity Metal Foams. *Journal of heat transfer, 122*(3), 557-565.

[33] **Angirasa, D.** (2002). Forced Convective Heat Transfer in Metallic Fibrous Materials. *Journal of heat transfer, 124*(4), 739-745.

[34] **Lu, W., Zhao, C. Y., & Tassou, S. A.** (2006). Thermal analysis on metal-foam filled heat exchangers. Part I: Metal-foam filled pipes. *International Journal of Heat and Mass Transfer, 49*(15–16), 2751-2761.

[35] **Zhao, C. Y.** (2012). Review on thermal transport in high porosity cellular metal foams with open cells. *International Journal of Heat and Mass Transfer, 55*(13–14), 3618-3632.

[36] **Xu, H. J., Qu, Z. G., & Tao, W. Q.** (2011). Analytical solution of forced convective heat transfer in tubes partially filled with metallic foam using the two-equation model. *International Journal of Heat and Mass Transfer, 54*(17–18), 3846-3855.

[37] **Qu, Z. G., Xu, H. J., & Tao, W. Q.** (2012). Fully developed forced convective heat transfer in an annulus partially filled with metallic foams: An analytical solution. *International Journal of Heat and Mass Transfer, 55*(25–26), 7508-7519.

[38] **Xu, H. J., Qu, Z. G., & Tao, W. Q.** (2011). Thermal transport analysis in parallel-plate channel filled with open-celled metallic foams. *International Communications in Heat and Mass Transfer, 38*(7), 868-873.

[39] **Odabaee, M., Mancin, S., & Hooman, K.** (2013). Metal foam heat exchangers for thermal management of fuel cell systems – An experimental study. *Experimental Thermal and Fluid Science, 51*(0), 214-219.

[40] **Fiedler, T., White, N., Dahari, M., & Hooman, K.** (2014). On the electrical and thermal contact resistance of metal foam. *International Journal of Heat and Mass Transfer, 72*(0), 565-571.

[41] **Dukhan, N., Bağcı, Ö., & Özdemir, M.** (2015). Thermal development in open-cell metal foam: An experiment with constant wall heat flux. *International Journal of Heat and Mass Transfer, 85*, 852-859.

[42] **Khashehchi, M., Ashtiani Abdi, I., Hooman, K., & Roesgen, T.** (2014). A comparison between the wake behind finned and foamed circular cylinders in cross-flow. *Experimental Thermal and Fluid Science, 52*(0), 328-338.

[43] **Chumpia, A., & Hooman, K.** (2014). Performance evaluation of single tubular aluminium foam heat exchangers. *Applied Thermal Engineering, 66*(1–2), 266-273.

[44] **Noh, J.-S., Lee, K. B., & Lee, C. G.** (2006). Pressure loss and forced convective heat transfer in an annulus filled with aluminum foam. *International Communications in Heat and Mass Transfer, 33*(4), 434-444.

[45] **Poulikakos, D., & Renken, K.** (1987). Forced Convection in a Channel Filled With Porous Medium, Including the Effects of Flow Inertia, Variable Porosity, and Brinkman Friction. *Journal of heat transfer, 109*(4), 880-888.

[46] **Xiong, M.** (2003). Thermally Developing Forced Convection in a Porous Medium: Parallel-Plate Channel or Circular Tube with Walls at Constant Heat Flux. *6*(3), 10.

[47] **Nield, D. A., Kuznetsov, A. V., & Xiong, M.** (2004). Thermally developing forced convection in a porous medium: Parallel-plate channel or circular tube with isothermal walls. *Journal of Porous Media, 7*(1), 19-27.

[48] **Nield, D. A., Kuznetsov, A. V., & Xiong, M.** (2003). Thermally developing forced convection in a porous medium: parallel plate channel with walls at uniform temperature, with axial conduction and viscous dissipation effects. *International Journal of Heat and Mass Transfer, 46*(4), 643-651.

[49] **Kuznetsov, A. V., Xiong, M., & Nield, D. A.** (2003). Thermally Developing Forced Convection in a Porous Medium: Circular Duct with Walls at Constant Temperature, with Longitudinal Conduction and Viscous Dissipation Effects. *Transport in Porous Media, 53*(3), 331-345.

[50] **Nield, D. A., Kuznetsov, A. V., & Xiong, M.** (2002). Effect of local thermal non-equilibrium on thermally developing forced convection in a porous medium. *International Journal of Heat and Mass Transfer, 45*(25), 4949-4955.

[51] **Vafai, K., & Tien, C. L.** (1981). Boundary and inertia effects on flow and heat transfer in porous media. *International Journal of Heat and Mass Transfer, 24*(2), 195-203.

[52] **Kaviany, M.** (1985). Laminar flow through a porous channel bounded by isothermal parallel plates. *International Journal of Heat and Mass Transfer, 28*(4), 851-858.

[53] **Dukhan, N.** (2008). Developing Nonthermal-Equilibrium Convection in Porous Media With Negligible Fluid Conduction. *Journal of heat transfer, 131*(1), 014501-014501.

[54] **Haji-Sheikh, A., Nield, D. A., & Hooman, K.** (2006). Heat transfer in the thermal entrance region for flow through rectangular porous passages. *International Journal of Heat and Mass Transfer, 49*(17–18), 3004-3015.

[55] **Hooman, K., Haji-Sheikh, A., & Nield, D. A.** (2007). Thermally developing Brinkman–Brinkman forced convection in rectangular ducts with isothermal walls. *International Journal of Heat and Mass Transfer, 50*(17–18), 3521-3533.

[56] **Hooman, K., & Ejlali, A.** (2007). Entropy generation for forced convection in a porous saturated circular tube with uniform wall temperature. *International Communications in Heat and Mass Transfer, 34*(4), 408-419.

[57] **Hooman, K., & Haji-Sheikh, A.** (2007). Analysis of heat transfer and entropy generation for a thermally developing Brinkman–Brinkman forced convection problem in a rectangular duct with isoflux walls. *International Journal of Heat and Mass Transfer, 50*(21–22), 4180-4194.

[58] **Hooman, K., & Gurgenci, H.** (2007). Effects of viscous dissipation and boundary conditions on forced convection in a channel occupied by a saturated porous medium. *Transport in Porous Media, 68*(3), 301-319.

[59] **Hooman, K., & Gurgenci, H.** (2008). Effects of Temperature-Dependent Viscosity on Forced Convection Inside a Porous Medium. *Transport in Porous Media, 75*(2), 249-267.

[60] **Bhattacharya, A., & Mahajan, R. L.** (2002). Finned Metal Foam Heat Sinks for Electronics Cooling in Forced Convection. *Journal of Electronic Packaging, 124*(3), 155-163.

[61] **Zhao, C. Y., Kim, T., Lu, T. J., & Hodson, H. P.** (2004). Thermal Transport in High Porosity Cellular Metal Foams. *Journal of Thermophysics and Heat Transfer, 18*(3), 309-317.

[62] **Kurtbas, I., & Celik, N.** (2009). Experimental investigation of forced and mixed convection heat transfer in a foam-filled horizontal rectangular channel. *International Journal of Heat and Mass Transfer, 52*(5–6), 1313-1325.

[63] **Mancin, S., Zilio, C., Cavallini, A., & Rossetto, L.** (2010). Heat transfer during air flow in aluminum foams. *International Journal of Heat and Mass Transfer, 53*(21–22), 4976-4984.

[64] **Mancin, S., Zilio, C., Rossetto, L., & Cavallini, A.** (2011). Heat Transfer Performance of Aluminum Foams. *Journal of heat transfer, 133*(6), 060904-060904.

[65] **Dukhan, N., Al-Rammahi, M. A., & Suleiman, A. S.** (2013). Fluid temperature measurements inside metal foam and comparison to Brinkman–Darcy flow convection analysis. *International Journal of Heat and Mass Transfer, 67*(0), 877-884.

[66] **Hetsroni, G., Gurevich, M., & Rozenblit, R.** (2005). Metal foam heat sink for transmission window. *International Journal of Heat and Mass Transfer, 48*(18), 3793-3803.

[67] **Mancin, S., Zilio, C., Diani, A., & Rossetto, L.** (2013). Air forced convection through metal foams: Experimental results and modeling. *International Journal of Heat and Mass Transfer, 62*(0), 112-123.

[68] **Lambert, A. A., Cuevas, S., & del Río, J. A.** (2006). Enhanced heat transfer using oscillatory flows in solar collectors. *Solar Energy, 80*(10), 1296-1302.

[69] **Dukhan, N., Bağcı, Ö., & Kavurmacıoğlu, L. A.** (2015). Effect of frequency on heat transfer due to oscillating water flow in open-cell metal foam: An experimental study. *Experimental Thermal and Fluid Science, 66*, 97-105.

[70] **Kim, S. Y., Kang, B. H., & Hyun, J. M.** (1994). Heat transfer from pulsating flow in a channel filled with porous media. *International Journal of Heat and Mass Transfer, 37*(14), 2025-2033.

[71] **Guo, Z., Kim, S. Y., & Sung, H. J.** (1997). Pulsating flow and heat transfer in a pipe partially filled with a porous medium. *International Journal of Heat and Mass Transfer, 40*(17), 4209-4218.

[72] **Khodadadi, J. M.** (1991). Oscillatory Fluid Flow Through a Porous Medium Channel Bounded by Two Impermeable Parallel Plates. *Journal of Fluids Engineering, 113*(3), 509-511.

[73] **Zhao, T. S., & Cheng, P.** (1996). Oscillatory pressure drops through a woven-screen packed column subjected to a cyclic flow. *Cryogenics, 36*(5), 333-341.

[74] **Hsu, C.-T., Fu, H., & Cheng, P.** (1999). On Pressure-Velocity Correlation of Steady and Oscillating Flows in Regenerators Made of Wire Screens. *Journal of Fluids Engineering, 121*(1), 52-56.

[75] **Cha, J. S., Ghiaasiaan, S. M., & Kirkconnell, C. S.** (2008). Oscillatory flow in microporous media applied in pulse – tube and Stirling – cycle

cryocooler regenerators. *Experimental Thermal and Fluid Science, 32*(6), 1264-1278.

[76] **Pamuk, M. T., & Özdemir, M.** (2012). Friction factor, permeability and inertial coefficient of oscillating flow through porous media of packed balls. *Experimental Thermal and Fluid Science, 38*(0), 134-139.

[77] **Pamuk, M. T., & Özdemir, M.** (2012). Heat transfer in porous media of steel balls under oscillating flow. *Experimental Thermal and Fluid Science, 42*(0), 79-92.

[78] **Leong, K. C., & Jin, L. W.** (2006). Characteristics of oscillating flow through a channel filled with open-cell metal foam. *International Journal of Heat and Fluid Flow, 27*(1), 144-153.

[79] **Leong, K. C., & Jin, L. W.** (2005). An experimental study of heat transfer in oscillating flow through a channel filled with an aluminum foam. *International Journal of Heat and Mass Transfer, 48*(2), 243-253.

[80] **Pathak, M. G., Mulcahey, T. I., & Ghiaasiaan, S. M.** (2013). Conjugate heat transfer during oscillatory laminar flow in porous media. *International Journal of Heat and Mass Transfer, 66*(0), 23-30.

[81] **Sözen, M., & Vafai, K.** (1991). Analysis of oscillating compressible flow through a packed bed. *International Journal of Heat and Fluid Flow, 12*(2), 130-136.

[82] **Byun, S. Y., Ro, S. T., Shin, J. Y., Son, Y. S., & Lee, D. Y.** (2006). Transient thermal behavior of porous media under oscillating flow condition. *International Journal of Heat and Mass Transfer, 49*(25–26), 5081-5085.

[83] **Habibi, K., Mosahebi, A., & Shokouhmand, H.** (2011). Heat Transfer Characteristics of Reciprocating Flows in Channels Partially Filled with Porous Medium. *Transport in Porous Media, 89*(2), 139-153.

[84] **Dai, Q., & Yang, L.** (2013). LBM numerical study on oscillating flow and heat transfer in porous media. *Applied Thermal Engineering, 54*(1), 16-25.

[85] **Leong, K. C., & Jin, L. W.** (2006). Effect of oscillatory frequency on heat transfer in metal foam heat sinks of various pore densities. *International Journal of Heat and Mass Transfer, 49*(3–4), 671-681.

[86] **Leong, K. C., & Jin, L. W.** (2004). Heat transfer of oscillating and steady flows in a channel filled with porous media. *International Communications in Heat and Mass Transfer, 31*(1), 63-72.

[87] **Fu, H. L., Leong, K. C., Huang, X. Y., & Liu, C. Y.** (2000). An Experimental Study of Heat Transfer of a Porous Channel Subjected to Oscillating Flow. *Journal of heat transfer, 123*(1), 162-170.

[88] **Bağcı, Ö., Dukhan, N., & Özdemir, M.** (2015). Characteristics of oscillating liquid flow in foam-like highly-porous media: An experimental study. *Experimental Thermal and Fluid Science, 60*(0), 96-105.

[89] **Kaviany, M.** (2002). *Principles of heat transfer*: John Wiley & Sons.

[90] **Dukhan, N., Bağcı, Ö., & Özdemir, M.** (2014). Metal foam hydrodynamics: Flow regimes from pre-Darcy to turbulent. *International Journal of Heat and Mass Transfer, 77*(0), 114-123.

[91] **ERG Materials and Aerospace**. Retrieved 2015, from http://www.ergaerospace.com

[92] **Dukhan, N., & Patel, P.** (2008). Equivalent particle diameter and length scale for pressure drop in porous metals. *Experimental Thermal and Fluid Science, 32*(5), 1059-1067.

[93] **Kuwahara, F., Shirota, M., & Nakayama, A.** (2001). A numerical study of interfacial convective heat transfer coefficient in two-energy equation model for convection in porous media. *International Journal of Heat and Mass Transfer, 44*(6), 1153-1159.

[94] **Figliola, R. S., & Beasley, D.** (2015). *Theory and design for mechanical measurements*: John Wiley & Sons.

[95] **Bağcı, Ö., Dukhan, N., & Özdemir, M.** (2014). Flow regimes in packed beds of spheres from Pre-Darcy to turbulent. *Transport in Porous Media, 104*(3), 501-520.

[96] **Ward, J.** (1965). *Turbulent flow in porous media*: University of Arkansas, Engineering Experiment Station.

[97] **Macdonald, I., El-Sayed, M., Mow, K., & Dullien, F.** (1979). Flow through porous media-the Ergun equation revisited. *Industrial & Engineering Chemistry Fundamentals, 18*(3), 199-208.

[98] **Comiti, J., & Renaud, M.** (1989). A new model for determining mean structure parameters of fixed beds from pressure drop measurements: application to beds packed with parallelepipedal particles. *Chemical Engineering Science, 44*(7), 1539-1545.

[99] **Nield, D. A., & Bejan, A.** (2006). *Convection in porous media*: Springer Science & Business Media.

[100] **Venkataraman, P., & Rao, P. R. M.** (1998). Darcian, transitional, and turbulent flow through porous media. *Journal of Hydraulic Engineering, 124*(8), 840-846.

[101] **Bolt, G. H., & Groenevelt, P. H.** (1969). COUPLING PHENOMENA AS A POSSIBLE CAUSE OF "NON-DARCIAN" BEHAVIOUR OF WATER IN SOIL. *International Association of Scientific Hydrology. Bulletin, 14*(2), 17-28.

[102] **Sedghi-Asl, M., Rahimi, H., & Salehi, R.** (2014). Non-Darcy Flow of Water Through a Packed Column Test. *Transport in Porous Media, 101*(2), 215-227.

[103] **Paek, J. W., Kang, B. H., Kim, S. Y., & Hyun, J. M.** (2000). Effective Thermal Conductivity and Permeability of Aluminum Foam Materials1. *International Journal of Thermophysics, 21*(2), 453-464.

[104] **Hamaguchi, K., Takahashi, S., & Miyabe, H.** (1983). Flow friction and heat transfer characteristics of a regenerator matrix (case of foamed metal). *Trans. Jpn. Soc. Mech. Eng, 49*, 1991-2000.

[105] **Dukhan, N.** (2006). Correlations for the pressure drop for flow through metal foam. *Experiments in Fluids, 41*(4), 665-672.

[106] **Calmidi, V. V., & Mahajan, R. L.** (1999). The Effective Thermal Conductivity of High Porosity Fibrous Metal Foams. *Journal of heat transfer, 121*(2), 466-471.

[107] **Xu, H., Gong, L., Huang, S., & Xu, M.** (2014). Non-equilibrium heat transfer in metal-foam solar collector with no-slip boundary condition. *International Journal of Heat and Mass Transfer, 76*(0), 357-365.

[108] **Dukhan, N., & Suleiman, A. S.** (2014). Simulation of entry-region flow in open-cell metal foam and experimental validation. *Transport in Porous Media, 101*(2), 229-246.

[109] **Cengel, Y. A., Boles, M. A., & Kanoglu, M.** (1998). *Thermodynamics: an engineering approach* (Vol. 1056): McGraw-Hill New York.

[110] **Yang, C., Ando, K., & Nakayama, A.** (2011). A Local Thermal Non-Equilibrium Analysis of Fully Developed Forced Convective Flow in a Tube Filled with a Porous Medium. *Transport in Porous Media, 89*(2), 237-249.

[111] **Dukhan, N., & Ali, M.** (2012). Effect of Confining Wall on Properties of Gas Flow Through Metal Foam: An Experimental Study. *Transport in Porous Media, 91*(1), 225-237.

CURRICULUM VITAE

Name Surname:	Özer Bağcı
Place and Date of Birth:	İstanbul, 13.06.1983
E-Mail:	bagcio@itu.edu.tr, ozerbagci@gmail.com

EDUCATION:

B.Sc.:	Istanbul Technical University, Mechanical Engineering
M.Sc.:	Istanbul Technical University, Aeronautical and Astronautical Engineering

PROFESSIONAL EXPERIENCE AND REWARDS:

Project Titles

- Experimental investigation of influence of metal foam pore density variation under oscillating flow condition on fluid flow and heat transfer
- Experimental and Numerical Investigation of Fluid Flow and Heat Transfer in Open-Cell Metal Foam Subjected to Oscillating Flow
- Prediction of Combustion in a Diesel Engine Using Intrinsic Low Dimensional Manifolds Technique

Awards

- Derbentli Award of Success – June 2014, Istanbul
- Outstanding Paper Award – July 2014, Orlando, Florida: Study with title "Flow Regimes in Foam-Like Highly Porous Media" presented at the 10th International Conference on Heat Transfer in Orlando, Florida.

PUBLICATIONS AND PRESENTATIONS ON THE THESIS:

Published Journal Articles

- Dukhan, N., **Bağcı, Ö.,** & Kavurmacıoğlu, L. A. (2015). Effect of frequency on heat transfer due to oscillating water flow in open-cell metal foam: An experimental study. *Experimental Thermal and Fluid Science, 66*, 97-105.

- Dukhan, N., **Bağcı, Ö.,** & Özdemir, M. (2015). Thermal development in open-cell metal foam: An experiment with constant wall heat flux. *International Journal of Heat and Mass Transfer, 85,* 852-859.

- **Bağcı, Ö.,** Dukhan, N., & Özdemir, M. (2015). Characteristics of oscillating liquid flow in foam-like highly-porous media: An experimental study.*Experimental Thermal and Fluid Science, 60,* 96-105.

- Dukhan, N., **Bağcı, Ö.,** & Özdemir, M. (2014). Experimental flow in various porous media and reconciliation of Forchheimer and Ergun relations. *Experimental Thermal and Fluid Science, 57,* 425-433.

- Dukhan, N., **Bağcı, Ö.,** & Özdemir, M. (2014). Metal foam hydrodynamics: Flow regimes from pre-Darcy to turbulent. *International Journal of Heat and Mass Transfer*, *77,* 114-123.

- **Bağcı, Ö.,** Dukhan, N., & Özdemir, M. (2014). Flow regimes in packed beds of spheres from Pre-Darcy to turbulent. *Transport in Porous Media, 104*(3), 501-520.

- **Bağcı, Ö**., Dukhan, N., & Özdemir, M., "Fully-Developed Forced Convection in Heated Open-Cell Metal Foam: An Experimental Study Using Water," *Experimental Thermal and Fluid Science Journal,* Submitted, December 5, 2014

Journal Articles Under Review

- **Bağcı, Ö**., Dukhan, N., Özdemir, M., & Kavurmacıoğlu, L.A., "Experimental Heat Transfer Due to Oscillating Water Flow in Open-Cell Metal Foam," *International Journal of Thermal Science,* Submitted, December 15, 2014.

Presentations in International Conferences

- Dukhan, N., **Bağcı, Ö.,** Özdemir, M., & Kavurmacıoğlu, L. A., "Numerical Solution of Flow in Open-Cell Metal Foam and Comparison to Experiment", *8th International Conference on Computational Heat and Mass Transfer,* ICCHMT 8, May 25-28, 2015, Istanbul, Turkey.

- **Bağcı, Ö.,** Dukhan, N., & Özdemir, M., "Experimental Thermal Development in Open-Cell Metal Foam: Darcy Flow of Water" *7th International Conference on Porous Media,* InterPore 15, May 18-21, 2015, Padua, Italy.

- Dukhan, N., **Bağcı, Ö.,** Özdemir, M., & Kavurmacıoğlu, L. A., "Experimental Fully-Developed Thermal Convection For Non-Darcy Water Flow In Metal Foam", *International Conference On Advances In Mechanical Engineering Istanbul 2015 - ICAME'15,* May 13-15, 2015, Yildiz Technical University, Istanbul, Turkey.

- **Bağcı, Ö.,** Dukhan, N., & Özdemir, M., "Flow Regimes in Foam-Like Highly Porous Media," *10th International Conference of Heat Transfer, Fluid Mechanics and Thermodynamics*, Orlando, FL, July 14-16, 2014.

- **Bağcı, Ö.,** Dukhan, N., & Özdemir, M., "Various Flow Regimes and Permeabilities for Packed-Spheres Porous Media", *10th International Conference on Diffusion in Solids and Liquids,* Paris, France, June 23 – 27, 2014.

- **Bağcı, Ö.,** Dukhan, N., & Özdemir, M., "Experimental Characteristics of Oscillating Liquid Flow in Metal Foam: Effect of Flow Displacement", *3rd Rostocker Symposium on Thermophysical Properties for Technical Thermodynamics,* Çeşme, Turkey, June 12-15, 2014.

- **Bağcı, Ö.,** Dukhan, N., & Özdemir, M., “Liquid Flow in Packed Spheres of Equal Diameters: Regimes, Permeability and Forchheimer Coefficient,”, *Convective Heat and Mass Transfer Conference, CONV-14,* Kusadasi, Turkey, June 8-13, 2014.